

University of Padova

Department

“Territorio e Sistemi Agro-Forestali”

Master Degree in Forestry and Environmental Sciences

Monitoring mining activities using UAVs (Unmanned
Aerial Vehicles). A Chinese case study.

Supervisor

Prof. Paolo Tarolli

Co-Supervisor

Prof. Chen Jianping

MSc student

Eugenio Straffellini

Mat. 1133171

A.A. 2017/2018

For my parents,
Grandparents,
Tommaso and Federica

ABSTRACT

The technological progress that has characterized human beings since their appearance on our planet, despite being probably one of the main reasons for their undisputed dominance over other species, has not always brought only benefits. While technological progress has led to an increase in human life expectancy and the consequent exponential growth of the world population, the awareness of living in a highly vulnerable system characterised by scarce resources should be strongly affirmed in human society.

The continuous and massive exploitation of natural resources, which has grown strongly since the Industrial Revolution, has not only brought prosperity to the Great Industrial Powers of the World, but has profoundly changed the Earth's surface almost in its entirety, thus addressing scientists and scholars to the debate on Anthropocene, a new geological era.

Based on these considerations, this thesis aims to analyse one of the most controversial human practices ever: mining. While mines allow the availability of primary resources necessary to satisfy human well-being, they cause a profound modification of the Earth's surface, with direct and indirect consequences on the surrounding environment.

In this paper, the mining area of Miyun, PR China, is studied through the use of a technology that is rapidly expanding in the field of precision topography: 'Unmanned aerial vehicle' (UAV) photogrammetry using the 'Structure From Motion' (SfM) technique.

In particular, this work focuses on the processing and comparison of multi-temporal data obtained from two UAVs surveys inside the mine, respectively in 2014 and 2016.

Starting from the flight planning and the preliminary setting of the UAV, this work will show the methodologies for the construction of Digital Models of the Surface (DEMs) from the point clouds obtained through the SfM technique.

The following part of the work is instead dedicated to the elaboration of the models obtained, such as the geomorphological analysis of the surface of the mine, the quantification of the volume excavated and/or deposited in the two years under study and a detailed analysis of the subsidence that has characterized three trucks road.

With regard to the last part, this thesis aims to provide a methodology that can identify any areas at risk of subsidence through a multi-temporal approach, using UAVs. In addition, the method is applied not only for roads, but it can be also useful and usable in all those contexts where the presence of infrastructure on the territory requires particular attention because of a significant increase in risk situations.

SUMMARY

| | |
|--|----|
| ABSTRACT | 4 |
| INDEX OF FIGURES..... | 8 |
| INDEX OF TABLES..... | 13 |
| INDEX OF CHARTS..... | 14 |
| INDEX OF EQUATIONS..... | 15 |
| 1 INTRODUCTION | 16 |
| 1.1 Human impact on Earth: are we living in a new geological epoch?..... | 16 |
| 1.1.1 Anthropocene and the concept of Great Acceleration | 20 |
| 1.2 Raw material demands..... | 24 |
| 1.3 Introduction to mining | 28 |
| 1.3.1 Mining techniques..... | 29 |
| 1.4 Environmental issues related to mining activities | 34 |
| 1.4.1 Pollution..... | 34 |
| 1.4.2 Erosion..... | 36 |
| 1.4.3 Subsidence | 37 |
| 1.5 Disasters related to mining activities | 38 |
| 1.5.1 Brazil: Bento Rodriguez district’s disaster | 38 |
| 1.5.2 Hungary: Ajka red mud disaster | 40 |
| 1.5.3 Utah – USA: Bingham Canyon Copper mine disaster..... | 42 |
| 1.6 Mining activities monitoring using Remote Sensing..... | 44 |
| 1.7 Goals of the thesis..... | 48 |
| 2 REMOTE SENSING | 50 |
| 2.1 Remote sensing for land surface changes | 50 |
| 2.1.1 Remote sensing and Land Change Science | 51 |
| 2.1.2 Other example applications of Remote sensing..... | 52 |
| 2.2 SAR, Lidar & UAV Technologies..... | 54 |
| 2.2.1 SAR Technologies | 54 |
| 2.2.2 Lidar Technology..... | 55 |
| 2.2.3 Unmanned Aerial Vehicle (UAV) Technology | 60 |
| 2.3 Structure from Motion (SfM) Technology | 68 |
| 2.3.1 Functioning of SfM..... | 68 |
| 2.3.2 Theoretical application of SfM | 70 |
| 3 STUDY AREA | 74 |

| | | | |
|-------|--|---|-----|
| 3.1 | | Mining activities near Beijing | 74 |
| 3.2 | | The mine under study | 80 |
| 3.3 | | UAV field surveys | 82 |
| 4 | | METHODOLOGY | 86 |
| 4.1 | | UAV set up and flight plan | 86 |
| 4.1.1 | | UAV general settings | 86 |
| 4.1.2 | | UAV flight planning | 92 |
| 4.2 | | SfM photogrammetric survey | 94 |
| 4.3 | | DEM analysis | 98 |
| 4.4 | | DoD for volume quantification | 101 |
| 5 | | RESULTS AND DISCUSSION | 104 |
| 5.1 | | Results of the SfM applications | 104 |
| 5.2 | | DEMs calculation and analysis | 106 |
| 5.2.1 | | Introductory analysis | 106 |
| 5.2.2 | | Elevation analysis | 108 |
| 5.2.3 | | Slope analysis | 109 |
| 5.2.4 | | Aspect analysis | 110 |
| 5.2.5 | | Curvature analysis | 111 |
| 5.2.6 | | Roughness indexes analysis | 115 |
| 5.2.7 | | Main Statistical information of geomorphological analysis | 118 |
| 5.3 | | Volume quantification | 120 |
| 5.3.1 | | DoD analysis of entire open-pit mine | 121 |
| 5.3.2 | | DoD analysis of South-East deposit | 123 |
| 5.3.3 | | DoD analysis of central excavation area | 125 |
| 5.3.4 | | Tonnage estimation | 127 |
| 5.4 | | Subsidence estimation | 128 |
| 5.4.1 | | Subsistence estimation for the road's surfaces | 128 |
| 5.4.2 | | New challenges for the subsidence estimation using UAV | 132 |
| 6 | | CONCLUSION | 134 |
| 7 | | REFERENCES | 138 |
| | | ACKNOWLEDGEMENTS | 150 |

INDEX OF FIGURES

| | |
|--|----|
| Figure 1.1. Trends from 1750 to 2010 in globally aggregated indicators for socio-economic development.. Modified by Steffen et al (2015). | 21 |
| Figure 1.2. Trends from 1750 to 2010 for ten of the socio-economic graphs (excluding primary energy use) in three groups. Modified by Steffen et al (2015) | 22 |
| Figure 1.3. Trends from 1750 to 2010 in indicators for the structure and functioning of the Earth System. Modified my Steffen et al (2015)..... | 23 |
| Figure 1.4. Examples of surface mine: a) Open-pit mine (Anthony Collins Wordpress); b) Placer mining (johnfowler.photoshelter); c) Hydraulic mining (Malakoff Diggings); d) Dredging operations (WPL Group); e) In-situ..... | 29 |
| Figure 1.5. Examples of underground mine: a) Sub-Level Caving Subsidence reaches surface in underground mine (Wikipedia); b) Machine in an underground mine (Wikipedia); c) Underground mine gallery (ghosttownexplorers.org); d) Miners in an underground mine (myplac..... | 31 |
| Figure 1.6. Example of Highwall mining system (The Kyushu University Museum). | 33 |
| Figure 1.7. Scheme that shows the process from the mining's operation to the soil's impact. Modified by Salomons (1995). | 34 |
| Figure 1.8. Map showing Minas Gerais, the state in which the disaster occurred. Source: The Guardian | 38 |
| Figure 1.9. A representative picture about the Brazilian disaster: aerial view of the Rio Doce where the river joins the sea. Source: Nasa Earth Observatory. | 39 |
| Figure 1.10. Territorial framing of the disaster. Source: modified by .katasztrofavedelem.hu and Gelencsér et al., 2011. | 40 |
| Figure 1.11. Territorial framing of the mine, placed in Utah. Source: modified by Google Earth 2017. | 42 |
| Figure 1.12. Debris extension in the mine. Source: modified by Earthobservatory.nasa.gov..... | 42 |
| Figure 1.13. Representation of Landsat 7 working in space orbit. Source: Landsat.gsfc.nasa.gov..... | 45 |
| Figure 1.14. An example representing a drone flying over an open-pit mine. Source: modified by simtop.es. | 46 |

| | |
|--|----|
| Figure 2.1. Maps of the land use of Shijiazhuang area (China) in 1987(a) and 2001 (b). Modified by Xiao et al., 2006..... | 51 |
| Figure 2.2. Deterioration status assessment of AC roof. Three levels (low, medium and high) respectively in blue, yellow and red. Rimini, Italy..... | 52 |
| Figure 2.3. Operating scheme of SAR technology. Source: modified by: http://www2.ing.unipi.it/ | 54 |
| Figure 2.4. Interferograms derived from JERS-1 SAR. Modified my Beak, 2008..... | 55 |
| Figure 2.5. Light Detection and Ranging Systems Components. Source: https://www.elprocus.com .. | 56 |
| Figure 2.6. Lidar scan of the city of Bremen, Germany. Modify by Dorit Borrmann, and Jan Elseberg from Jacobs University Bremen | 56 |
| Figure 2.7. a) Operating principle of a terrestrial Lidar scanner during works. Modified by Dassot et. A. (2011); b) Schematic representation of a plane during a Lidar scan. Modified by www.aurorasolar.com | 58 |
| Figure 2.8. Different in endurance and altitude of different UAVs. Source: modified by Watts et al., 2012. | 61 |
| Figure 2.9. Different types of wing in two UAVs. (1) Parrot© DISCO FPV; (2) Aerofoundry© Watupá 300 | 62 |
| Figure 2.10. Some examples of UAV model: (1) DJI© Phantom 2; (2) DJI© Spreading Wings S1000; (3) MJX© X600..... | 63 |
| Figure 2.11. Example of the use of UAV for building a 3D-model of Belgium’s mine. Self-processing of data kindly granted by China University of Geoscience of Beijing. Map by OpenStreetMap© and processing using Pix4Dmapper© | 66 |
| Figure 2.12. How to take pictures for a correct using of SfM. (a) Interior; (b) Isolated object; (c) Façade. Source: modified by Agisoft Photoscan© User Manual..... | 68 |
| Figure 2.13. Scheme of SfM survey and the position of targets on the ground. Source: www.unvaco.org | 69 |
| Figure 2.14. DTM (0.1 m resolution) produced by SfM technology. (a), (b) and (c) are different results by using diverse analysis. Source: Prosdocimi et al. (2015)..... | 70 |
| Figure 2.15. Example of 3D-model in a Belgium’s mine. Self-processing of data kindly granted by China University of Geoscience of Beijing. Elaborated using Agisoft PhotoScan© | 71 |
| Figure 2.16. Example of volume calculation using data from SfM technology. Self-processed data (using PhotoScan© and CloudCompare©) kindly granted by CUGB. a)3D model of deposit; b) relative height for volume calculation. | 72 |

| | |
|---|----|
| Figure 3.1. Geographic framework of the major mines around Beijing. The red box indicates the mine under study. Self-produced data. Source: Google Earth® . | 75 |
| Figure 3.2. Mine 1 to 6. Self-produced data. Source: Esri, Digital Globe, GeoEye, Earthstar Geographics, CNES/Airbus DS, USDA, USGS, AeroGRID, IGN, and the GIS user community. | 76 |
| Figure 3.3. Mine 7 to 12. Self-produced data. Source: Esri, Digital Globe, GeoEye, Earthstar Geographics, CNES/Airbus DS, USDA, USGS, AeroGRID, IGN, and the GIS user community. | 77 |
| Figure 3.4. Mine 13 to 18. Self-produced data. Source: Esri, Digital Globe, GeoEye, Earthstar Geographics, CNES/Airbus DS, USDA, USGS, AeroGRID, IGN, and the GIS user community. | 78 |
| Figure 3.5. Mine 19 and 20. Self-produced data. Source: Esri, Digital Globe, GeoEye, Earthstar Geographics, CNES/Airbus DS, USDA, USGS, AeroGRID, IGN, and the GIS user community. | 79 |
| Figure 3.6. Geographical framing of the mine in Beijing area (1). The main body of the open-pit mine (2) (Source: Chen et al., 2015). Aerial view of December 2014 (3) and November 2016 (4) from Google Earth© and with two details (5) - (6). | 81 |
| Figure 3.7. The Skywalker X5, or the UAV used during the two surveys. Source: skywalkermdel.com. | 82 |
| Figure 3.8. Flight design of 2014 survey. | 83 |
| Figure 3.9. Flight design of 2016 survey. | 83 |
| Figure 3.10. Ground Control Points used in 2014. | 84 |
| Figure 3.11. Ground Control Points used in 2014. | 84 |
| Figure 3.12. The location of GCPs on the ground within the study area. | 85 |
| Figure 4.1. Electrical scheme: Engines (1); Speed Controls (2); Battery module (3); Battery (4). Powered by DraftSight 2017©. | 88 |
| Figure 4.2. Electrical scheme: Radio (1); Camera (2); Parachute (3); Wind speed sensor (4); Antenna of receiver (5); Receiver body (6); GPS receiver (7). Powered by DraftSight 2017©. | 89 |
| Figure 4.3. The three main movements of an airplane (1) and the components that allow them (1). Source: www.machinedesign.com and www.vincesrocket.com. | 91 |
| Figure 4.4. The main commands of a radio remote control. Source: ww.baronerosso.it. | 92 |
| Figure 4.5. Camera location and overlap of 2014 (1) and 2016 (2). Source: Agisoft PhotoScan© Report. | 94 |

| | |
|--|-----|
| Figure 4.6. Example of software screenshot during 2016 data process. | 95 |
| Figure 4.7. CloudCompare screenshot during 2016 cloud analysis. | 97 |
| Figure 4.8. Example scheme about how to work the aspect tool. Source: modified by ArcGis Help. ... | 99 |
| Figure 4.9. An operating scheme of DoD. Modified by Williams, 2012. | 101 |
| Figure 4.10. Screen of GCD Software. Source: joewheaton.org. | 103 |
| Figure 5.1. The first result of the 2014 survey (1) and 2016 (1). The detailed cartography will be shown later. | 104 |
| Figure 5.2. The red boundary line is the perimeter of the area occupied by the quarry in 2016, while the red-coloured part refers to the increase in the area of the excavation zone. The blue arrow shows the zone that will be zoomed in figure 5.3. | 106 |
| Figure 5.3. Particular example of increased surface area occupied by the quarry in the north-west. ... | 107 |
| Figure 5.4. Comparison between 2014 (left) and 2016 (right) DEMs. The blue arrow indicates one of the most important deposit of the quarry. The yellow arrows indicate the areas of greatest variation. | 108 |
| Figure 5.5. Comparison between 2014 (left) and 2016 (right) slope (deg) rasters. The red box highlights a terraced area. The yellow arrows indicate the areas of greatest variation. | 109 |
| Figure 5.6. Enlargement of the two rasters of the slope in the area of the large deposit to the south-east. The map allows to clearly appreciate the changes in the surface after two years from the first survey. The red box identifies a group of new buildings. The yellow arrows indicate the areas of greatest variation. | 110 |
| Figure 5.7. Comparison between 2014 (a- right) and 2016 (b-left) aspect. Black arrow indicates the main deposit. The yellow arrows indicate the areas of greatest variation. | 110 |
| Figure 5.8. Comparison between 2014 (a- right) and 2016 (b-left) aspect in the main southeast deposit. The yellow arrows indicate the areas of greatest variation. | 111 |
| Figure 5.9. Comparison between 2014 (a) and 2016 (b) Profile and 2014 (c) and 2016 (d) Plan curvature. Blue arrow indicates the main deposit and the red one indicates the extraction area. These portions of mine will be zooming in late. The yellow arrows indicate the areas of greatest variation. | 112 |
| Figure 5.10. Comparison between 2014 (a) and 2016 (b) Profile and 2014 (c) and 2016 (d) Plan curvature in the main deposit. The yellow arrows indicate the areas of greatest variation. | 113 |
| Figure 5.11. Comparison between 2014 (a) and 2016 (b) Profile and 2014 (c) and 2016 (d) Plan curvature in the main excavation. The yellow arrows indicate the areas of greatest variation. | 114 |

Figure 5.12. Comparison between 2014 (left) and 2016 (right) Roughness-elev rasters. The red box highlights the terraced area, the dark red indicates the expansion area of the mine zooming below and the yellow indicate the greatest variation. 115

Figure 5.13. Comparison between 2014 (a) and 2016 (b) Roughness-elev rasters. The excavation operations have simplified the topography with a drastic reduction in roughness. The yellow arrows indicate the areas of greatest variation. 116

Figure 5.14. Comparison between 2014 (left) and 2016 (right) Roughness-elev rasters. The red box highlights a terraced area. The yellow arrow indicate the areas of greatest variation..... 116

Figure 5.15. Enlargement of the roughness index-slope map inside the southern hole, characterized by a morphology of terracing. a) is about 2014 and b) 2016. 117

Figure 5.16. Comparison between 2014 (a) and 2016 (b) Roughness-slope rasters. The excavation operations have clearly simplified the topography of the ground, with a drastic reduction in roughness. The yellow arrows indicate the areas of greatest variation. 117

Figure 5.17. Maps of DoD based on a) 2016 orthophoto and b) 2016 hillshade..... 121

Figure 5.18. Entire mine DoD results observable as a histogram. a) and c) refer to the change in erosion/deposit area; b) and d) refer to the changes in volume..... 122

Figure 5.19. Maps of DoD based on a) 2016 orthophoto and b) 2016 hillshade of the SE deposit. ... 123

Figure 5.20. Deposit DoD results observable as a histogram. a) and c) refer to the change in erosion/deposit area; b) and d) refer to the changes in volume..... 124

Figure 5.21. Maps of DoD based on a) 2016 orthophoto and b) 2016 hillshade of the central excavation. 125

Figure 5.22. Excavation DoD results observable as a histogram. a) and c) refer to the change in erosion/deposit area; b) and d) refer to the changes in volume..... 126

Figure 5.23. a) and b) are the locations of the Road I; c) is the result of the distance calculation. 129

Figure 5.24. a) and b) are the locations of the Road II; c) is the result of the distance calculation..... 130

Figure 5.25. a) and b) are the locations of the Road III; c) is the result of the distance calculation.... 131

INDEX OF TABLES

| | |
|--|-----|
| Table 1.1. Geological Time Scale – Tulan University | 16 |
| Table 1.2. Two different alternatives for defining Anthropocene. Source: modified by Nature, Lewis & Maslin, 2015. | 18 |
| Table 1.3. Chronostratigraphic-Chart’s extract updated in 07/18. Modified by ICS – www.stratigraphy.org | 19 |
| Table 1.4. Minerals identified in red Mud their probable origins. | 41 |
| Table 2.1. Classification of UAVs according to size. Source: modified by TRADOC, (2010)..... | 61 |
| Table 3.1. Main characteristics of the major mines around Beijing. Self-produced data. Google Earth®. | 75 |
| Table 4.1. The main technical characteristics of UAV used for such work. | 87 |
| Table 4.2. The main parameters of the camera mounted on the Skywalker X5 used for the two flights. | 90 |
| Table 4.3. UAV Flights parameters. | 93 |
| Table 5.1. Comparison between main survey data..... | 105 |
| Table 5.2. Estimation of the extracted surface in the quarry..... | 107 |
| Table 5.3. Main statistical parameters of 2014 and 2016 geomorphological analysis. | 118 |
| Table 5.4. Results of DoD of entire quarry. | 121 |
| Table 5.5. Results of DoD of SE deposit. | 123 |
| Table 5.6. Results of DoD of central excavation. | 125 |
| Table 5.7. Tonnage estimation. | 127 |
| Table 5.8. For each section of road, the minimum, mean and maximum subsidence values (lowering of the surface) are indicated. The mean column refers to an average subsidence value of the three road sections. | 128 |

INDEX OF CHARTS

| | |
|----------------|-----|
| Chart 1.1..... | 24 |
| Chart 1.2..... | 25 |
| Chart 1.3..... | 25 |
| Chart 1.4..... | 26 |
| Chart 1.5..... | 26 |
| Chart 2.1..... | 64 |
| Chart 2.2..... | 64 |
| Chart 2.3..... | 65 |
| Chart 5.1..... | 118 |
| Chart 5.2..... | 129 |
| Chart 5.3..... | 130 |
| Chart 5.4..... | 131 |

INDEX OF EQUATIONS

| | |
|-------------------|-----|
| Equation (1)..... | 96 |
| Equation (2)..... | 98 |
| Equation (3)..... | 99 |
| Equation (4)..... | 100 |
| Equation (5)..... | 102 |
| Equation (6)..... | 102 |
| Equation (7)..... | 102 |
| Equation (8)..... | 102 |

1 | INTRODUCTION

1.1 | Human impact on Earth: are we living in a new geological epoch?

Detailed rocks stratigraphy studies worldwide over the last 150 years have led to the division of time into distinct units. The result of this work are the ‘*geologic columns*’ (Nelson, 2015), or rather periods classified by geological analysis and characterized by a known relative age.

The following table 1.1 proposes a simplification of this classification method.

Table 1.1. Geological Time Scale – Tulan University

| Eon | Era | Period | Epoch | Age(my) |
|-------------------------------|--|---------------|-------------|---------|
| Phanerozoic (Visible Life) | Cenozoic (Recent Life) (Age of Mammals) | Quaternary | Holocene | 0.01 |
| | | | Pleistocene | 1.8 |
| | | Tertiary | Pliocene | 5.3 |
| | | | Miocene | 23.0 |
| | | | Oligocene | 33.9 |
| | | | Eocene | 55.8 |
| | | | Paleocene | 65.5 |
| | | | Cretaceous | |
| | Mesozoic (Middle Life) (Age of Reptiles) | Jurassic | 145 | |
| | | Triassic | 200 | |
| | | Permian | 251 | |
| | Paleozoic (Ancient Life) | Pennsylvanian | 299 | |
| | | Mississippian | 318 | |
| | | Devonian | 359 | |
| | | Silurian | 416 | |
| Ordovician | | 444 | | |
| Cambrian | | 488 | | |
| | | 542 | | |
| | | | | |
| Proterozoic (Early Life) | | | | |
| | Oldest Known Life | | | 2500 |
| Hadean/Archean | | | | |
| | Oldest Known Rocks | | | 3800 |
| | Age of the Earth | | | 4600 |

Large divisions are Eons. From oldest to youngest are:

- i. Hadean (very few rocks of this age are known).

- ii. Archean (Ancient Rocks).
- iii. Proterozoic (means “early life”).
- iv. Phanerozoic (“visible life”).

The most recent Eons, Phanerozoic, are divided into 3 Eras:

- i. Paleozoic (means ancient life).
- ii. Mesozoic (means middle life, also called the age of dinosaurs)
- iii. Cenozoic (means recent life, also called the age of mammals).

The most recent Era, the Cenozoic, is subdivided into two Periods:

- i. Tertiary
- ii. Quaternary

Finally, another subdivisions of Periods are called Epochs. In particular:

- i. Paleocene, Eocene, Oligocene, Miocene and Pliocene for Tertiary period.
- ii. Pleistocene and Holocene for Quaternary Period.

The geological epochs, particularly important inasmuch characterized by relative short temporal unit, are calculated not only by stratigraphic analysis of rocks, but also by the observation of glacial cores, by the studying of characterize of living being lived in the past and by their variations along time.

Since its first appearance, the presence of human being had led to deep variations into Earth’s surface. Indeed, through the continuous and increasing anthropization of territory and the growing exploitations of natural resources for satisfy its needs, it is having a strong impact on Earth’s natural evolution.

Starting from these considerations, the scientific community is evaluating the creation of a new geological epoch called Anthropocene. (Crutzen, 2002). The term derives from the Greek “*anthropos*” and was coined by the biologist Eugene Stoermer and used by the Nobel laureate Paul Crutzen. This word means “*man*”, to prove how the *Homo sapiens* is a determinant variable in the Earth’s evolution.

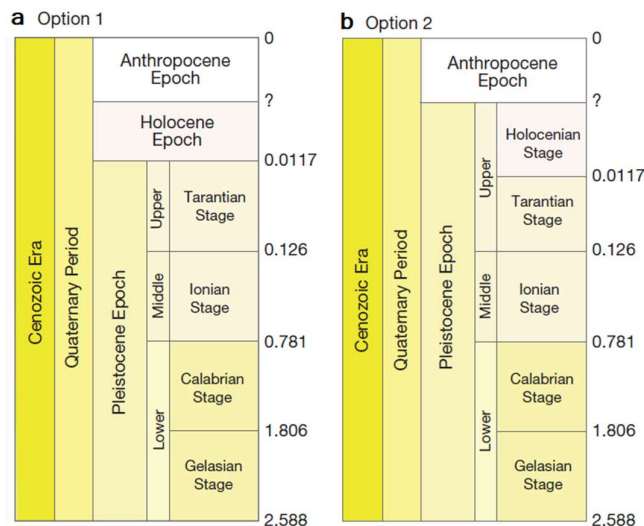
For the formalization of the creation of a new epoch in geological time, scholars must demonstrates that the Earth’s surface is undergoing noteworthy changes due to the impact of

man. Moreover, the magnitude of these impacts must be sufficiently high to justify the passage from Holocene to Anthropocene.

Consequently, as scientific evidence for demonstrating the high intensity of environmental impact due to man, scientists focus on the analysis of carbon dioxide and methane in polar ice, the rapid growth in urbanization and the important modification of natural elements (i.e. atmosphere, oceans, soils, living beings and more). (Erlandson, 2014)

As can be seen in table 1.2 below, the debate on the introduction of Anthropocene as a new epoch is leading to the definition of different assumptions about how to classify geological time (Lewis, 2015).

Table 1.2. Two different alternatives for defining Anthropocene. Source: modified by Nature, Lewis & Maslin, 2015.



Since the beginning of the Holocene, about 11,500 years ago, human activities on Earth have been growing progressively and are becoming more and more impacting.

From the moment that man learned the art of agriculture, born in Mesopotamia and then spread from Middle East to North Europe, there was a progressive shift from hunting to the exploitation of land for agricultural use. This change can be seen as a fossil record within rocks sediments and it becoming one of the oldest man's footprints on the Earth. In addition, the rise of agriculture associated with the beginning of forest exploitation for producing timber and artefacts, may have contributed to elevate CO₂ levels in the atmosphere long time before the Industrial Revolution (Ruddiman, 2003).

As well as Zalasiewicz (2011) declares, following the Neolithic revolution of agriculture, humans began to live in villages, and, still later, urban cultures spread across the tropical and

temperate zones everywhere. After that, the urbanization has accelerated and starting from medieval time arose the first million cities such as Paris and London. Nowadays, there are many megacities with >10 million habitants and these are intended to grow (Zalasiewicz, 2011).

That population growth is historically linked with the Industrial Revolution, which supplied the power and the technology to satisfy the cities demand. As reported in the work of Zalasiewicz (2011), urbanization is a direct result of a population explosion and the growth of cities is a characteristic feature of the Anthropocene. For this reason, Steffen, Grinevald et. Al (2011) suggested that AD 1800, approximately the start of the Industrial Revolution in Europe, could be considered as the beginning of the Anthropocene. (W. Steffen, 2011).

Science, by its definition and nature, is however in continuous evolution and change. In fact, during the final revision of this thesis work, at international level, a strong debate was opened that could overturn the "temporal classification" of the period in which we are living.

The International Union of Geological Sciences (IUGS) has changed the classification where the 21st century is located, no longer talking about Anthropocene (therefore admitting that human impact is so serious to close an Epoch and to open a new one), but updating Holocene (started 11,700 years ago after the last glaciation) through a new subdivision into three ages (Carrington, 2016).

The International Commission on Stratigraphy published, in July 2018, the updated version of "Chronostratigraphic Chart" (ICS, 2004), where the Holocene is divided in:

- Greenlandian Age; from the beginning of the Holocene Age to 8326 years ago.
- Northgrippian Age; since the end of Greenlandian Age to 4250 years ago.
- Meghalayan Age; from the end of Northgrippian Age to the present day.

The following table 1.3 shows the updated official graph.

Table 1.3. Chronostratigraphic-Chart's extract updated in 07/18. Modified by ICS – www.stratigraphy.org

| Series / Epoch | Stage / Age | numerical age (Ma) | |
|----------------|-----------------------------|--------------------|---------|
| Quaternary | Holocene <small>U/L</small> | Meghalayan | present |
| | | Northgrippian | 0.0042 |
| | | Greenlandian | 0.0082 |
| | Pleistocene | Upper | 0.0117 |
| | | Middle | 0.126 |
| | | Calabrian | 0.781 |
| | | Gelasian | 1.80 |
| | | 2.58 | |

The name of this new age comes from the North-Eastern Indian state of Meghalaya, where a stalagmite recovered from a cave has provided chemical evidence of a severe drought that occurred about 4200 years, considered the reason for the beginning of the last phase of Holocene (Maslin, 2018).

The fact that a drought of 'natural' origin has however conditioned so strongly the subdivision of time to the point of modifying the very-supported thesis of Anthropocene (where instead it is human impact that plays a fundamental role), is creating (and will create) considerable controversy both from a scientific and political point of view.

1.1.1 | Anthropocene and the concept of Great Acceleration

The concept of the "Great acceleration" was born in 2004 from a work led by Steffen, a professor at the Australian National University. It aims to describe and graphically represent appropriate socio-economic parameters and indicators regarding the Earth system over a period of time from 1750 to 2000, in order to observe its trends (Will Steffen et al., 2004). The work was then updated on the basis of new data and through the modification of some methodologies, studying an extended time frame until 2010 (Steffen, 2015). The following text in this chapter is based on the two articles mentioned above.

The "Great Acceleration" graphs were originally designed and built by a work of the International Geosphere-Biosphere Programme (IGBP), and they can offer an understanding of the structure and functioning of the Earth system. In addition, the growing human footprint on surface has been a crucial element, in particular, to recognize the relationship between the Earth system and economic development.

Starting from the date on which Cruzen proposed the beginning of Anthropocene and arriving until 2010, the Steffen et al project focused on defining the trajectory described by a series of socio-economic indicators over time, then comparing them with the trend of environmental parameters. The concept of Great Acceleration was born in the reading of the graphs, where since 1950 there has been a significant increase in the curves. In fact, Steffen, in 2004, affirmed that in the last 50 years there has been the most rapid transformation of the human relationship with the natural world in the history of humanity. Moreover, it adds that the term aims to capture the holistic, global and interconnected nature of post1950 changes that simultaneously affect the socio-economic and biophysical spheres of the Earth system and go far beyond climate change.

The next three figures (1.1, 1.2, 1.3) show Steffen's graphical results. As can be seen, the figure 1.1 represents the socio-economic trends in general quantitative terms, the figure 1.2 divides the data into three categories according to the economic classification of the analysed Country (OECD – 34 Countries; BRICS – 5 Countries; OTHERS) and the figure 1.3 shows the Earth system trend. Although it is not possible to assimilate a growth of the socio-economic trend to a cause-effect growth of the environmental indicators of reference, it is absolutely possible to find a strong correlation between them, and such data offer scientific proof that human activity significantly influences the structure and functionality of the Earth (Galloway et al., 2008).

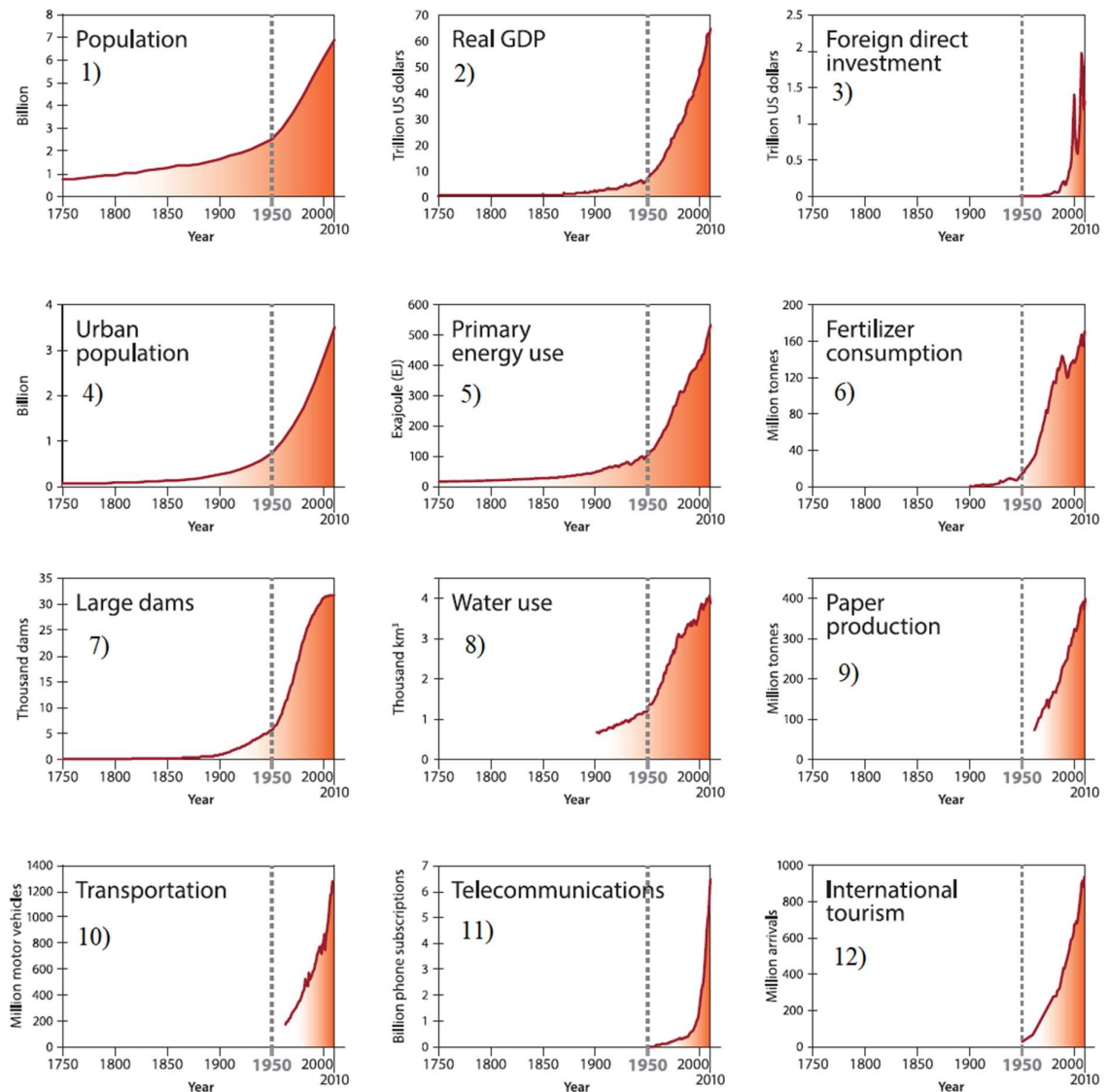


Figure 1.1. Trends from 1750 to 2010 in globally aggregated indicators for socio-economic development.. Modified by Steffen et al (2015).

- (1) Global population data according to the HYDE (History Database of the Global Environment, 2013) database.
- (2) Global real GDP (Gross Domestic Product) in year 2010 US dollars.
- (3) Global foreign direct investment in current (accessed 2013) US dollars.
- (4) Global urban population data according to the HYDE database.
- (5) World primary energy use.
- (6) Global fertilizer (nitrogen, phosphate and potassium) consumption.
- (7) Global total number of existing large dams (minimum 15 m height above foundation) based on the ICOLD (International Committee on Large Dams) database.
- (8) Global water use is sum of irrigation, domestic, manufacturing and electricity water.
- (9) Global paper production from 1961 to 2010.
- (10) Global number of new motor vehicles per year.
- (11) Global sum of fixed landlines and mobile phone subscriptions.
- (12) Number of international arrivals per year.

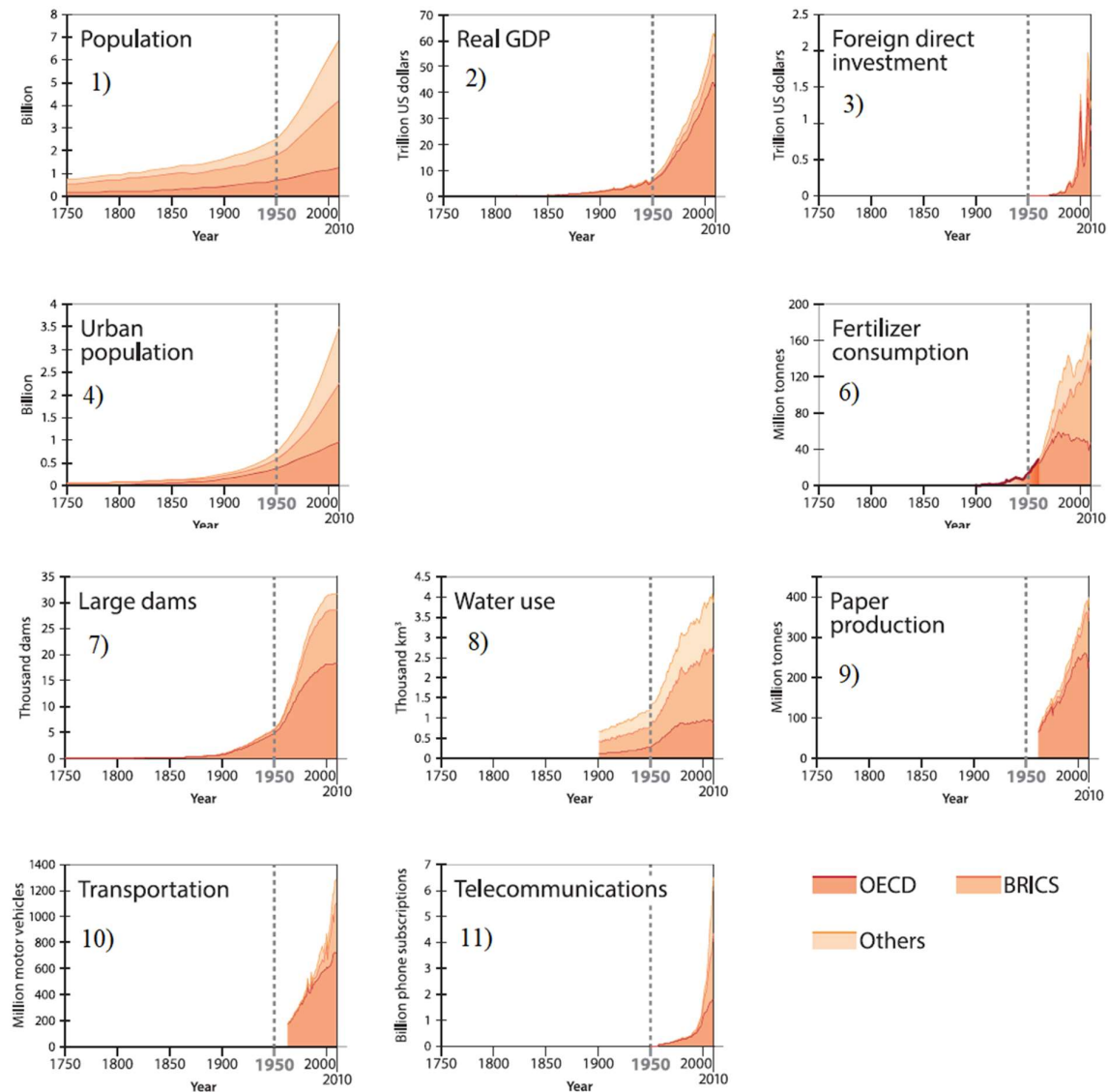


Figure 1.2. Trends from 1750 to 2010 for ten of the socio-economic graphs (excluding primary energy use) in three groups. Modified by Steffen et al (2015)

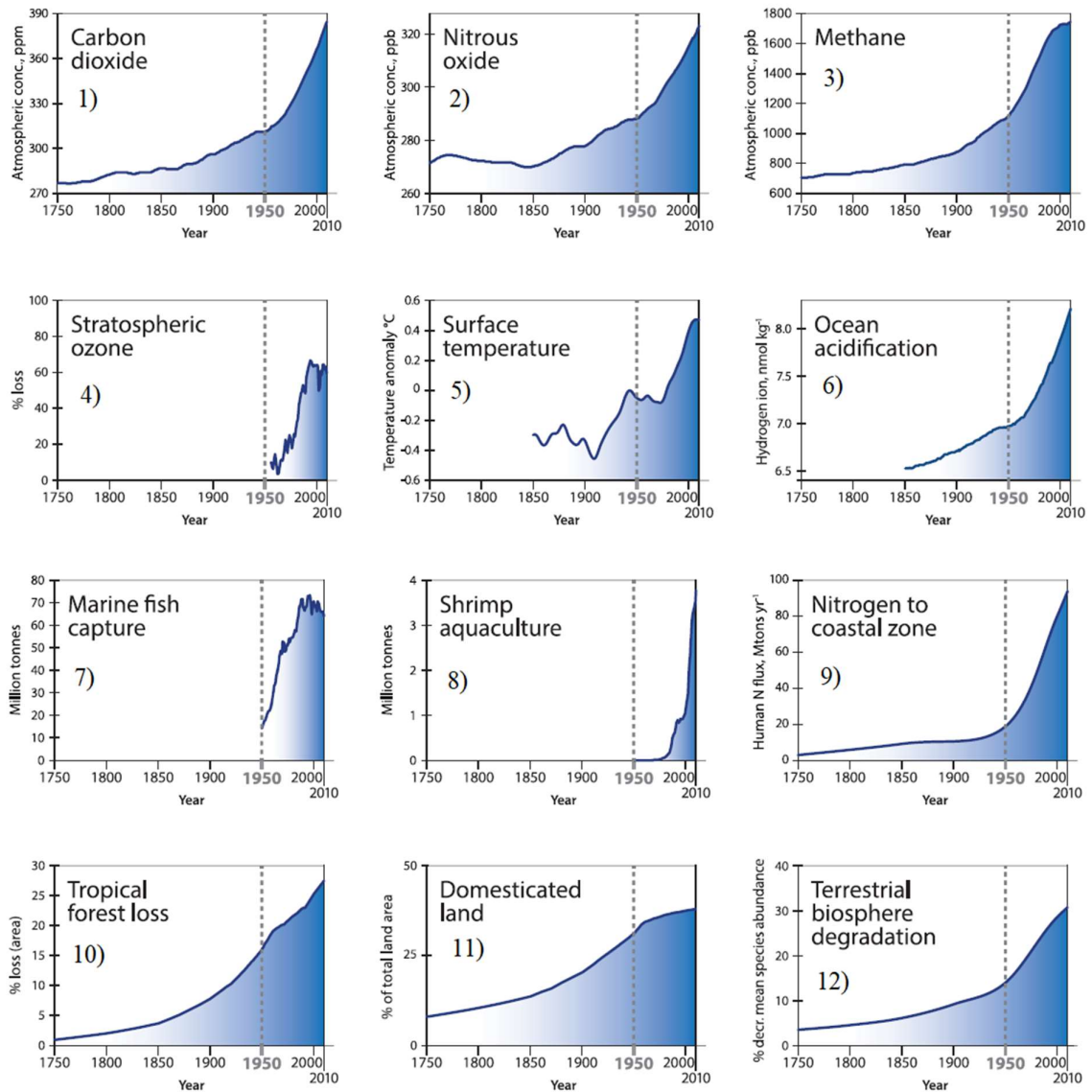


Figure 1.3. Trends from 1750 to 2010 in indicators for the structure and functioning of the Earth System. Modified by Steffen et al (2015).

- (1) Carbon dioxide from firn and ice core records.
- (2) Nitrous oxide from firn and ice core records.
- (3) Methane from firn and ice core records .
- (4) Maximum percentage total column ozone decline (2-year moving average).
- (5) Global surface temperature.
- (6) Ocean acidification.
- (7) Global marine fishes capture production.
- (8) Global aquaculture shrimp production.
- (9) Model-calculated human-induced perturbation flux of nitrogen into the coastal margin.
- (10) Loss of tropical forests.
- (11) Increase in agricultural land area.
- (12) Percentage decrease in terrestrial mean species abundance.

1.2 | Raw material demands

Here are showing and analysing some statistics about mining activities worldwide. For do it, is important to know how the energy is produced all over the world and how the quantity of raw material (i.e. indispensable for producing electric energy) changes along time and geographic region. Furthermore, is very interesting to compare the energy demand (classified by the different fuels) with the demographic evolution of Earth's population.

Firstly, the next chart 1.1 illustrates the time trend of world consumption (expressed in 'Million tonnes oil equivalent') needed to satisfy the world demand. The graph shows that the more consumed fuels refers to world level are oil, coal and natural gas in last 25 years.

Very is the fact that the consumption grew only by 1.0% in 2016, well below the 10-year average of 1.8%. Moreover, as well as happened in 2015, growth was below average in all regions except Europe and Eurasia (bp, 2017). Therefore, as well as possible to see in BP statistical review (2017), oil provided the largest increment to energy consumption at 77 million tonnes of oil equivalent (mtoe), followed by natural gas (57 mtoe) and renewable power (53 mtoe). In addition, as can be seen from the chart 1.1, in the last 25 years there was a general increase in world consumption.

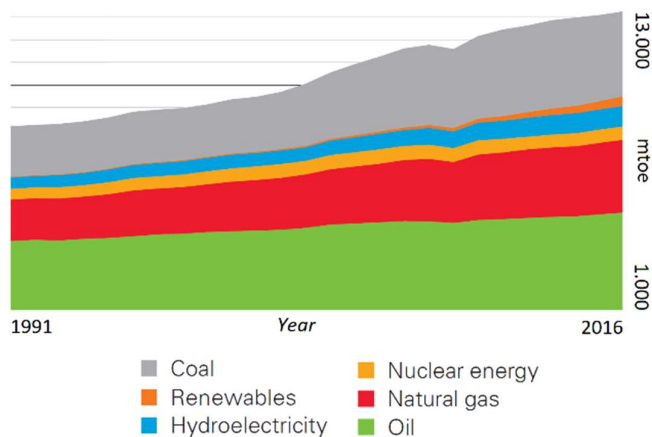


Chart 1.1. World consumption in mtoe from 1991 to 2016. Source: modified by BP Statistical review - 2017

This fact is probably dictated by a rise in the number of world citizen appreciable in chart 1.2 (World Bank Group, 2017), built by a self-analysis of populations data.

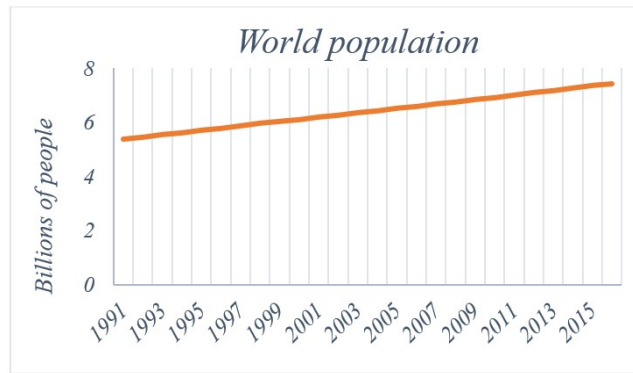


Chart 1.2. World population's trend from 1991 to 2016. Source: data.un.org

Speaking about fossil fuels, examining the regional consumption by fuel in next chart 1.3, calculated by 2015 data by World Mining Data 2016, is possible to appreciate that the macro-area where there is the wider use of coal, expressed in percentage, is Asia Pacific. In particular, the county leader in mineral fuel production is China (with 3,682,421,706 t), followed by USA and Russia (Reichl, 2017).

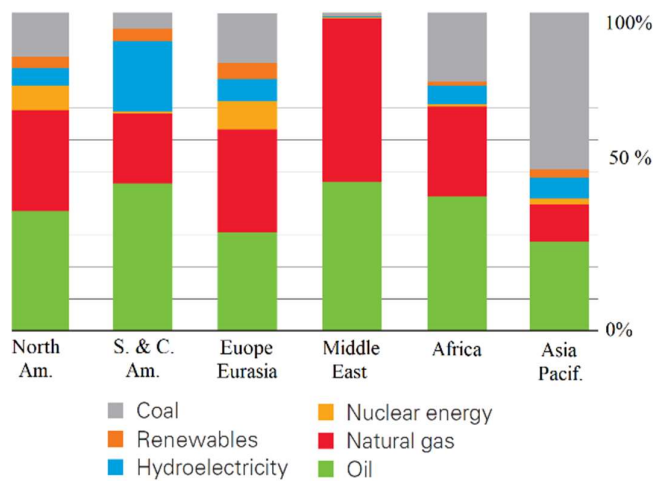


Chart 1.3. Consumption of fuel in percentage, classified by region. Source: modified by BP statistical review - 2017

Moreover, oil remains the world's dominant fuel, which accounts for about one third of the total energy consumed. In 2016, it gained global market share for the second consecutive year, following 15 years of declines from 1999 to 2014.

Regarding coal, in the last years its market share fell to 28.1%, the lowest level since 2004. These data, available on BP statistical review of 2017, are reported in percentage in the chart 1.4 below.

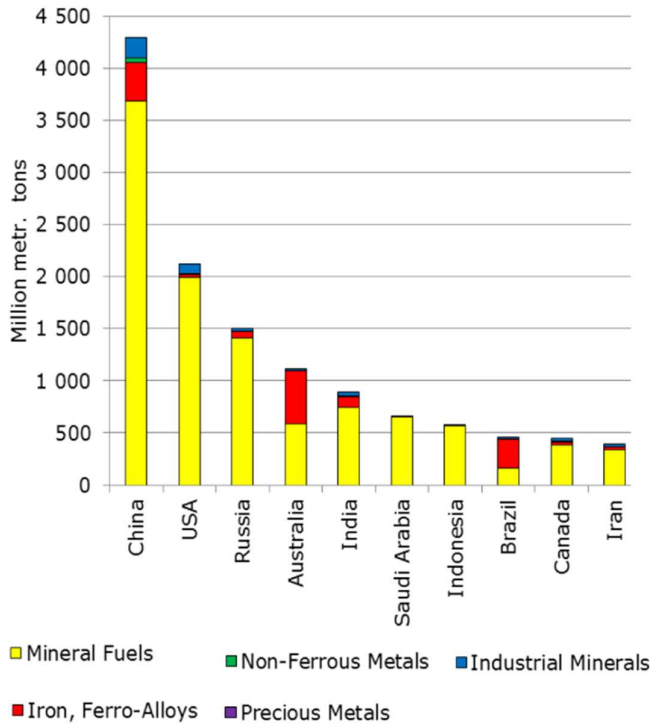


Chart 1.4. Statistics about largest coal producer countries in 2015 (without construction minerals, in Million m. t) Source: modified by World Mining Data 2017.

To deepen this decrease in coal production worldwide and to macro-economic regions level is possible to observe the next chart 1.5 a). Yellow line allow to know the great growth in coal production of China starting from the first years of twenty-first century and the next decrease in subsequent years (International Energy Agency, 2017). In addition, grey line in chart 1.5 b), describes the variation of coal production since 1970.

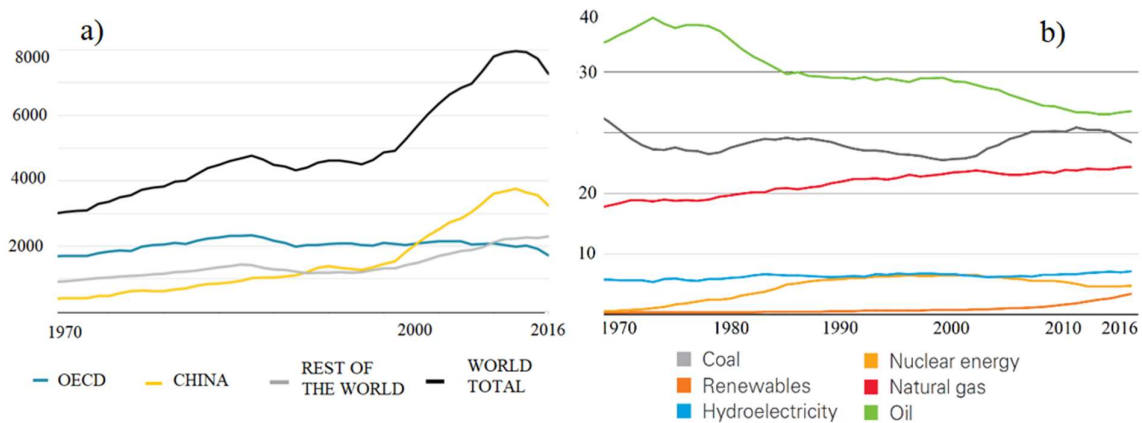


Chart 1.5. a) World total coal production in Mt. Source: Modified by International Energy Agency – iea – 2017; b) Shares of global primary energy consumption in percentage. Source: BP statistical review 2017

1.3 | Introduction to mining

The mining industry, as well as the energy sector, is to be considered fundamental for the analysis of evolution of the human being. His study allows to know the Economic Geography of a Country and, therefore, helps to understand many reasons regarding the variation of land use within a territory.

The Earth's crust hires a great economic importance for man because, starting by rocks, is possible to produce mineral building materials and key elements for industrial processes. In addition, the location of mineral deposits within an area, combined with technological innovation in transport field and electricity production, has historically represented the ideal location for the development of large industrial agglomerations.

Starting from the Industrial Revolution, mining raw materials are the basis of productive activities and, for this reason, possession of them is considered a decisive strategic factor. Mineral resources are concentrated in deposits, or areas where there is a concentration of such mineral higher than the average of other parts of the Earth's crust. Their formation requires extremely long times (from millions to tens of millions of years) and for this reason, despite the ongoing training process, mineral resources are probably destined to run out. The processes that originate raw material deposits are the same ones that are at the base of the formation of various types of rocks. In fact, there are three different types of processes, which lead to the formation of deposits: magmatic, sedimentary and metamorphic. The whole set of rock formation processes along the time line determines the geological history of an area, with evident consequences on the spatial distribution of mineral deposits along the Earth's surface.

Indiscriminate exploitation of mining resources has led to two orders of problems (in the following chapters the theme of environmental issues linked to mining activities will be treated with more detail).

- i. For some raw materials, there is a serious risk of resource depletion in relatively short time (this is the case, for example, of oil extraction). This problem is dictated by the fact that the exploitation resource rate is higher than the natural formation process rate.
- ii. Extraction of materials causes considerable environmental problems. For example, the opening of giant excavations contributes to accelerate the surface's erosion by atmospheric agents. Furthermore, the large quantities of waste that are abandoned after excavation can be dispersed in the hydrosphere with serious problems related, for example, to pollution.

1.3.1 | Mining techniques

Mining industry aims to extract minerals or other geological materials, working from natural deposits, to satisfy raw the material demand on international market. Techniques are many and differ as function of the type of area to be exploited.

Next chapters explains some example about traditional exploitation methods. In this work of thesis, they are classified into three broad categories.

1.3.1.1 | Surface mining

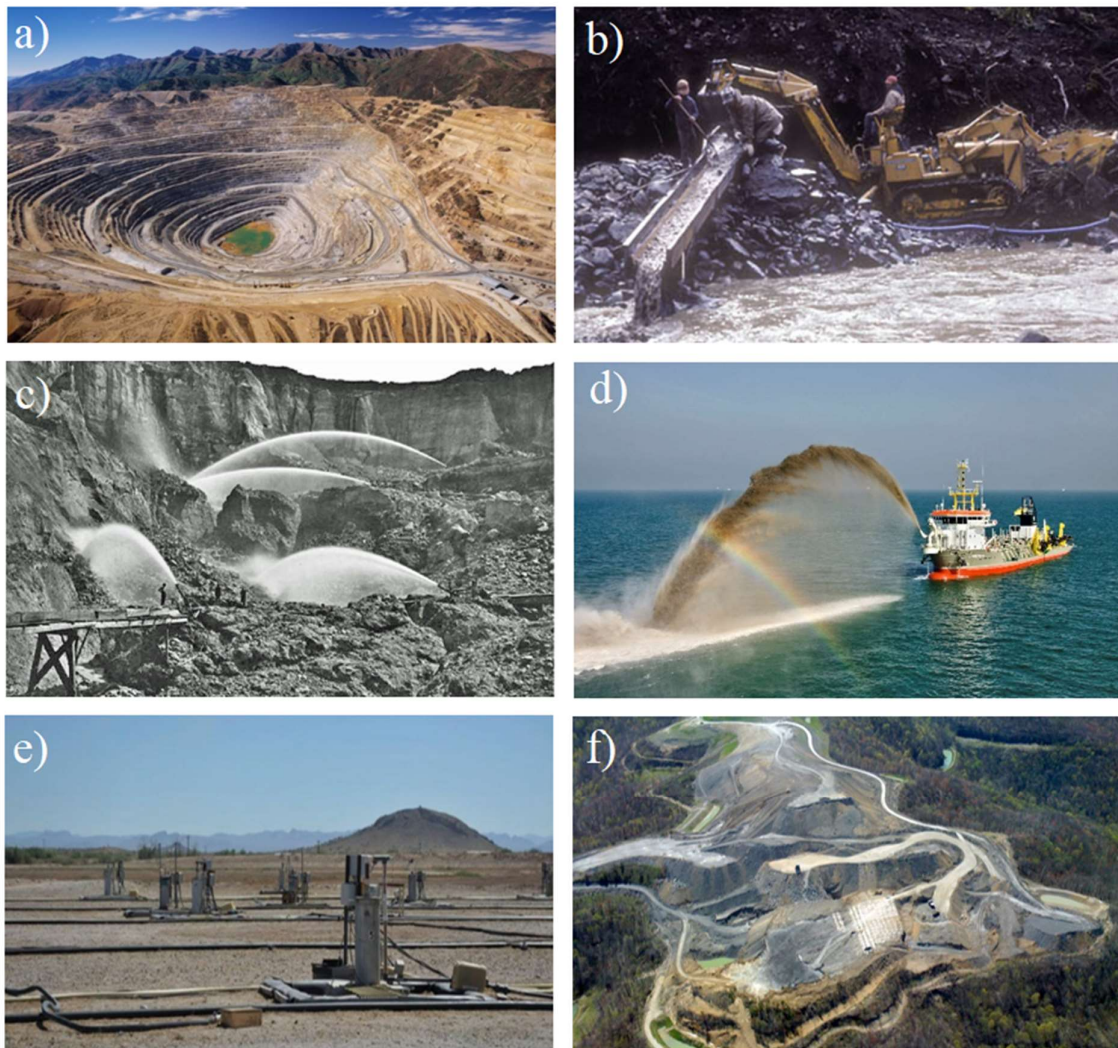


Figure 1.4. Examples of surface mine: a) Open-pit mine (Anthony Collins Wordpress); b) Placer mining (johnfowler.photoshelter); c) Hydraulic mining (Malakoff Diggings); d) Dredging operations (WPL Group); e) In-situ.

Surface mining is the predominant exploitation procedure worldwide: in United States, for example, is produced about 85% of all minerals (excluding petroleum and natural gas) and most of these are mined by open pit or open cast methods (Weedman, 2001). Below are cited some of the most commonly used surface mining methods.

- i. *Open pit mining*. It is a mechanical extraction method where deposit is generally mined in benches or steps. Open pit (or open cast) mining is usually used to exploit an ore near surface and, often, necessitates a large capital investment. Anyway, this type of quarry is also very productive thanks to its size, low operating cost, and good safety conditions. (Hartman, 2002). Figure 1.4.a shows an operative example.
- ii. *Aqueous extraction methods*. This method, as explained by Weedman in 2011, take advantage by water or another liquid (e.g., dilute sulphuric acid, weak cyanide solution or ammonium carbonate) to extract the mineral.
- iii. *Placer mining*. It is another technique used to exploit consolidated deposits like sand and gravel, especially for material that contain coal, mineral, gemstones and precious metals. In particular, this technique is the mining of stream bed deposits (alluvial) or, occasionally, of glacial deposits. Figure 1.4.b shows an operative example.
- iv. *Hydraulic mining (or Hydraulicking)*. This is another type of quarry where is utilized a high-pressure stream of water directed against the mineral deposit for extract ore. Indeed, this jet causes breaks in the rock with the consequent removal of material by the erosive actions of the water (Thrush, 1996). Figure 1.4.c shows an operative example.
- v. *Dredging*. This is an another type of mining performed by floating ships in rivers, lake or sea where the level of water is not too high. The machine used in this technique is called *dredge* and the extraction of minerals could be done by mechanically or hydraulically way. Figure 1.4.d shows an operative example.
- vi. *Solution mining*. This method, also called *in-situ recovery (ISR)*, is a mining process used to recover minerals through boreholes drilled into a deposit. Firstly, in this process, some holes are excavated into the ore deposit and subsequently explosive or hydraulic fracturing may be used to create open pathways for the penetration of an appropriate solution. A flow is pumped into the deposit where it makes contact with the ore. Thanks to this process, is possible to extract metals and minerals from an ore body without using conventional mining technique likes open-cut or underground mining (World Nuclear Association, 2017). Figure 1.4.e shows an operative example.

- vii. *Mountaintop removal mining (MTR)*. This method, also known as *mountaintop mining (MTM)*, is a form of surface mining performed at the summit of mountain, where coal are extracted by removing land. Explosives are used to remove up to 120 vertical meters of mountain to expose underlying coal seams. Excess rock and soil is dumped into nearby valleys that are called "*holler fills*" or "*valley fills*" (United States Environmental Protection Agency, 2016). Figure 1.4.f shows an operative example.

1.3.1.2 | *Underground mining*



Figure 1.5. Examples of underground mine: a) Sub-Level Caving Subsidence reaches surface in underground mine (Wikipedia); b) Machine in an underground mine (Wikipedia); c) Underground mine gallery (ghosttownexplorers.org); d) Miners in an underground mine (myplac).

Underground mining, also called unsupported, supported, or caving, consists of excavate tunnels (or shafts) into the surface to reach buried ore deposits. In fact, extracted minerals (and waste materials) are transported to the Earth's surface through tunnels and shafts. The type of wall and roof supports used may classify this type of mining. In addition, depends by configuration and size of site and by the direction in which mining operations evolves.

Below are cited some of the most commonly used underground mining methods.

1. *Underground hard rock mining.* As well as mentioned by Thrush in 1996, “Underground hard rock mining” is a term that described various set of underground mining techniques used to excavate hard minerals. In particular, it is often used for extracting metals like gold, silver, iron, copper, zinc and nickel. However, this method is also used for excavating ores characterized by the presence of precious gems. Furthermore, is possible to used to the excavation minerals such as salt, coal, or oil sands. In figure 1.5.a there is a mine-collapse situation.
2. *Underground soft rock mining.* It is another group of underground mining techniques mainly used to extract coal, oil and other minerals or geological materials from sedimentary rocks. Considering that the deposits in sedimentary rocks are commonly layered and relatively soft, this mining methods differ from those used to mine deposits in igneous or metamorphic rocks.

Two very common types of underground mining are:

- i. *Drift mining.* This is one of the most famous technique: is an underground method in which the entry of mine is called *adit*, or rather, where the entrance to an underground mine is horizontal or nearly horizontal. Using this type of entrance is possible to enter, drain water, ventilate mine, and extract minerals at the lowest level (Raymond, 1881). Adits are also used to explore mineral veins before opening a new site. Figure 1.5.b show a drift mining machine operating under the Earth’s surface.
- ii. *Shrinkage Stope Mining.* This term is used to describe the process of mining upwards from a lower to an elevated level, leaving the resulting broken rocks (i.e. waste material) in the excavation just created (GreatMining, 2017). These broken rocks acts as a working platform for miners and assists to stabilize the excavation by supporting the walls. In addition, the method may be used for ore mining in shrinkage stopes and for underground construction projects.

1.3.1.3 | Highwall mining

Highwall mining is a particular form of surface mining that evolved from auger mining. In this technique, the coal seam is penetrated by a continuous miner (a machine that produces a constant flow of ore from the working face of the mine) propelled by a hydraulic mechanism called PTM (Pushbeam Transfer Mechanism) (RitchieWiki, 2017).

In this method, starting from a great-size crater created for an open-pit-mine exploitation, some augers are used to perforate different entrances into the coal seam on the highwall's side (O'Hagan, 1997). After that, ore is carried out by remote control where an operator (located in a cabin) uses a television camera for monitoring and controlling the processes. An example of Highwall mining is reported in follow figure 1.6.



Figure 1.6. Example of Highwall mining system (The Kyushu University Museum).

1.4 | Environmental issues related to mining activities

Here is proposing an alternative way to observe mining activities: to analyse its relationship with the environment.

Within the technological and cultural evolution of recent years, the mining industry certainly plays a key role on two fronts. 1) Coal, for example, is nowadays indispensable for the human energy needs: through which 36% of the world's electricity is produced using this mineral; 2) The process of coal extraction from the Earth's surface is extremely impacting and polluting for environment (R. K. Tiwary, 2001).

In fact, despite mining activities affects relatively small areas in relation with the enormity of the Earth's crust, it may has a large local impact on the environment (Salomons, 1995). Figure 1.7, modified from Salomon's work, can synthesize and outline how these types of human's activities influences the soil.



Figure 1.7. Scheme that shows the process from the mining's operation to the soil's impact. Modified by Salomons (1995).

Mining activities may represents an environmental problem in diverse ways: firstly, different processes for mining leads direct and indirect pollution to local territory (for example interfering with close hydrographic network and releasing pollutants).

On the other hand, the opening of wide excavations may lead to structural collapse of mine, due to a continuous surface erosion of the soil carried by rainfall and weathering.

Another problem is certainly dictated by subsidence, which can affect different areas within a mine: subsidence of deposits of material, which in the most extreme cases can facilitate the collapse, and subsidence of the ground subjected to the continuous transit of heavy vehicles through the excavation area.

1.4.1 | Pollution

Speaking about pollution, in the process of mining large amounts of water are discharged on surface to facilitate the mining operation. This water often contains high amount of pollutants and, sometime, it causes acidification of water regime. Mine water, discharged from

underground and open cast mines, if not suffers a proper treatment generally contain high level of TSS (*Total suspended solids*), TDS (*Total dissolved solids*) and other pollutants (i.e. heavy metal, nitrate, sulphate, oil, grease and more). These pollutants can be lethal to aquatic flora and fauna and, if they are subjected by a bio-magnification process, is possible that pollutants will be arrive in human diet. This event depends by many different factors, first of all by the specifics and the concentration in the water of pollutants (R. K. Tiwary, 1994). Other important factors for describing water pollution are pH, water hardness, presences of other non-toxic metals and adsorbing or complexing agents. These factors are mirrored on mine water discharge, and are often associated with acid mine drainage (R. Tiwary, 1997).

Moreover, toxicity for a living being can be acute or chronic due to exposure usually greater than one year (Azapagic, 2004). Tiwary et al, in 1994, studied the Damodar River (placed in India), where the environment is significant threatened by a large mining activity. These studies shows that mine water often contains high level of total dissolved solids TDS in the range of 200–860 mg L⁻¹ and it proves that this type of exploitation of landscape may have negative effects on the quality of river water.

Speaking about types of pollutants, in water mine are dissolved cations as calcium, magnesium, sodium and potassium. The major anions, instead, are sulphate, chloride, fluoride, nitrate, bicarbonate and carbonate. From the dissolution of pyritic sulphur in the mines is possible to find thiosulphate and sulphuric minerals and, close to quarries, their concentrations are generally high. This is an important environmental problem because they may create oxidation with the consequence acidification of waters.

Other water pollutants bounded to mining activities, as well as explained by Tiwary et al. in 2001, are nitrate ions. They are usually created from explosives used to blast the coal in the mines.

In addition, oil and grease are founded next to effluents by workshop leak: oil or other toxic reagents are frequently originated by spillage of fluids in mine area due to exploitation's processes. In particular, this pollutant is highly dangerous for the area because forms a thin hydrocarbon film that interferes with the reoxygenation of the water. It may become unsafe for aquatic ecosystems with a serious consequent on environment and, in the most serious cases, in people diet.

Moreover, the presence of high concentration of pollutants in water could interfere with its self-purification capacity, leading to a diminishing light penetration and, subsequently, in a decreasing of photosynthesis yield.

A serious problem is represented by dumps and, in particular, by percolate. Rainfall may dissolve some toxic metals from its heap and may contaminate the water course. The problem becomes more complicated when dumps contains pyritic waste.

In extreme cases, silt deposition can lead to flooding and interfere with other biological activities. In case of coal, mining TSS normally contains high amount of fine coal particles and it makes surface water blackish and reduces aesthetic values of receiving water bodies.

If it is true that mining activities are indispensable for human development, on the other hand the process transforms fertile land into wasteland and causes serious environmental pollution and ecological degradation, which can lead to the loss of biodiversity, amenity, and economic wealth (Zhao et al., 2013).

1.4.2 | Erosion

Opencast mining is an efficient way for the exploitation of mineral resources. However, this technology can have a large impact on landscape by eliminating vegetation and permanently altering topography, soils and geological structures. As result of these facts is possible to observe an increase in soil erosion due to runoff and to insistent meteorological actions (Zhang et al., 2015) or, in other words, a selective process that sweeps away fine materials and nutrients from sloped lands (Polyakov et al., 2004).

In particular, the erosion of waste dumps constitute one of the major problem by open pit mining. The magnitude of erosion depends not only by rainfall characteristics, but also by surface properties and topographic features (Puigdefabregas, et al., 1999). As a result, land used for waste dumps becomes less fertile and more depleted in nutrients. Runoff and soil erosion hinder vegetative restoration in dumps, further inducing runoff and soil erosion and leading to a more severe threat to the stability of local ecosystems and economic development (K. Evans et al., 2004).

Summing, open mining activities lead to the elimination of vegetation, deep alteration of topography and soil with a drastically modification in geological subsurface structure and in hydrogeological regime.

1.4.3 | Subsidence

Subsidence is a phenomenon of soil lowering that can have natural causes, linked to geological processes, and artificial or anthropogenic causes linked to human actions. At a natural level, the subsidence is particularly evident in areas where there is considerable sedimentation of material, where the thickness of material can be very substantial.

Studying its characteristics is very important when there is infrastructure in the areas concerned, due to a significant increase in risk. For this reason, it is essential to study methodologies capable of monitoring soil movements, and to be able to offer an active tool of prevention.

In the specific case of mining, the study of subsidence can be of considerable importance in several aspects. First of all, the phenomenon of subsidence, if not monitored and properly treated, can lead to extreme cases of collapse of structures, both in open-cast and underground mines. An example of this is the 1996 disaster in Gretley Colliery, Australia, where four people were killed after a collapse (Ge et al., 2001). In addition to the fundamental theme of operator's safety in the mine, the monitoring of the phenomena of changes in the topography of the excavated areas makes it possible to study detailed maintenance plans, with positive results also on the economic results of the mine (Ambrožič et al., 2003).

Another aspect in which subsidence can affect mining activity is closely linked to the operations of excavation and transport of the material. Within the mines, the heavy vehicles necessary for the movement and transport of the material work full time, thus continuously soliciting the ground. It is therefore to be expected that with the course of time the dirt roads of the quarries will be affected by subsidence and collapses (Ge et al., 2016).

1.5 | Disasters related to mining activities

In this chapter will be explain some examples about how mining can become a really threat, not only for environment and biodiversity, but also for the safety of cities and human activities.

1.5.1 | Brazil: Bento Rodriguez district's disaster

First, a representative example about the risk related to mining activities is the event that affected Brazil (municipality of Mariana Minas Gerais), in November 5th, 2015. Figure 1.8 shows the geographic framing of the event.



Figure 1.8. Map showing Minas Gerais, the state in which the disaster occurred. Source: The Guardian

Particularly, between 40-62 million m³ of water and sediment sluiced down a mountainside from an iron open-pit-mine when the Fundão dam failed (Lopes, 2016). This volume represents the largest tailings dam break down in modern history, higher than the magnitudes of the two largest incidents heretofore, especially in the Philippines in 1982 (28 million m³) and 1992 (32.2 million m³) (Fernandes et al., 2016).

This event was larger studied by a scientific point view because it affected environment both as pollution and both as erosion of surface. Furthermore, it strongly damaged people in surrounding area.

i. *Impacts on environment:*

The mine slurry-water affected hydrologic networks for 663.2 km in the Doce River, through the states of Minas Gerais and Espirito Santo and arrived until its estuary in the city of Linhares. The magnitude of this event was catastrophic: it represents, if fact, the longest travelled distance by tailings in a dam failure event in South America (INPE - Instituto Nacional de Pesquisas

Espaciais, 2015). Effects on ecosystem were austere and persistent for whole watershed. A few days following the disaster, analysis of surface reflectance data in Landsat-8 images allowed measurements of the extent and intensity of the damage, identifying significant vegetation loss and deposition of tailings with extreme high concentration of iron along the Doce River (Mielke et al., 2015). The event, as well as explained by Fernandes in 2016, affected almost 1469 ha of natural vegetation and 90% of the riparian habitats of the Fundão, the North Gualaxo and the Carmelo Rivers. In addition, due to the action of ocean currents in the Atlantic, fine suspended sediments have interested marine habitats of the Brazilian coast. Figure 1.9 allows knowing the scale of disaster.



Figure 1.9. A representative picture about the Brazilian disaster: aerial view of the Rio Doce where the river joins the sea. Source: Nasa Earth Observatory.

ii. *Socioeconomic impacts:*

The mud tsunami immersed the small district of Bento Rodrigues, destroying a large part of the city including cultural heritage and displacing its entire population (600 people). Moreover, it tragically killed at least 19 people (Marinha do Brasil, 2015).

The disruption of ecosystem services along the Doce River poses direct and indirect impacts on livelihoods and health of human populations living in basin's are. In particular, 41 downstream municipalities along the margins of the Doce River lost access to fishing resources, clean water, crop production sites, hydroelectric power generation and raw materials. These events were very damaging to local economies especially for what concern fishing (the primary resources for indigenous people like Krenak tribe) and mining employments. As well as described by Fernandes in 2016, the whole economic loss is estimated in over 20 billion dollars.

1.5.2 | Hungary: Ajka red mud disaster

The accident of the Ajka Aluminum Factory was a serious industrial accident occurring in the western part of Hungary on 4th October 2010, about 160 kilometres southwest of Budapest (Jha, 2010). Figure 1.10 offers a territorial framing by aerial images.

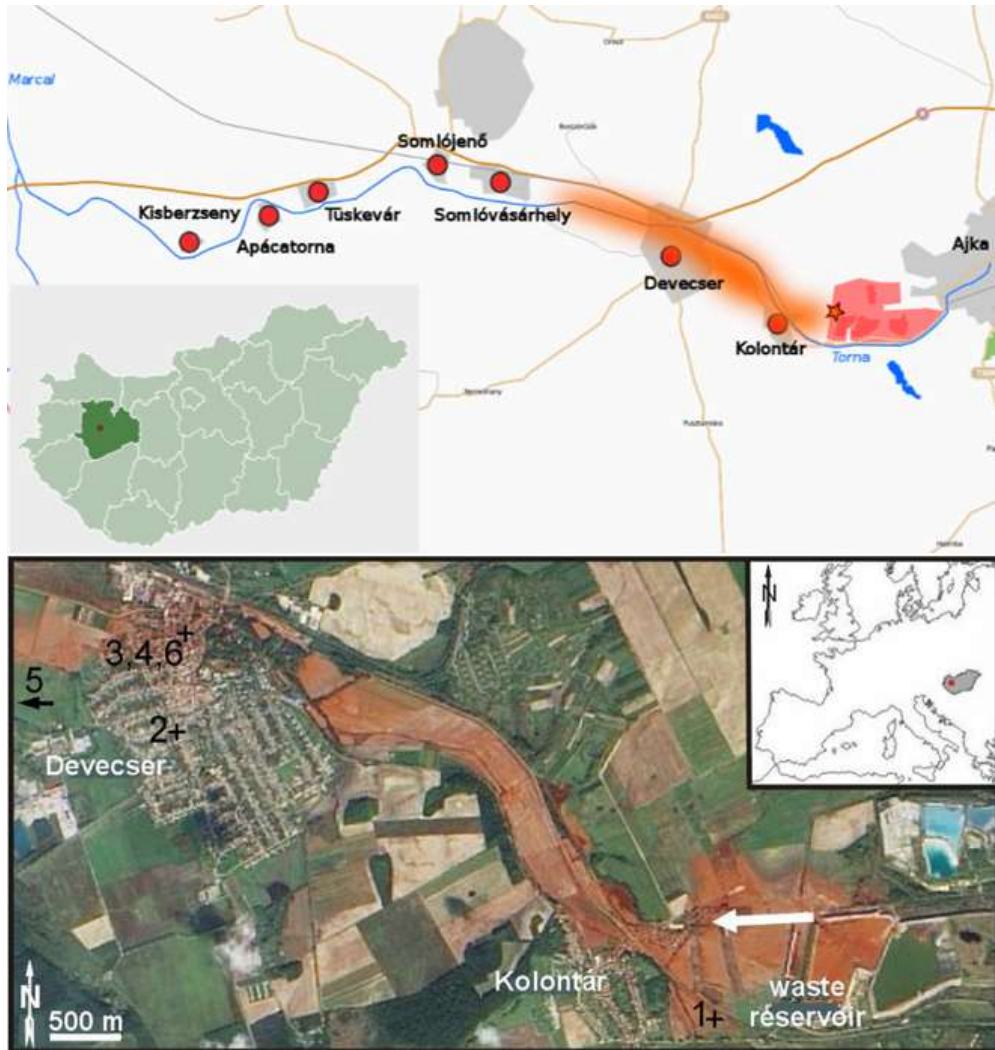


Figure 1.10. Territorial framing of the disaster. Source: modified by katasztrofavedelem.hu and Gelencsér et al., 2011.

That day, the north-western part of a vast sludge reservoir of an aluminium factory near Ajka city suddenly gave way freeing an impressive mass of about 1,000,000 cubic meters of water and red sludge (Mayes et al., 2016). This mud was a by-product of the production of alumina from bauxite in the Bayer process, which involved reactions with NaOH at high temperature and pressure (Gelencsér et al., 2011). The same authors shows in his work the composition of red mud, as reported in table 1.4:

Table 1.4. Minerals identified in red Mud their probable origins.

| mineral identified by XRD and/or TEM | nominal composition | probable origin |
|---|---|----------------------------------|
| hematite | Fe ₂ O ₃ | bauxite |
| cancrinite | Na ₆ CaAl ₆ Si ₆ (CO ₃) O ₂₄ · 2H ₂ O | alumina production |
| "hydrogarnet" | Ca ₃ AlFe(SiO ₄)(OH) ₈ | alumina production |
| calcite | CaCO ₃ | bauxite or alumina production |
| perovskite | CaTiO ₃ | bauxite |
| boehmite | AlO(OH) | bauxite |
| gibbsite | Al(OH) ₃ | bauxite or alumina production |
| quartz | SiO ₂ | bauxite or soil |
| albite | NaAlSi ₃ O ₈ | soil |
| muscovite | KAl ₂ (AlSi ₃ O ₁₀)(OH) ₂ | soil |
| rutile | TiO ₂ | bauxite |
| gypsum | CaSO ₄ · 2H ₂ O | cleanup procedures |

After collapse, the toxic material flowed out the riverbank invading the surrounding areas. In next days, starting from the hydrographic network close to the mine, the mud reached the Danube River, with tragically consequences on ecosystems caused by the high level of pollutants found into mud. As reported by Mayes in 2016, chemical analyses following the disaster identified short-term and long-term impacts.

The first are tightly bound to salinity stress and the caustic nature of the spill material, characterized by a high concentration of metalloid.

Secondly, as a long-term impacts, it has been recognized a salinization of soils and potential nutrient enrichment because of phosphorus in the red mud suspension.

However, the environmental restoration of the Torna-Marcál river ecosystem has been favored by the fine grain of red mud, and especially because the high concentration of the most toxic heavy metals (i.e. As, Cr, Ni, V) was within the finer mud fraction (Anton et al., 2014).

1.5.3 | Utah – USA: Bingham Canyon Copper mine disaster

The Bingham Canyon Mine (figure 1.11), also called Kennecott Copper Mine, is an open pit porphyry-copper mine placed in Oquirrh Mountains, in southwest of Salt Lake City (Utah, USA).



Figure 1.11. Territorial framing of the mine, placed in Utah. Source: modified by Google Earth 2017.

It is one of the bigger artificial excavation worldwide with a size of 0.97 km deep and 4 km wide (Tarolli et al., 2016) and, covering approximately 770 ha of soil, produced more than 19 million tonnes (Jasmine, 2016). This area became famous also due to a massive landslide that affected the mine during April 2013. In fact, the north-eastern wall of the pit collapsed in two distinct episodes lasting ~90 seconds, and separated in time by ~1.5 hours (Pankow et al., 2014). The extension of debris flow deposit is represented in figure 1.12.



Figure 1.12. Debris extension in the mine. Source: modified by Earthobservatory.nasa.gov.

As describe in a Pankow et al's work, the *Rio Tinto Corporate* compared DTM from before and after the event estimating a landslide moving of 165 million tonnes, comparable to approximately 55 million cubic meters (Rio Tinto Corporate, 2017). In addition, he cited that this fact represented the largest non-volcanic landslide to have occurred North America in modern times, overcoming the rock avalanche took placed in Alaska in 2012 and the Mount Meagr rock side in British Columbia (characterizes by about 50 million cubic meters magnitude).

Luckily, the Bingham Canyon event did not lead to casualties among miners, even by the presence of sensors capable of monitoring the geotechnical stability of the quarry. Furthermore, studying the statistics related to these types of events, it is possible to affirm that the early-warning monitoring systems are indispensable for human safety for avoiding environmental disaster.

1.6 | Mining activities monitoring using Remote Sensing

The main impact of mining on the earth's surface is certainly soil consumption and erosion. This chapter introduces these aspects and proposes remote sensing as a monitoring technique. Some operational examples that associate a technique with mining will be reported in the next chapter.

Soil erosion is one of the most severe environmental problems. In fact, it removes soil rich in nutrients and increases the natural level of sedimentation in rivers, leading to the reduction of their storage capacity. In addition, it is a complex combination of changes in land use, increase of agricultural practices, urban expansion and intense rainstorms and, furthermore, it may be accelerated by climatic change towards a more forceful hydrologic cycle (Pandey et al., 2007).

Another primary issue related to soil erosion is the decrease of fertile soil layer (Lal, 1998), that may lead to different consequences: 1) socio-economic problems related to an increase in the costs for cultivation due to the lower natural productivity of soil. 2) Materials from erosion could be spilled in the hydrographic network and in closer lakes, in extreme cases with mud or debris flow with, often, serious danger for infrastructure.

Because of this, the design of an appropriate soil use plan becomes a strategic point for a better territorial development not only for reducing the related hazard, but also for optimize resources. Therefore, will be more and more important to analyse the erosion hazard, identify a priority-scale inside the watersheds and monitoring any critical issues. In this way, is possible to decrease the likelihood of genesis disastrous events.

Due to the complexity of the variables involved in erosion, it becomes difficult to measure or predict the erosion in a precise way. In fact, soil erosion is the result of the interaction of several factors alternating in a complex and articulated way. For this reason, the analysis and the correct quantifying of it may become highly complicated (Pandey et al., 2007). This theme also takes on greater value when it comes to possible complications, first of all the safety of people. For this reason environmental monitoring and the survey of the Earth's surface assumes a fundamental and strategic role.

The continuous technological progress that involves the environmental field is leading to the birth of increasingly precise and reliable technologies for the survey, identification, monitoring and classification of resources. In recent years, for example, optical sensors mounted on

satellites in orbit in space are continuously observing the Earth's surface, storing and processing millions of information relating to the Earth's surface (Datu et al., 2003).

This operating methodology is called Remote sensing, or, as defined by Sabins in 1999, “The science of acquiring, processing, and interpreting images and related data, acquired from aircraft and satellites, that record the interaction between matter and electromagnetic energy” (Sabins, 1999).

These skills allows countless applications in environment field and for surveying and monitoring the soil. In fact, it is used for resources exploration.

For example, as cited by Sabin in 1999, it is used in this way in two different applications: 1) for mapping the geology of an area in order to identify ore deposits and eventual faults and fractures; 2) for recognizing hydrothermally altered rocks by their spectral signatures.

These imagines may be acquired taking advantages by different techniques and instrument. For example it can be done using satellite’s sensor (one of the most famous database is powered by Landsat Project, since 1972, observable in figure 1.13, and special optical instrument mounted on aircraft with or without pilot.

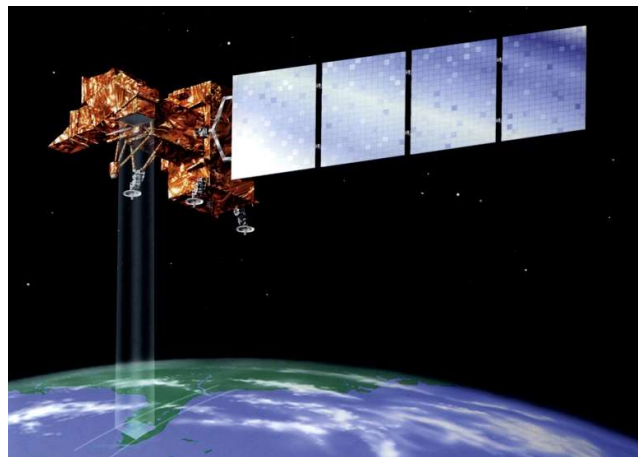


Figure 1.13. Representation of Landsat 7 working in space orbit. Source: Landsat.gsfc.nasa.gov.

How Sabin continues in his work, images acquired by satellite systems have different advantages, as archives worldwide data in readily and available database, with images that cover large areas of the Earth’s surface. In addition, these data are often not too much expensive in relation with the size of zone.

Regarding without-pilot system, it is called UAV. This term is defined as “uninhabited and reusable motorized aerial vehicles”, which can be remotely controlled by means of autonomous,

semi-autonomous or manual operations. The UAV systems are based on multiple low-cost and conventional platforms and are equipped with multiple flexible and efficient sensors. Moreover, it is able to acquire high-resolution images for photogrammetric and remote sensing applications platforms (Tong et al., 2015). Next figure 1.14 shows an example of UAV.



Figure 1.14. An example representing a drone flying over an open-pit mine. Source: modified by simtop.es.

The applications of these tools are countless. In the environmental field, for example, NASA Dryden Research Center, NASA Ames Research Center, and NASA Goddard Space Flight Center have developed a special UAV systems able to monitor the state of forests worldwide through special sensors (Zhou, 2009). Other similar instruments, sensitive to different wavelengths and capable of classifying the soil according to the reflectivity of its constituent objects, are able to offer rapid and precise measurements in case of natural disasters and emergencies and to monitor cities and buildings on the Earth's surface.

1.7 | Goals of the thesis

The main goal of this thesis is the geomorphological analysis of an open-pit mine in Miyun County, near Beijing, PR China. The thesis focuses on the use of Unmanned Aerial Vehicles (UAVs) for high-precision topographic surveying in order to identify and quantify the impact of mining activities on the Earth's surface.

First, after a preliminary phase characterized by drone setting and flight planning, the possibility of using the UAV for the construction of accurate digital surface models (DEM) is reported.

In particular, using SfM photogrammetric technique for the construction of point clouds, two DEMs were generated, respectively for the 2014 and 2016 surveys.

Secondly, two types of analysis were carried out based on the two DEMs:

- i. Mono-temporal geomorphological analysis of each of the two DEMs, such as elevation, slope, roughness and surface curvature analysis;
- ii. Multi-temporal analysis for the comparison of the two surfaces in order to a) highlight significant changes in the Earth's surface and b) quantify these changes in terms of volume and tonnage.

Finally, by directly exploiting the two clouds of points that were suitably cleaned and aligned, this work analysed the subsidence of the surface of some roads inside the mine.

2 | REMOTE SENSING

As mentioned in chapter 1.6 above, soil erosion, especially in the case of mining activities, requires a detailed study in order to highlight its characteristics. Modern Remote sensing techniques (satellite, drone or aircraft) offer extremely interesting data to understand the topography of the soil and to highlight those changes that could be critical.

For this reason, here is described in detail some remote sensing techniques used in scientific research with particular attention to mining activities.

In particular, at first are listed only some of the most common applications of this technology in socioeconomic and environmental fields, with a focus on mining. Still later, starting from an in-depth study of some of these, here will be described the UAV technique as very interesting way for Earth surface surveying with high precision and relative low costs.

2.1 | Remote sensing for land surface changes

Remote sensing is defined as: “The science and art of obtaining information about an object, area, or phenomenon through the analysis of data acquired by a device that is not in contact with the object, area or phenomenon under investigation” (Lillesand et al., 2014).

With the rapid and continuous development of the Digital Era since XX Sec., remote sensing (refer to the introduction for more information), as well as the completely technological world, has had a strong expansion. Remote sensing capabilities are mainly based on advanced hardware technologies that, supported by suitable processing software, allows to process an image and providing a simple read-out version to decision makers (Hardin et al., 2013). As the authors continue, hyperspectral remote sensing of the Earth has significant application in different majors as atmospheric science and climatology, agriculture, geology, forestry, hydrology, environmental and urban areas monitoring.

Next sectors synthesizes some of these applications and show some application examples.

2.1.1 | Remote sensing and Land Change Science

Because of the ever-increasing rhythm of Earth's surface changes and given the extreme importance that the scientific community is addressing about this topic, many authors have proposed the Land Change Science (LCS) as important research topic for studying the interactions between man and environment (Gutman et al., 2004).

Remote sensing is a technique that even in this case can provide a large database of data, even of different space-time nature. They allow to observe the changes occurring on the Earth's surface and offer great material to understand how man's decisions are reflected in the composition of the environment. Through remote images is possible to understand what types of change are taking place, where and when they have occurred (and at what rate) and, finally, what are the factors that actually affect each of these.

For example, to understand the potential of remote sensing in the field of land use change, is possible to appreciate the following multi-temporal map of the use of soil (figure 2.1), in which the massive expansion of the urban area (grey colour) of Shijiazhuang, China, can be detected (Xiao et al., 2006).

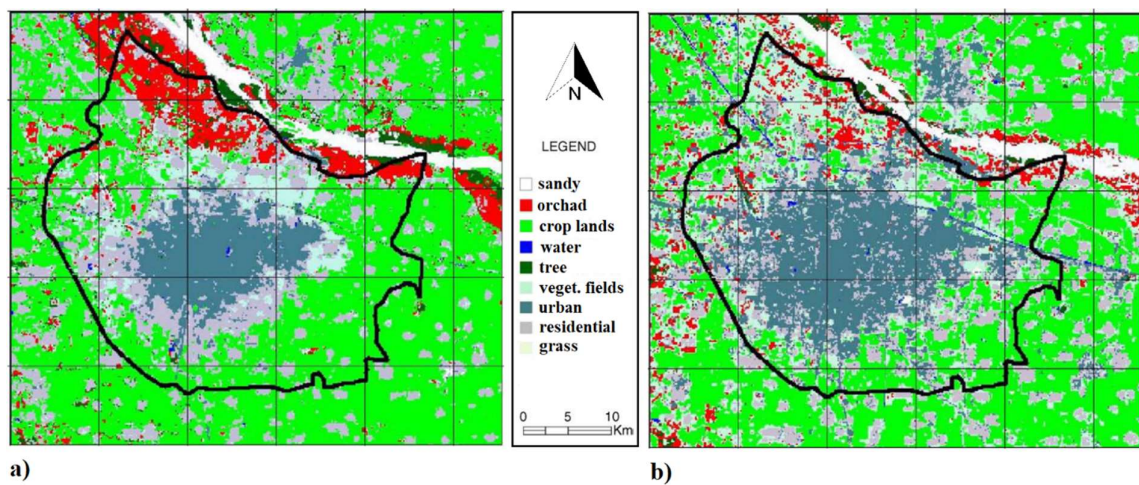


Figure 2.1. Maps of the land use of Shijiazhuang area (China) in 1987(a) and 2001 (b). Modified by Xiao et al., 2006.

In particular, remote sensing can offer interesting opportunities for the urban environment, with good socio-economic findings. Hardin in 2013 shows that, by remote sensing images, it is possible to identify building materials in constructions and checking their wear condition, as well as is possible monitoring the asphalt preserving state of city roads.

As an example to understand the potentialities of this technique is interesting to mention a study conducted in Italy that shows the possibility to use hyperspectral imageries for identifying the presence of asbestos in constructions, a building material banned due to its toxicity (Bassani et al., 2007). In next figure 2.2 a result of this research.

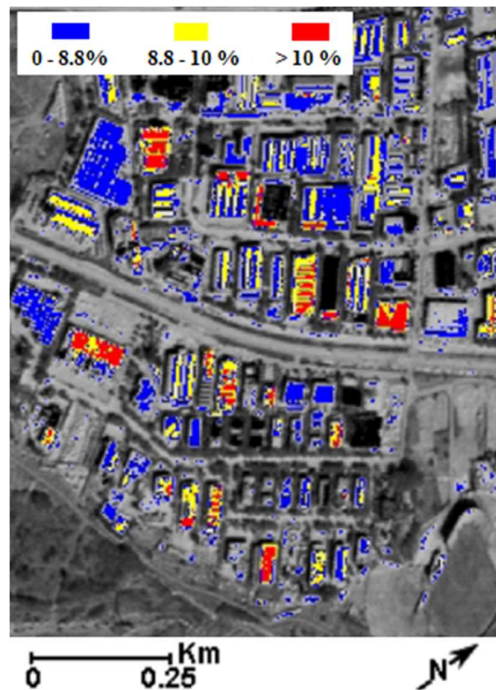


Figure 2.2. Deterioration status assessment of AC roof. Three levels (low, medium and high) respectively in blue, yellow and red. Rimini, Italy.

2.1.2 | Other example applications of Remote sensing

Another interesting example of Remote sensing is about the study of Meteorology, Climatology, hydrology and ecology.

The use of remote sensing images, in close collaboration with the use of Geographical Informative Systems software (GIS) for spatial analysis, can offer a great source of data in this field instantly and on a different scale. In fact, it allows focusing scientific research on a scale of cities, nationally or even globally (Tomlinson et al., 2011). As authors continue, despite the need for an initial high cost in terms of research and equipment, Remote sensing allows an improvement in studies conducted with the only traditional in-field techniques.

Another interesting application of Remote sensing can be found in the monitoring of the particulate aerosol in the atmosphere. For example, it is possible to study the daily distribution

of aerosols in air masses above the continents via MODIS and dark land targets (Kaufman et al., 1997).

In addition, satellite image observations can be extremely interesting for hydrologic basin analyses and, specially, for the analysis of one of the most important component of this major: rainfall. Especially with the development of the NASA's Earth Observing System space program, and with the advancement of more accurate mathematical models, Remote sensing can offer many benefits in the study of land surface water balance, such as rainfall estimation, evapotranspiration, glacier and snow observation, water storage capacity of soil and moisture measurement (Tang et al., 2009).

Another important use of Remote sensing concerned Ecology. In fact, the analysis of the distribution of ecosystems on the Earth's surface can provide an excellent starting point for understanding the evolution of land use in an area. Different patterns of vegetation, in fact, can reflect innumerable ecosystems closely linked to each other and with high ecological value. Biodiversity, for example, one of the key parameters for ecological analysis of an area, can be mapped based on the species richness, or the number of species that can be found within that area. In addition, some authors are recently studying the development of models able to understand how ecosystems can respond to anthropogenic impact, estimating the variation in composition and dynamics within plant communities(Ustin et al., 2010).

One of the most commonly Remote sensing tool used in Ecology the NDVI index variation in an area. It, which means Normalized Difference Vegetation Index, is a satellite-based vegetation index that correlates strongly with aboveground net primary productivity (Pettorelli et al., 2005), and it is closely related to soil species richness and can be used as a tool for the construction of ecological maps.

2.2 | SAR, Lidar & UAV Technologies

2.2.1 | SAR Technologies

Firstly, SAR is an abbreviation of ‘Synthetic Aperture Radar’, a radar Remote sensing technique developed since the 1950s that enables to obtain high-resolution images from space, to recognize objects on Earth and to evaluate their spatial-temporal modifications.

The feature that distinguishes the SAR system is the type of emission of radar pulses, typically via microwaves. Differently from other techniques, the SAR radar emits microwaves laterally, allowing the sensor to analyse the elements on the Earth's surface at different times. The lateral pulses of the radar form the lines of the image (i.e. the range dimension), while the azimuth dimension of the image is formed by the movement of the sensor, that continuously sends and receives the radar pulses (CNR, 2018). The following figure 2.3 shows a typical operating scheme of the SAR technology, (Unipi, 2016).

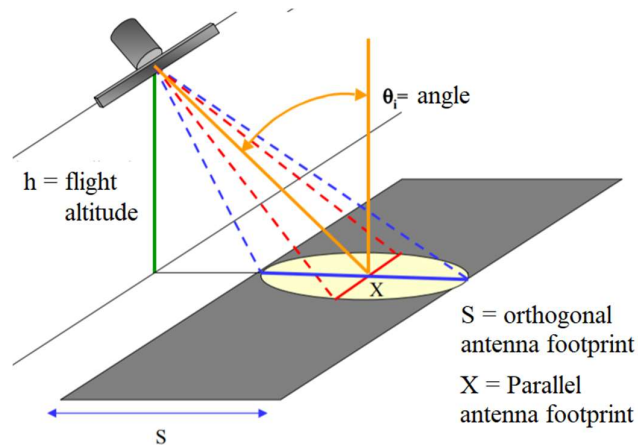


Figure 2.3. Operating scheme of SAR technology. Source: modified by: <http://www2.ing.unipi.it/>

The radar and the SAR system record the time when the pulse is returned, its power and the microwave phase. Analysis of this information produces an interferogram between the two SAR data acquisitions. It can be InSAR (or radar interferogram) or DInSAR (or differential interferogram). By comparing different images, it is possible to obtain three-dimensional images of the Earth's surface, allowing an accurate measurement of the topographical forms. Working on two different images taken at different times, this technique allows to evaluate any changes and deformations that have occurred on the ground (Sousa et al., 2013).

In the mining sector, SAR is used to monitor the area of interest, particularly to show changes over time through multi-temporal acquisitions. One of the most significant case is the analysis of the subsidence (Baek et al., 2008). As example, next figure 2.4, modified by Beak et al (2008), shows a subsidence detection of the interest area using SAR.

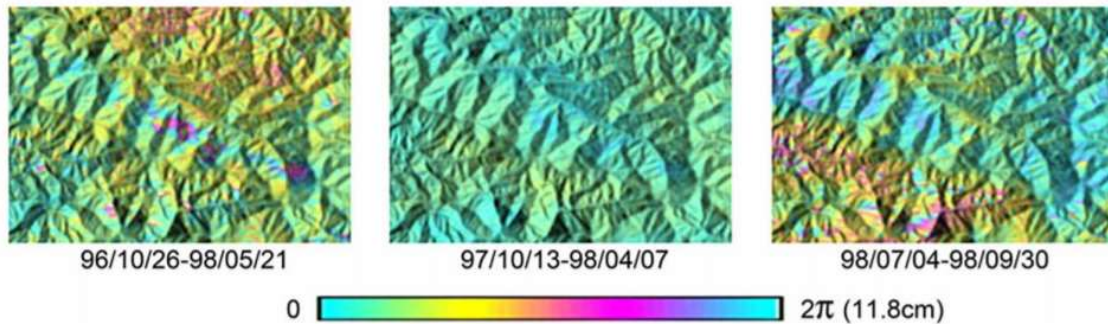


Figure 2.4. Interferograms derived from JERS-1 SAR. Modified by Beak, 2008.

Another example in mining field is about Deutsche Steinkohle AG (DSK), a German coal mining company, that due to legal requirements has been obligated to assess environmental impacts and to forecast effects of current excavations and, for do this, has started to use and invest in SAR technology (Wegmuller et al., 2000).

2.2.2 | Lidar Technology

Another very common technique is the Lidar technology (topographic Lidar or Laser Altimetry), born in the 60's and acronym for “Light Detection And Ranging”. It is an active Remote sensing instrument that is based on the use of specific laser sensors for monitoring the Earth’s surface (Marcoe, 2007) and usable in different applications.

The basic concept is to measure the time taken by a laser pulse to travel from the sensor to a target at a certain distance (i.e. the ground or the interested object to study). As Marcoe (2007) continues, the pulse can be described by a frequency and wavelength measurement: they are usually high frequency waves (between 10 and 150 kHz) and with wavelengths between 1.0 μm and 1.5 μm for surface morphology studies and between 0.50 μm and 0.55 μm for bathymetric studies. Subsequently, the laser pulse is reflected on the object concerned and returns to the instrument where it is collected by a special telecopies. The pulse travel time, once known the length and frequency of the wave, is finally converted to a distance. Next figure 2.5 shows an example of a technical scheme about Lidar components.

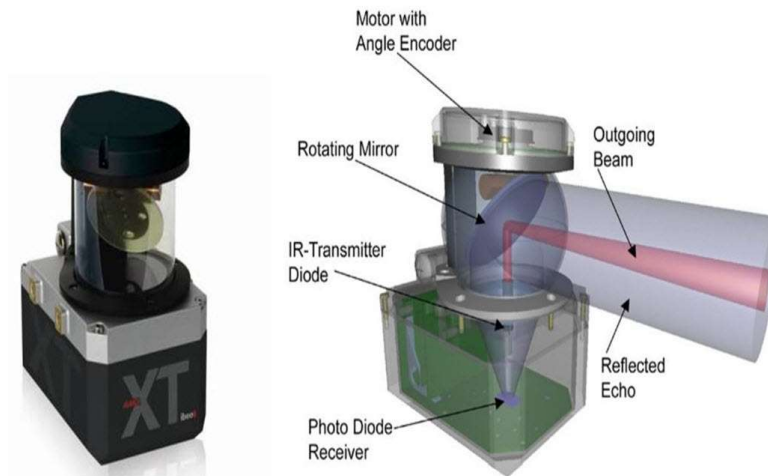


Figure 2.5. Light Detection and Ranging Systems Components. Source: <https://www.elprocus.com>

In addition to direct measurement between the points of the system where it works, the scanner is constantly georeferenced by a GPS device mounted inside the main body. This is true both for terrestrial instruments (where there is a single position because the scanner is not moving) and for moving systems. The second (performed by Airborne or special land conveyance) is more complicated because the motion increases the number of variables in the system.

In this way is possible to obtain a *point cloud*, or a very high number of known-coordinate points with known relative distance. It is the result of Lidar survey and consist in a 3D-mathematical representation of reality (Amato, 2017). Furthermore, starting from these data is possible to perform countless post-processing operations for different types of work. Next figure 2.6 shows an interesting example about Lidar technology and as the 3D model (the result of scan) can appear.

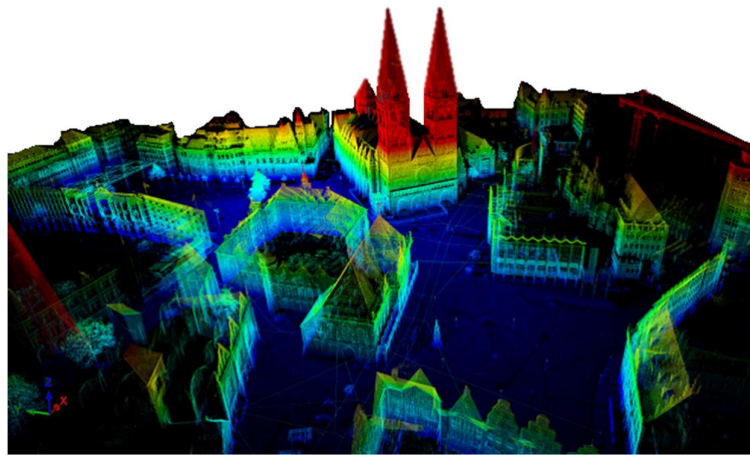


Figure 2.6. Lidar scan of the city of Bremen, Germany. Modify by Dorit Borrmann, and Jan Elseberg from Jacobs University Bremen

Although this method was extremely expensive during the first years of application, in recent years the cost of Lidar data acquisition has been greatly reduced thanks to the technological evolution that are undergoing hardware components (Chen, 2007). For this reason, Lidar is having a strong growth in application both in terms of private investment (eg topographic or forestry professionals) and in the public domain (several Country published these data in opportune databases).

Lidar classification systems are varied and based on different parameters. An example of classification might be the location where the sensor is located. If the sensor remains on the ground it is referred to as T-Lidar (or Terrestrial Lidar), whereas if it is mounted on a flying aircraft, is called Aerial-Lidar.

First of all, the T-Lidar is a quick and precise tool that enable the representation of the reality in which it works through a three-dimensional (3D) mathematical model consisting of a point cloud (Othmani et al., 2011). The laser beam is emitted from an instrument component that is mounted on a known position rigid stand (i.e. it is possible to georeferencing the emission point using GPS coordinate). Automatically, starting from the emission of laser beam, the machine allows scanning the entire surrounding scene through a planar and vertical rotation of the sensor. Initially, this operation allows calculating the distance between the instrument and the target of beam and subsequently a software reconstructs the point cloud composed by millions of points (Dassot et al., 2011). The following figure 2 B shows an operating illustration of the instrument.

The second type of Lidar is the Airborne Lidar, performed using an aircraft for having a “top” point of view (please refer to next figure 2.6 b). It is an active Remote sensing methodology (Xiaoye, 2008) capable to mathematically describe a single point in the space in terms of three-dimensional coordinates (x, y, z). This technology is widely used for the construction of digital terrain models (DEMs), an essential starting point for countless post-processing in numerous fields (Hodgson et al., 2005).

Operationally, the laser beam is generally emitted with a wavelength ranging from 0.8 μm to 1.6 μm (Wehr et al., 1999) and pulse is emitted with a frequency up to 250 kHz (Lemmens, 2007). In terms of horizontal illuminated area (footprint) it works with a more or less 1 m in case of small footprint size and few tens of meters in case of large footprint size (Kelly et al., 2015).

The three-dimensional description of the ground is calculated by a software on the base of the time it takes the laser to leave the scanner's sensor (positioned on the aircraft) and reach the target on the ground (using the information from GPS (Liu et al., 2007)). Next figure 2.7 show an example of operating principles.

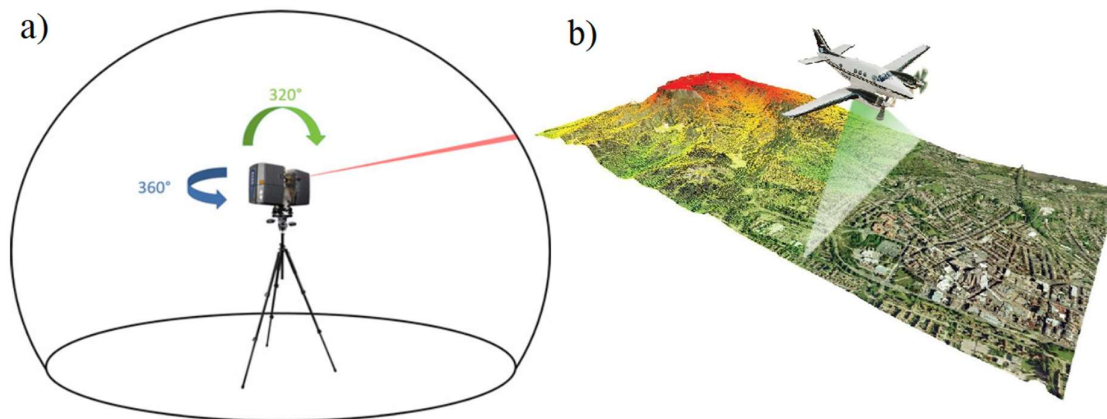


Figure 2.7. a) Operating principle of a terrestrial Lidar scanner during works. Modified by Dassot et. A. (2011); b) Schematic representation of a plane during a Lidar scan. Modified by www.aurorasolar.com

Applications of Lidar in Science are many. In particular, here will be described as examples Lidar in Forestry and Geomorphology.

Within Forestry science, Lidar technology is seeing a strong expansion in terms of operational use. As a demonstration of this, NASA and the University of Maryland, starting from 1997, have launched the VCL project (Vegetation Canopy Lidar) with the aim of creating a three-dimensional map of forests on a global scale for measuring canopy top heights, for studying the vertical distribution of surfaces and for calculating the elevation of ground surface.

These information, together with the age measurement and the conservation status of the forests, the inventory of biomass and the soil uses survey, will be crucial for climate mathematical modelling (and its prediction) on a global scale (NASA, 2003).

Lidar technology is extremely useful in Geomorphology science, too.

Geomorphology is the science that studies the Earth's surface origins and how it varies over time due to the chemical, physical and biological processes occurring on it. These processes, which give rise to the various topographic elements on the Earth's crust (such as mountains, hills, valleys, etc.), are at the base of the landscape. To do this, geomorphology aims to quantify processes that change the landscape through continuous environmental monitoring such as

climatic and meteorological analysis, hydrological analysis of watercourses, glacier studies, monitoring of the tectonic and volcanic activity, observation of biological processes and, last but not least, analysis and quantification of human activity. In addition, another key goal of geomorphology is not just to understand the landscape as it is in the present state (i.e. to interpret the whole of the processes that as a result have led to the surface as we know it), but try to predict how current processes can have an impact on the future landscape (Tooth et al., 1991).

An indisputable starting point for geomorphological analysis in an area is to have accurate and high-resolution data. In particular, any geomorphological analysis must be supported by appropriate maps for knowing and understanding the phenomena in progress and hypothesize its future evolution through the creation of ad-hoc models. The advent of airborne laser technology in recent decades has completely revolutionized data acquisition methodologies making work faster, more truthful and relatively less expensive (Flood, 2001) and useful in different scale.

As example of this and of the potential of high-resolution DTM powered by this technology, is possible to cite the use of Airborne Lidar data for detailed studying of the transition from hill to valley by analysing the relationship between slopes. Another example is the possibility to recognize the topographic signature of a debris flow by studying the slope-area diagram (Tarolli et al., 2009). In addition, an interesting geomorphometric parameter can be used to identify local variations of elevation and slope using Lidar data: the roughness index (Cavalli et al., 2008).

With regard to mining activity, this technology is particularly useful for the construction of high-resolution digital models of excavation areas, the basis for countless subsequent analyses.

An example of an application can be found in the monitoring of coastal dunes in Southern Monterey Bay, California (US), which became sand extraction areas from 1940 to 2004. The estimation of erosion caused by mining activity has been estimated on an annual basis using, among other relevant techniques, Lidar technology (Thornton et al., 2006).

Another interesting example is the use of Airborne-Lidar as a method of surveying in an exhausted mine for environmental restoration. In fact, the automation of Lidar point cloud processing with an appropriate integration into GIS, can help forest managers to take appropriate decisions on silvicultural treatments in areas occupied by a quarry (Wężyk et al., 2015).

2.2.3 | Unmanned Aerial Vehicle (UAV) Technology

The purpose of this chapter is to deepen in detail an important topographic field instrument (and more specifically in the SfM technique and in the aerial photogrammetry) that in the last decades is seeing a very strong expansion: UAV technology.

Specifically, the main features, the most common classifications and some application examples will be described below.

According to the glossary definition of ‘UAV International’, an UAV is an aircraft where the flying pilot is not on board and it is a subcategory of unmanned aircraft (UA). In particular, an UA:

- i. is capable of sustained flight by aerodynamic means;
- ii. is remotely piloted or capable of autonomous operation;
- iii. is reusable;
- iv. is not classified as a guided weapon or similar one-shot device designed for the delivery of munitions. (UVS International, 2012).

The use of these technologies has become ordinary in the military field and, given the extreme versatility that these machines can offer to the operator, is growing increasingly also in the civil sphere in different sectors (subsequent chapters will be dealt with some examples of application).

It is important to remember that not all UAVs are considered the same from the operational point of view. In particular, there are amateur models for recreational dedications only and not subject to particular flight rules and others, and other, more complex and professional, which are often subject to regulation. For example, in Italy, they must be conform to a Navigation Code included in the ENAC Regulation (<https://www.enac.gov.it>).

2.2.3.1 | Classification of UAVs

The world of flying UAVs is very wide and articulated and it is possible to organize classifications based on numerous parameters. In particular, these machines depending on the shape, size, weight, operating radius, construction material, and the type of function for which it has been designed. The following sections aim to deepen two of the main UAV classifications: shape and size.

UAVs classification according to size:

The first proposed classification concerns the size of UAV. In particular, observing the directives of military drones of the United States of America (U.S. Army Training and Doctrine Command - TRADOC, 2010), different groups can be observed. Next table 2.1 shows an example of classification where size, maximum gross takeoff weight, normal operating altitude and airspeed are indicated.

Table 2.1. Classification of UAVs according to size. Source: modified by TRADOC, (2010).

| Category | Size | Maximum Gross Takeoff Weight (MGTW) [kg] | Normal Operating Altitude [m] | Airspeed [km/h] |
|----------|------------|--|-------------------------------|-----------------|
| Group 1 | Very small | <1 | - | - |
| Group 2 | Small | 01-ott | <350 AGL* | <190 |
| Group 3 | Medium | ott-25 | <1000 AGL | <450 |
| Group 4 | Large | <600 | <5500 MLS** | <450 |
| Group 5 | Larger | >600 | >5500 MLS | Any airspeed |
| Group 6 | Largest | >600 | >5500 MLS | Any airspeed |

* AGL = Above Ground Level

** MSL = Mean Sea Level

As described by other authors there are different types of drone depending on the size that, consequently, is reflected on the performance of the aircraft. Below, in figure 2.8, there is an example of classification where the operating altitude and endurance are explained (Watts et al., 2012).

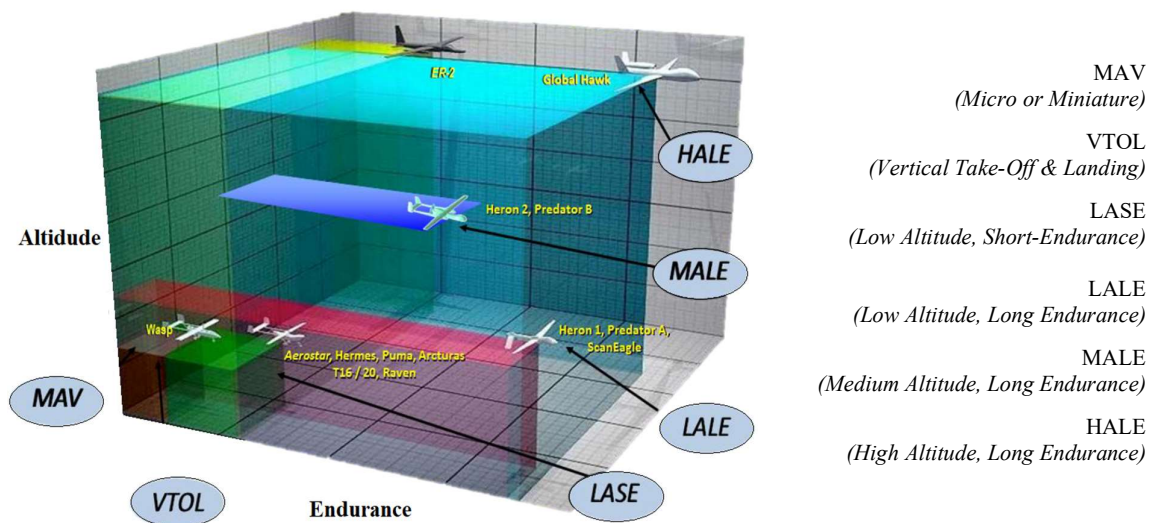


Figure 2.8. Different in endurance and altitude of different UAVs. Source: modified by Watts et al., 2012.

However, it is important to recognize that despite the size of the UAV can be large, civilian topography usually uses small aircraft, characterized by modest weight but easy to transport and with high versatility.

UAVs classification according to shape:

A first fundamental distinction regarding the shape of UAVs is the type of structure: fixed wing or with rotor. This section will show some examples of the various typologies and introduce some key features.

- *UAVs with Fixed-Wing*

Fixed-wing UAVs are very similar to airplanes, consisting of a central body with anchored wings, and are generally endowed of camera. Various models of this type are available on the market which differ in shape and size, but are generally characterized by greater flight autonomy than rotor ones (from 30-45 minutes to several hours - the most influence component about this parameter is certainly battery).

This type of construction, also thanks to the cruising speed of up to 150 km/h, makes this kind of vehicle able to cover considerable areas during a single flight (generally <math><10-12 \text{ km}^2</math>) and to offer great results from a photographic point of view (Clever Drone Maps, n.d.). Furthermore, the aircraft records the main flight parameters (as well as photographs and relative information) and allows downloading data on PC for subsequent post-processing operations.

Next image 2.9 show two different types of UAV with fixed wings.

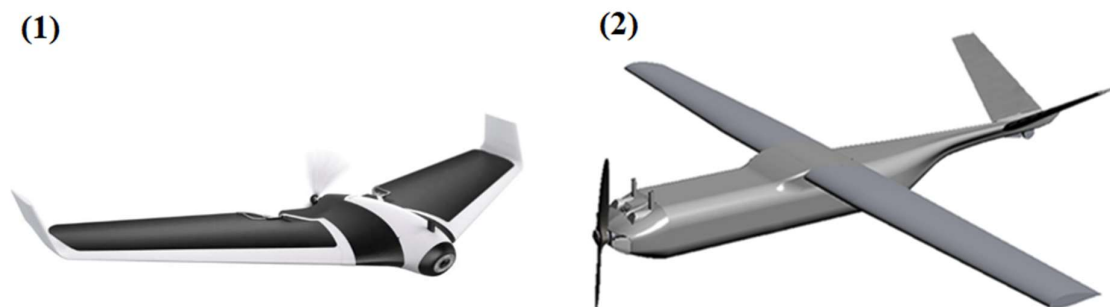


Figure 2.9. Different types of wing in two UAVs. (1) Parrot© DISCO FPV; (2) Aerofoundry© Watupá 300

○ UAVs with rotors

This category of aircraft, commonly known as Remote Piloted Aircraft (RPA) or multi-rotor, consists of a central body (where the camera is attached) and, more frequently, from one to eight rotors. They are remotely controlled by a person on the ground and, in the case of other sophisticated aircraft, from a remote base. Depending on the number of rotors they can be:

- i. *Tricopter*. Nano drones of very small size and with minimum operating radius. They can carry a small camera.
- ii. *Quadcopter*. Mini drones with short operating radius. They can carry a camera and, for example, a FPV (First Person Viewer) for police operations.
- iii. *Hexacopter*. Drones larger than the previous ones, they can carry a camera and a GPS receiver (Global Positioning System) for georeferencing images.
- iv. *Octocopter*. Larger drones, in addition to the camera and the GPS, can be equipped with stabilizers for better picture quality.

The following figures 2.10 show an example of how rotors can be placed around the central body of a drone and some example of different models available on the market. As is possible to observe from the arrows, rotors rotate alternately clockwise and counter clockwise.

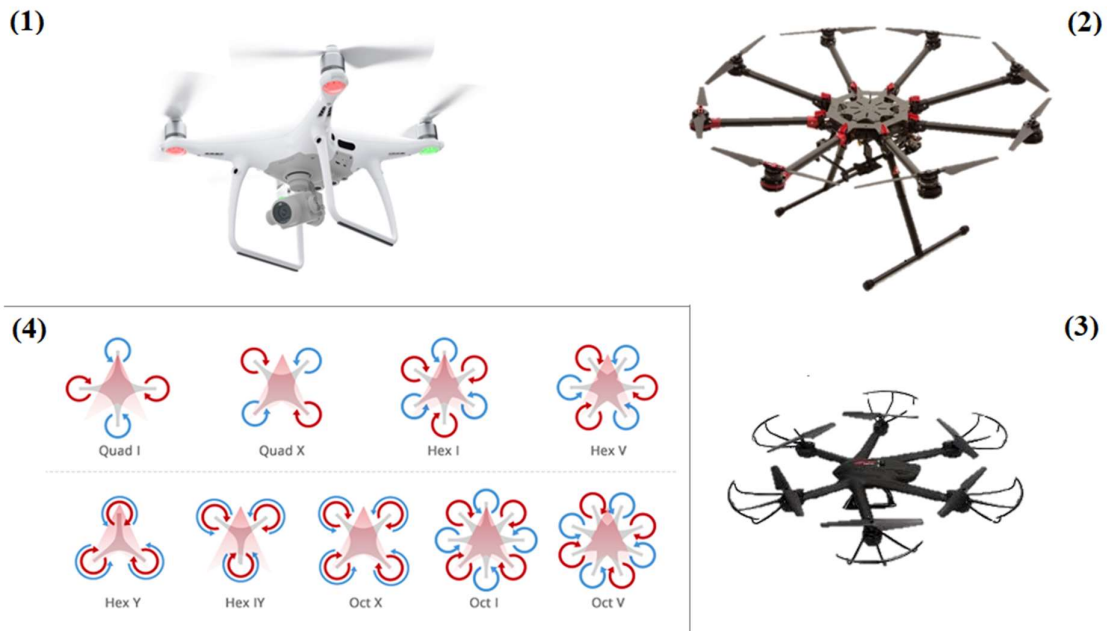


Figure 2.10. Some examples of UAV model: (1) DJI© Phantom 2; (2) DJI© Spreading Wings S1000; (3) MJX© X600. (4) Scheme about different types of multicopter.

2.2.3.2 | Applications of UAVs

Although UAV technology is primarily designed for military purposes (please note the chart 2.1.a), exponential expansion is also being observed in the civil field in recent years (Business Insider Intelligence, 2015). In addition, as can be seen from the chart 2.1.b, estimates conducted on the drones hardware investment suggest a strong increase in the interest in such technology both in the private and in the government domain (Joshi, 2017).

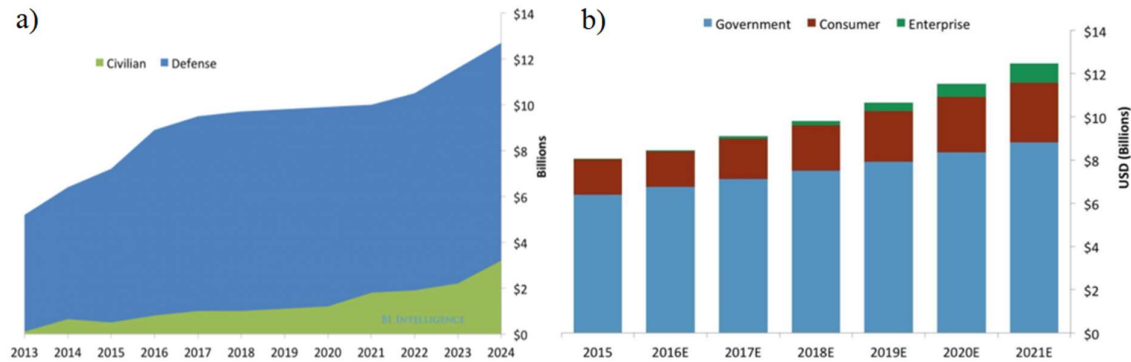


Chart 2.1. a) Estimated investment in drone hardware. Source: Business Insider, Joshi (4th July 2017); b) Estimated investment in drone hardware. Source: Business Insider, Joshi (4th July 2017).

Applications of this technology can be countless thanks to the versatility of the aircraft and simplicity of use (some models can be controlled simply by a smartphone). In particular, the most common applications could be recreational uses, architectural and engineering inspections, support in emergencies (fires, Earthquakes, etc.), urban security (e.g. through FPU), environmental research and analysis, agriculture and aerial photogrammetry (Drone Nodes, 2015). Chart 2.2, always drawn from the article by Business Insider and written by Joshi in 2017, shows some statistics about the use of drones in 2015.

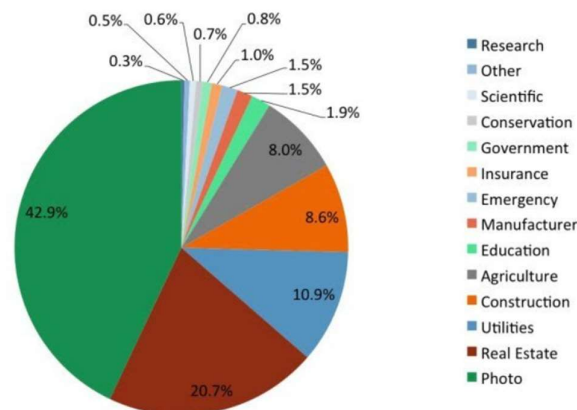


Chart 2.2. Top Industries uses of UAVs. Source: Business Insider, Joshi (4th Juli 2017).

2.2.3.3 | UAVs in geomorphology and mining applications

In the geomorphologic and topographic field (as well as in mining activities), UAV technology is an extremely useful tool as it provides a strategic point of view of the Earth's surface. Additionally, using this technique is possible to map and analyse areas of very different nature and, in particular, it find interesting applications in zones of difficult access for a human operator (Obanawa et al., 2015). UAV allows the use of the SfM technique for building high-resolution digital terrain models in three dimensions starting from a dense cloud points (for deepen this technique please refer to the dedicated chapter).

The following chart 2.3 shows the scope of the main remote sensing techniques: as is possible to observe, UAV technology allows building high quality cartographic products up to about 10 km² (Lee et al., 2015). Limiting elements are certainly the battery life and the high processing time of the data in case of large numbers of photographs and complex surfaces.

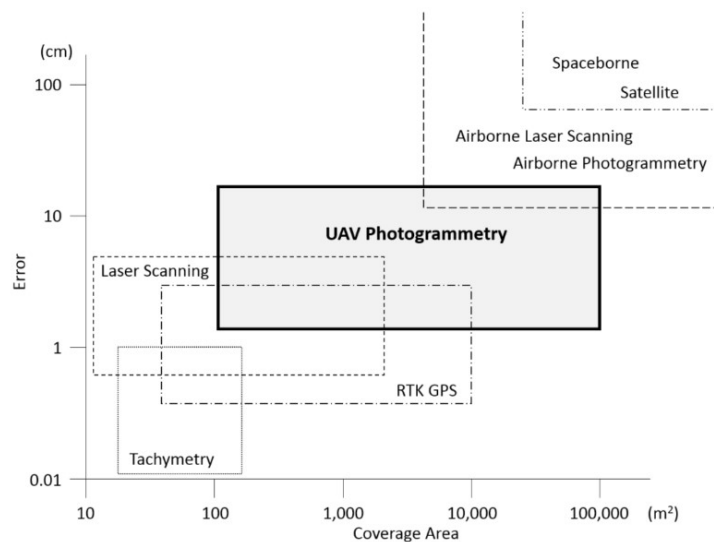


Chart 2.3. Ranges of coverage area and error for each topographic surveying technology. Source: Lee&Choi (2015).

Specifically the drone, equipped with a high-resolution camera, Global Position System (GPS) receiver for image georeferencing and with a software that can calculate the main flight parameters while shooting, allows producing all the inputs needed to start a SfM algorithm. Furthermore, is possible to increase the accuracy of the result introducing recognizable points on the ground (and clearly visible from the photographs) with known x,y,z coordinate (GCP).

Numerous UAV applications in the field of scientific research are described in the literature, with particular focus on the environment. For example, it is possible to quantify the anthropogenic mining impact on the Earth's surface (Chen et al., 2015), study potentially dangerous natural phenomena (Mancini et al., 2013), monitor the biosphere through multi-temporal images (Torres et al., 2014) and to study glacier landforms (Ely et al., 2017). Another very interesting field of application is hazard monitoring and management (i.e. landslides, floods, earthquakes, volcanos, ecc.) using different type of unmanned vehicles (Giordan, 2018). Regarding mining activities, the following figure 2.11 shows an example about how, by flying UAV with camera and GPS receiver and exploiting the potential of the SfM, a Digital Surface Model and a Digital Orthomosaic Model can be obtained used as a starting point for countless post-processing operations.

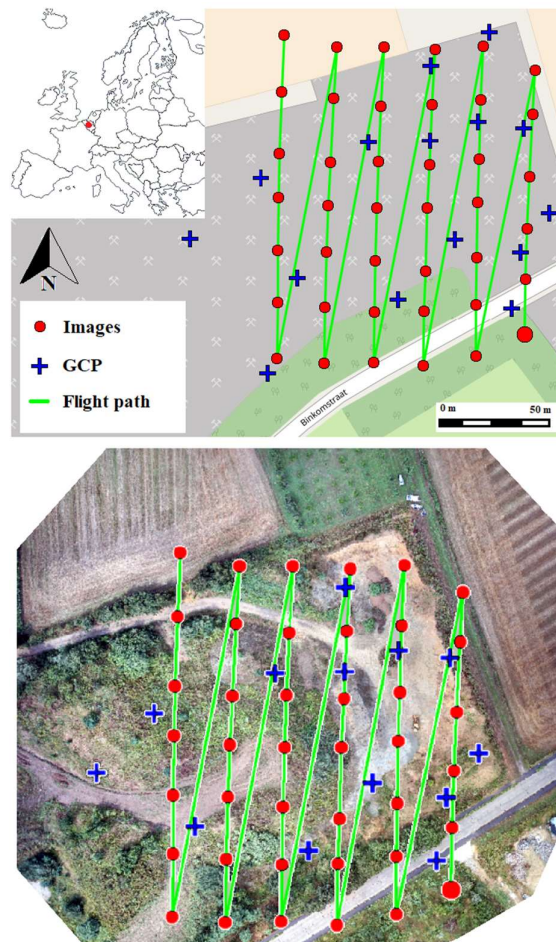


Figure 2.11. Example of the use of UAV for building a 3D-model of Belgium's mine. Self-processing of data kindly granted by China University of Geoscience of Beijing. Map by OpenStreetMap[®] and processing using Pix4Dmapper[®]

2.3 | Structure from Motion (SfM) Technology

“Structure From Motion” (SfM) is a photogrammetric technique that is based on the mathematical interpretation of a series of two-dimensional images representing a real object on Earth in order to create three-dimensional models that can be post-processed in function of the goal of the research (Recker et al., 2014).

Especially in the last decade, this method has become more common because it offers high-resolution results of survey areas, in short time and cheaper in term of cost compare to traditional photogrammetry.

This technology, widely studied and documented in the field of “Computer Vision”, is inspired by the ability of the human brain to interpret the world around itself, for example, through the dosage of lights, shadows and the shades of colours (Georgieva et al., 2008). In fact, the brain, starting from two-dimensional retinal images of a moving scene, is able to rebuild a three-dimensional model to get a more realistic perception of reality.

2.3.1 | Functioning of SfM

In order to make a correct SfM and thus obtain an operating result for subsequent processing it is important to follow some principles.

Firstly, is most significant to know how taking the photographs and how the study area should appear inside the pictures. In fact, the three-dimensional model is based on a series of photographs that must partly overlap, taken as described in the following image (for land-based SfMs). Next figure 2.12 shows how to take the pictures.

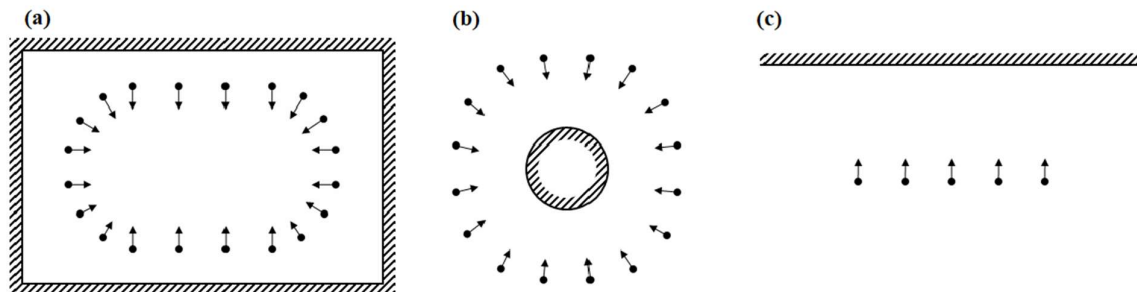


Figure 2.12. How to take pictures for a correct using of SfM. (a) Interior; (b) Isolated object; (c) Façade. Source: modified by Agisoft Photoscan© User Manual

The number of images depends on a number of factors, in particular the resolution of the camera used and the complexity of the object to be detected. Although the minimum number of photographs needed to solve the equation of creating a three-dimensional model is three, the complexity of shape, illumination, and material causes an improve in the number of the images needed (Westoby et al., 2012).

Once finished the first phase that allows the obtaining of input data, using appropriate software such as Pix4Dmapper[®] or Agisoft Photoscan[®], the three-dimensional reconstruction of the scenario is calculated as cloud of points, the output of the model. As can be deduced from the previous two phases, this technique is simple to use and allows qualitative results in relatively fast in field-operating times (the timing varies greatly from the workload, explicitly, the number of photographs to be processed and the complexity of the detected surface) and, comparted with traditional photogrammetry, at low cost.

Although these phases lead to a usable three-dimensional model, it is possible to improve its quality by detecting on the ground some points with known coordinate (x,y,z) called Ground Control Point (GCP). They are highlighted on the ground by using targets and the coordinates are compiled into a .csv format file that can be imported into the processing software to improve the accuracy of the survey. In addition, this process allows georeferencing the output using, for example, using a WGS84-based Coordinate System (Fonstad et al., 2013).

The next image 2.13 proposes a survey scheme of SfM using targets on the ground.



Figure 2.13. Scheme of SfM survey and the position of targets on the ground. Source: www.unvaco.org

2.3.2 | Theoretical application of SfM

SfM's capacity to produce high-resolution digital terrain models in a relatively simple and economical way is leading to an exponential increase in applications in different fields.

Numerous studies have demonstrated the real possibility to analyse the processes occurring on the Earth's surface by finding interesting applications in the geomorphologic, hydrogeological, ecological and engineering fields. For example, some authors have shown that the results obtained through SfM in the analysis of agricultural drainage network, also using common smartphones, are to be regarded as absolutely qualitative and comparable to the certainly more expensive photogrammetry (Prosdocimi et al., 2015). Next image 2.14, from the work mentioned above, is an example of SfM application in geomorphology and show the possibility of build an accurate DEM (0.1 m resolution) for the analysis of rivers.

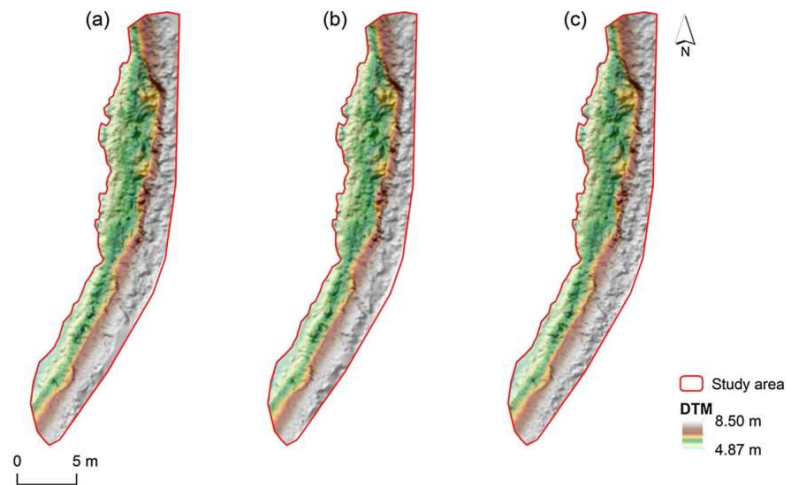


Figure 2.14. DTM (0.1 m resolution) produced by SfM technology. (a), (b) and (c) are different results by using diverse analysis. Source: Prosdocimi et al. (2015).

This technique also offers interesting opportunities when working on items that require very high resolution, even at individual centimetres.

This is the case, for example, of the study of the glacially-sculpted bedrock ridge, where it is advisable to study the micro-topography and roughness of the elements on the ground (Westoby et al., 2012). Other examples in this regard are the analysis of animal-induced erosions (Sofia et al., 2017) or, citing a completely different field of application where is required to observe the smallest detail, archaeological excavations (Green et al., 2014).

The SfM technique is also particular interest in the field of three-dimensional representation, which is very useful both at a scientific level as a basic data for further utilisations and for divulging purposes (one example of this is the three-dimensional reconstruction of archaeological artefacts).

Citing the work introduced in figure 2.17, where a self-processing of a Belgium mine was elaborated with kindly permissions of CUGB, SfM allow to produce a very accurate 3D model (ground resolution is about 10 cm/px). Next figure 2.15 shows a particular of the extraction area in the 3D model, where deposits, roads and a heavy machine are clearly visible.



Figure 2.15. Example of 3D-model in a Belgium's mine. Self-processing of data kindly granted by China University of Geoscience of Beijing. Elaborated using Agisoft PhotoScan©

Also with regard to the SfM technique, of considerable interest is the possibility of estimating volumes starting from the three-dimensional model or the point cloud.

This operation, better described and analyzed in the following chapters in the case study of this thesis, allows to observe in volumetric terms the changes that occur over time on the Earth's surface (if there are multi-temporal surveys), or to calculate on a single 3D model the volume of an element on the ground.

By way of example, and to demonstrate the great versatility of SfM, the following figure 2.16 shows the calculation of the volume (6.2 m^3) of a little deposit in the Belgian mine, performed analysing a point cloud built from SfM.

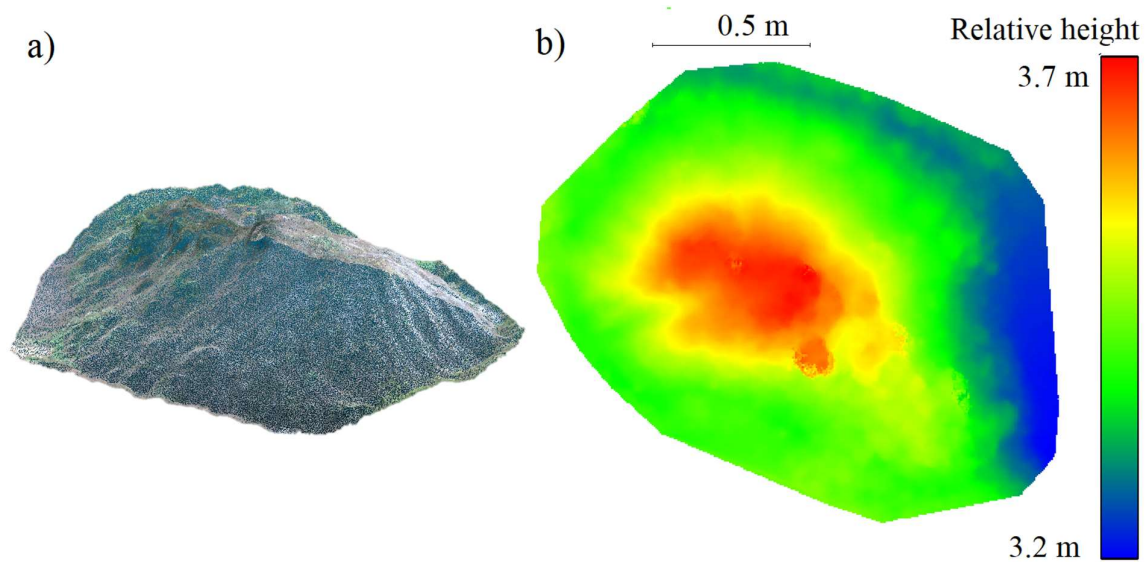


Figure 2.16. Example of volume calculation using data from SfM technology. Self-processed data (using PhotoScan[®] and CloudCompare[®]) kindly granted by CUGB. a) 3D model of deposit; b) relative height for volume calculation.

In the next chapter will be analysed the area of study in which the work of thesis was carried out.

3 | STUDY AREA

The analysis of the open-pit mine object of this thesis work is described. In particular, an analysis of the main mines in the area surrounding Beijing is initially proposed, to offer a regional view of mining activity in this area of China.

Then, the mine under study is described in detail, presenting the main characteristics of the flights such as the route of the UAV and the position of the Ground Control Points (GCPs).

For reasons of privacy, it was not possible to indicate the exact coordinates of the mine under study.

3.1 | Mining activities near Beijing

As a major supplier of raw materials, China's mining industry has expanded significantly in recent years in order to support the economic and demographic development of its population. However, the most obvious side effect of this expansion is the increasing presence of degraded soil. In fact, in China, land degraded by human activity already amounts to about 33 million hectares and soil loss is in constant growth at about 20 thousand hectares per year (Miao et al., 2000).

Based on these considerations, the purpose of this section is to provide an overview of mining activity near the Chinese capital by identifying and analysing the major open-pit mines in the area, in order to contextualise the mine studied in this thesis.

The geographical framework of these mines, in relation to the city of Beijing, is shown in figure 3.1. Subsequently, more detailed maps were produced containing orthophotos using the Basemap service offered by Esri ArcGis®, which clearly show how they are inserted into the territory. These maps are reported in next figures 3.2, 3.3 and 3.4.

For each mine, the perimeter and the area were subsequently measured in order to obtain a quantitative indicator of the mining presence in the area. These operations are shown in the following table 3.1.



Figure 3.1. Geographic framework of the major mines around Beijing. The red box indicates the mine under study. Self-produced data. Source: Google Earth®.

Table 3.1. Main characteristics of the major mines around Beijing. Self-produced data. Google Earth®.

| <i>Mine</i> | <i>Place</i> | <i>Perimeter [km]</i> | <i>Area [ha]</i> |
|----------------|--------------------|-----------------------|------------------|
| <i>Mine 1</i> | Liujiagou | 9.78 | 328 |
| <i>Mine 2</i> | Liuhegoucun | 4.45 | 81 |
| <i>Mine 3</i> | Anzigou | 2.1 | 23 |
| <i>Mine 4</i> | Huangyan | 4.44 | 62 |
| <i>Mine 5</i> | Louboyu | 2.23 | 16 |
| <i>Mine 6</i> | Shangzhuangzicun | 24.8 | 2070 |
| <i>Mine 7</i> | Xiaogangcun | 7.47 | 113 |
| <i>Mine 8</i> | Gaozhuangcun | 9.69 | 162 |
| <i>Mine 9</i> | Taihexing | 6.46 | 87 |
| <i>Mine 10</i> | Zhoukoudianzhen | 3.55 | 50 |
| <i>Mine 11</i> | Nian Kiln Er | 4.95 | 63 |
| <i>Mine 12</i> | Beixiasicun | 2.35 | 19 |
| <i>Mine 13</i> | Shuishanyu | 5.81 | 50 |
| <i>Mine 14</i> | Hulupengcun | 6.91 | 85 |
| <i>Mine 15</i> | Sanhezhuang | 1.69 | 10 |
| <i>Mine 16</i> | Beiwanggezhuangcun | 1.99 | 19 |
| <i>Mine 17</i> | Xilongquancun | 3.42 | 45 |
| <i>Mine 18</i> | Malinsi | 5.57 | 51 |
| <i>Mine 19</i> | Jinjiawa | 10.7 | 270 |
| <i>Mine 20</i> | Nanhecun | 6.67 | 82 |
| | | 125 | 3686 |

As can be seen from table 3.1, the soil eroded due to the major twenty quarries in the region around Beijing is about 4000 hectares. The next figures 3.2, 3.3, 3.4, 3.5 show an aerial view.

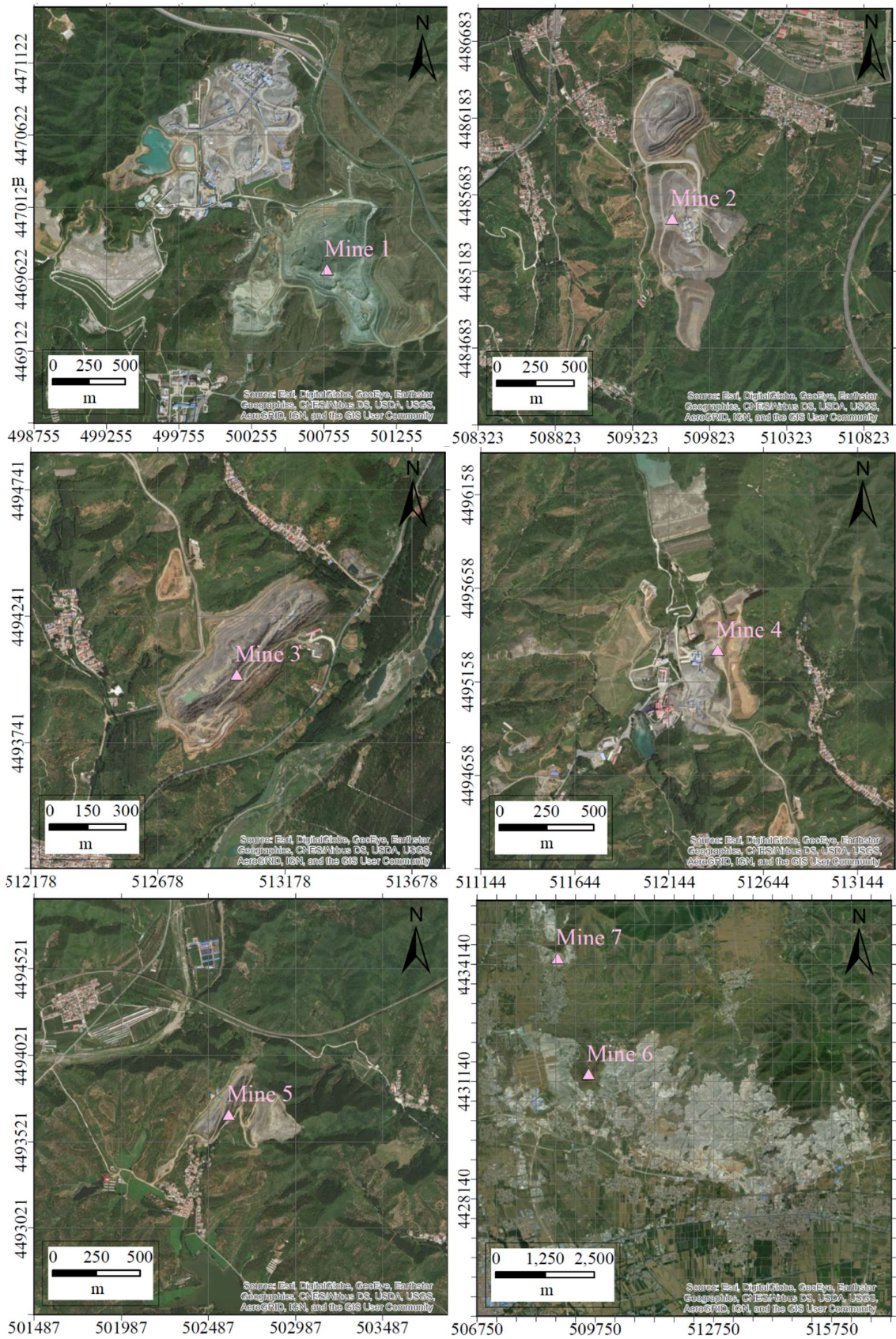


Figure 3.2. Mine 1 to 6. Self-produced data. Source: Esri, DigitalGlobe, GeoEye, Earthstar Geographics, CNES/Airbus DS, USDA, USGS, AeroGRID, IGN, and the GIS user community.

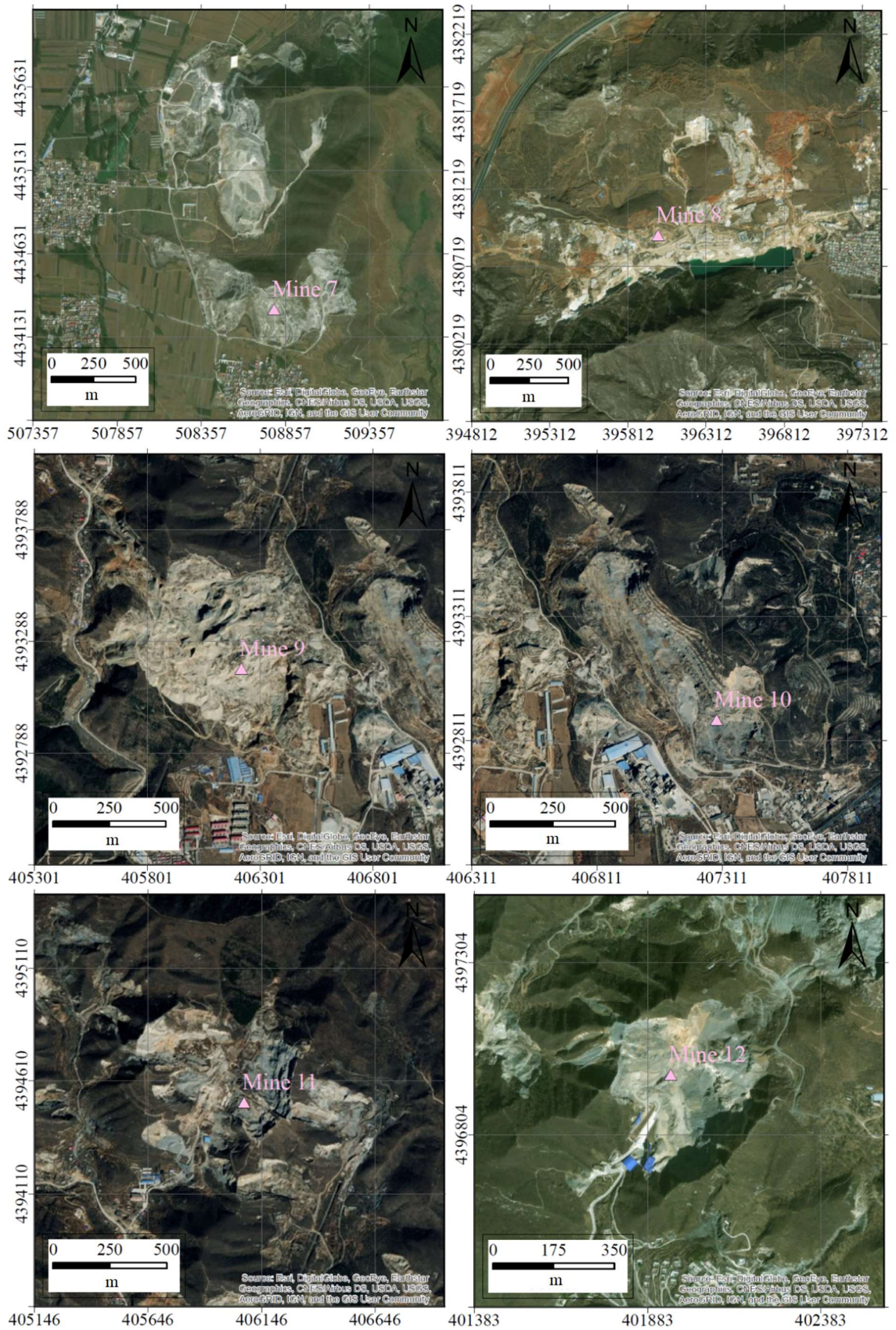


Figure 3.3. Mine 7 to 12. Self-produced data. Source: Esri, DigitalGlobe, GeoEye, Earthstar Geographics, CNES/Airbus DS, USDA, USGS, AeroGRID, IGN, and the GIS user community.

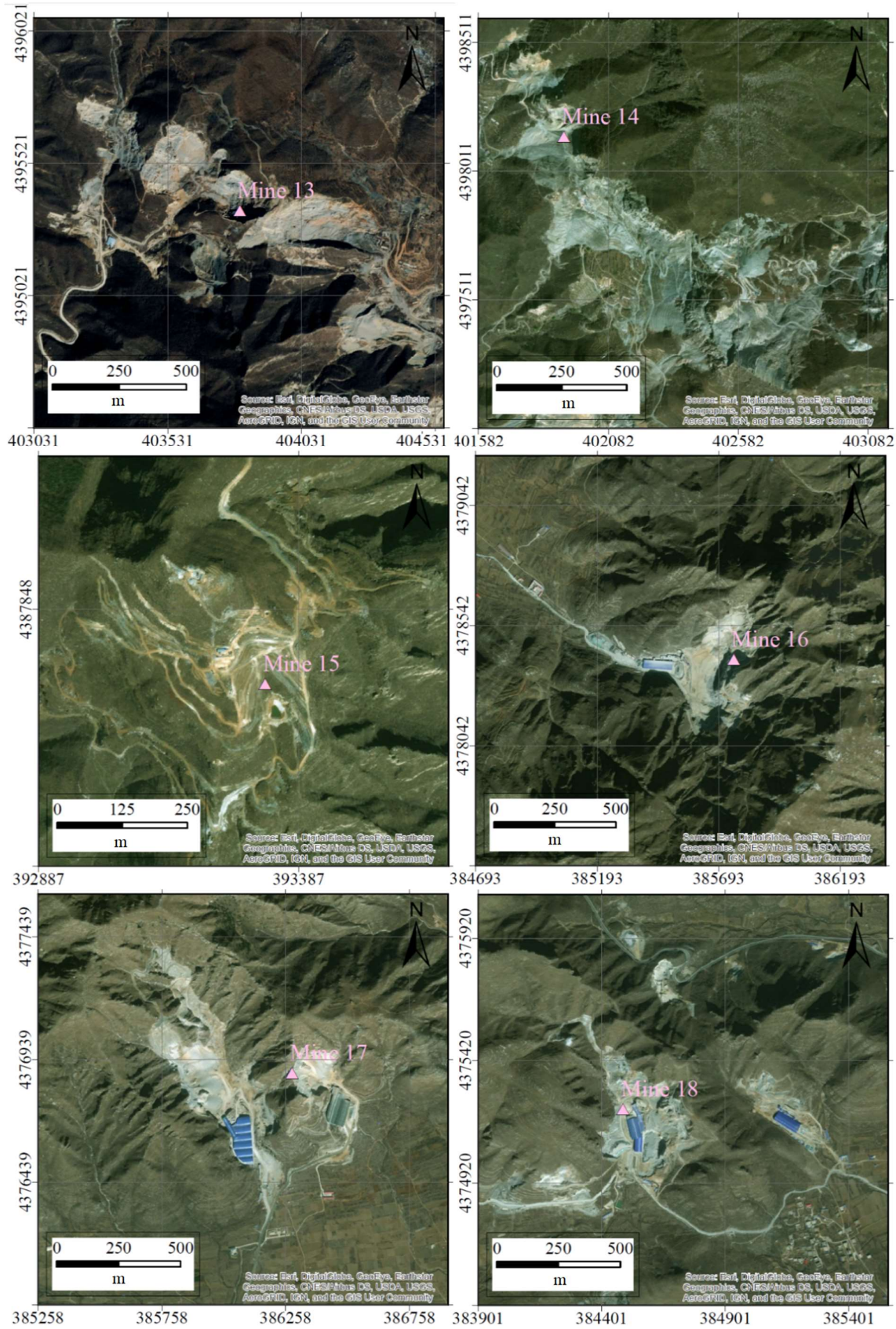


Figure 3.4. Mine 13 to 18. Self-produced data. Source: Esri, Digital Globe, GeoEye, Earthstar Geographics, CNES/Airbus DS, USDA, USGS, AeroGRID, IGN, and the GIS user community.

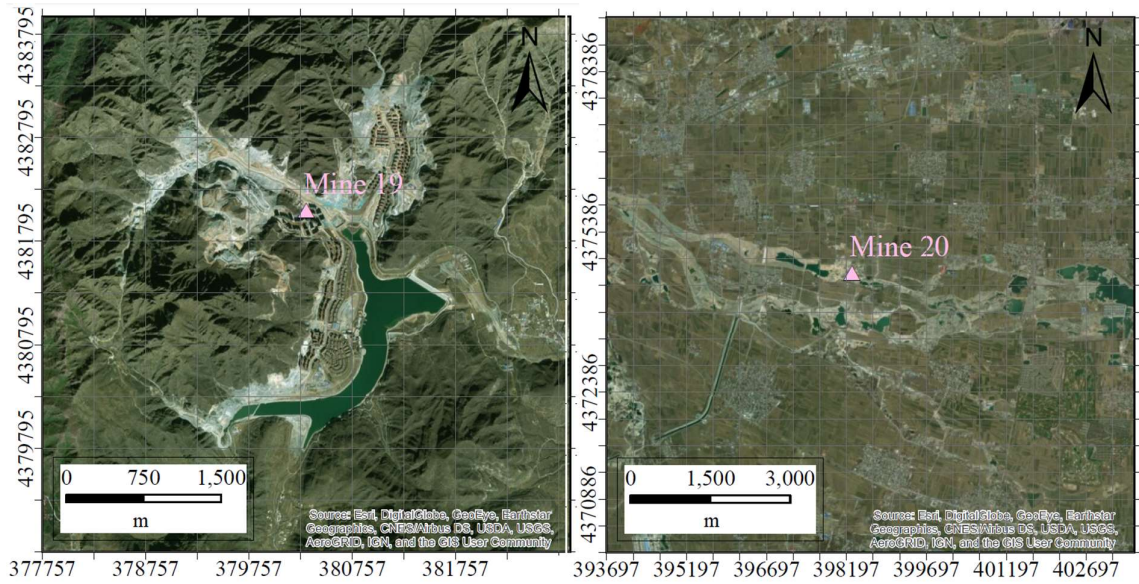


Figure 3.5. Mine 19 and 20. Self-produced data. Source: Esri, Digital Globe, GeoEye, Earthstar Geographics, CNES/Airbus DS, USDA, USGS, AeroGRID, IGN, and the GIS user community.

After an initial introduction to the main open-pit mines in the region surrounding Beijing, the next section of this chapter will focus on the mine object of study of this work of thesis.

3.2 | The mine under study

Firstly, the geographic and territorial framing of the open-pit mine under study is reported in the next figure 3.6 where, in addition, some photographs of the main parts are shown.

As introduced in the first chapter, mining quarries (and especially open-pit mines) causes deep soil modification. They are often visible by observing common online Map Visualization Services as Google Earth[®] or Bing Maps[®] (please note, for example, the difference between image (2) and image (3) of the figure 3.6). They can causes, in some serious event, environmental damage as pollution or strong surface erosion during atmospheric agents.

In particular, this mine is located northeast of China's capital but for reasons of privacy, it was not possible to indicate the exact coordinates of the mine.

Furthermore, the mine is part of a large extraction zone where coal and iron are mainly extracted. The mine, opened in 1959, is owned by one of the largest state-owned enterprise based in Beijing. Moreover, it is organized as multiple-steps mine with an extending area of about 17 km² and reserving more than 140 tonnes of iron ore (Chen et al., 2015). The immense main body of the aperture (please refer to images (2), (5) and (6) of the figure 3.6), big over 600 m of length and with a depth of about 40 m, causes a profound modification of the Earth's surface, which is why it will be widely analysed in this work.

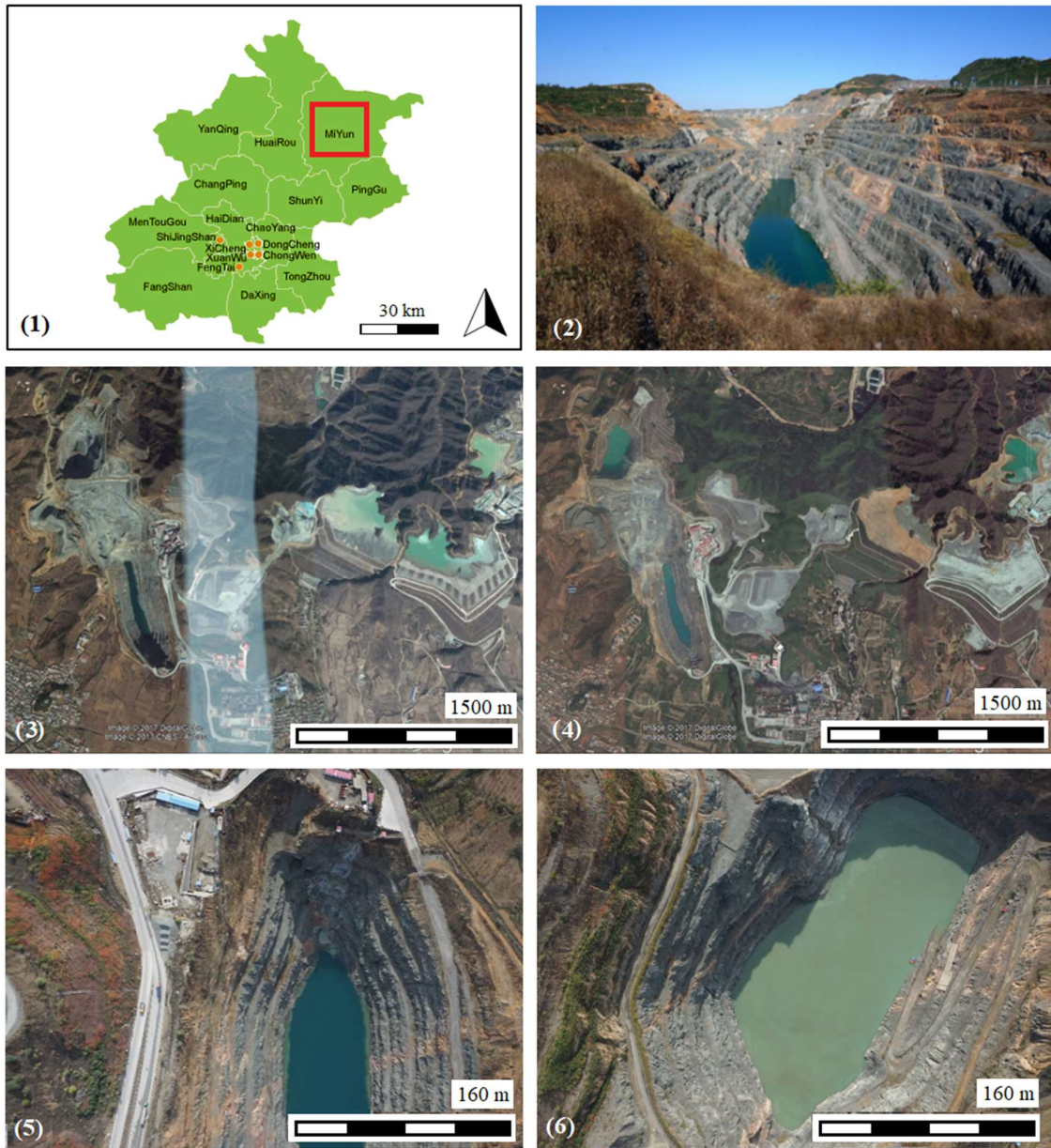


Figure 3.6. Geographical framing of the mine in Beijing area (1). The main body of the open-pit mine (2) (Source: Chen et al., 2015). Aerial view of December 2014 (3) and November 2016 (4) from Google Earth© and with two details (5) - (6).

3.3 | UAV field surveys

Due to the large size of the study area and the high resolution data needed, the SfM technique was applied using UAV technology. For a geomorphologic analysis aimed at highlighting changes in the surface of the open-pit mine, two different monitoring flights were carried out: one in August 2014 and one in October 2016.

The UAV used for the two surveys, a fixed-wing model, is called "Skywalker X5". It has a single propeller motor (mounted at the back), a wingspan of 980 mm and a length of 550 mm. With a top speed of over 40 km/h and a flight altitude of over 200 m, this drone is able to fly for over 40 minutes carrying a high-resolution camera (skywalkermodel.com). The drone was also equipped with the 20.9 MP resolution camera "Sony QX100", armed with a Carl Zeiss 10.4–37.1 mm lens and a 1.0" Exmor R CMOS sensor (Chen et al., 2015). The drone is illustrated in the next figure 3.7, taken by the official online store.



Figure 3.7. The Skywalker X5, or the UAV used during the two surveys. Source: skywalkermdel.com.

Flights were entirely planned using a PC in the field using MissionPlanner® and setting a flight altitude between 250 m and 350 m above ground, in order to have a minimum overlap of 80% for a single stripe and at least 40% between stripes.

As is possible to observe on the maps in figure 3.8, through a blue line is represented the route followed by the UAV during the survey of 2014. Similarly, in the following figure 3.9, the red line represents the route followed by the UAV during the 2016 survey.

As it may be observed comparing the two maps, in 2016 the drone flew covering a larger area and with a smaller distance between the stripes. This aspect will be examined in more detail in the following chapters.

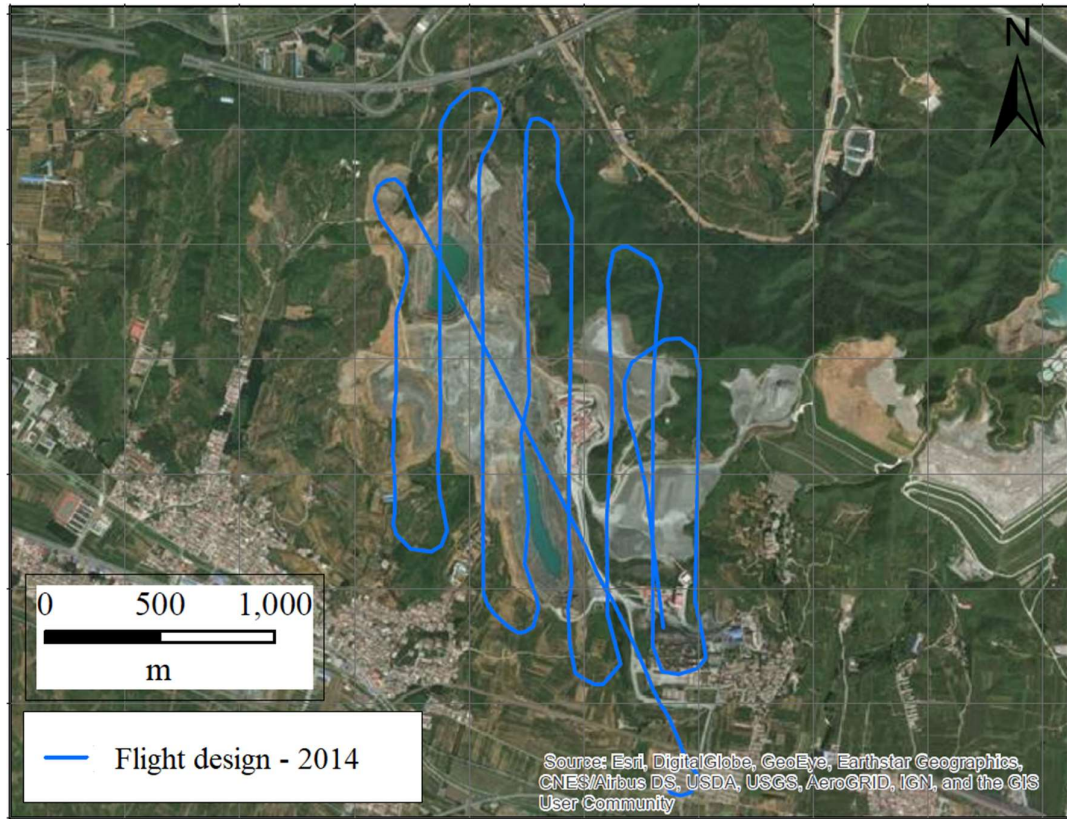


Figure 3.8. Flight design of 2014 survey.

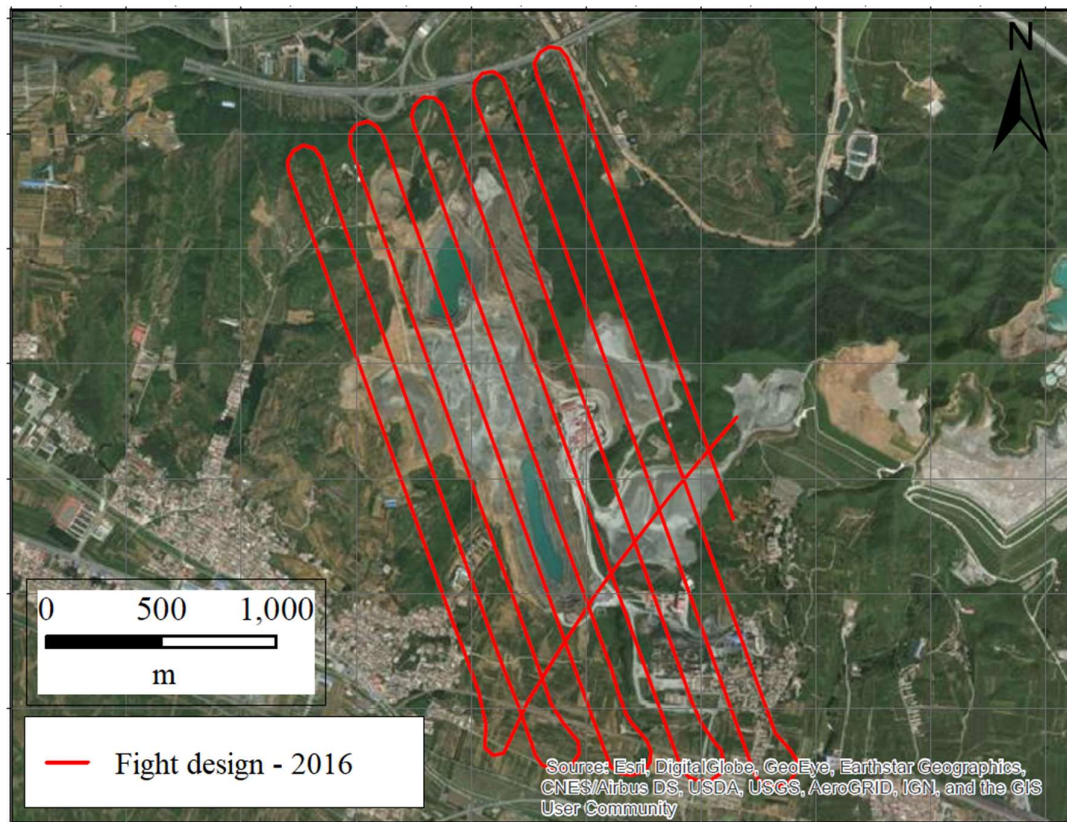


Figure 3.9. Flight design of 2016 survey.

The following two maps, in particular in figure 3.10 and in figure 3.11, represent the position of the GCPs inside the mine. The blue triangles represent the GCPs used for the 2014 survey, while the red triangles represent the GCPs used in 2016. In addition, in the next figure 3.12, are proposed some images taken by drone during the survey and that show the position of GCPs on the ground within the study area.

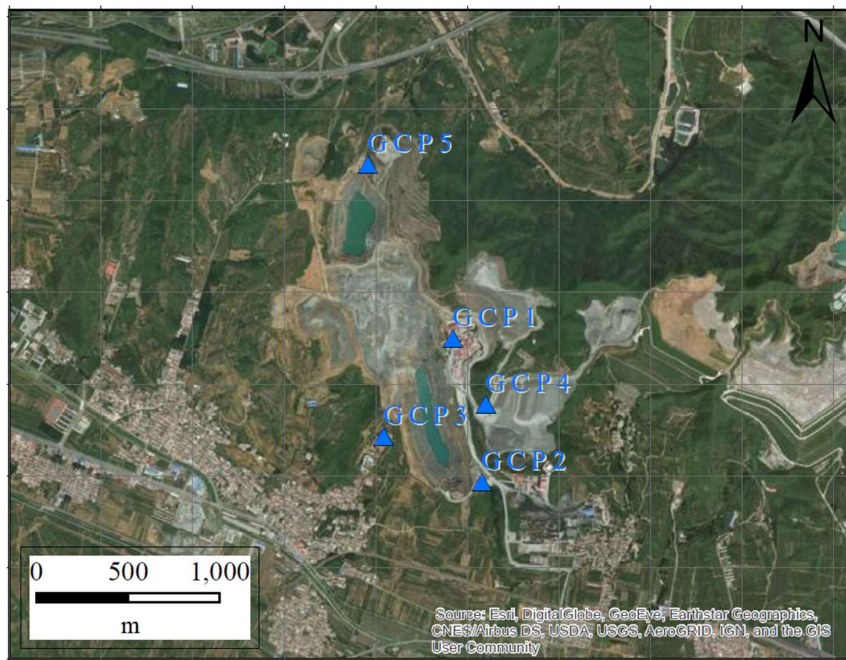


Figure 3.10. Ground Control Points used in 2014.

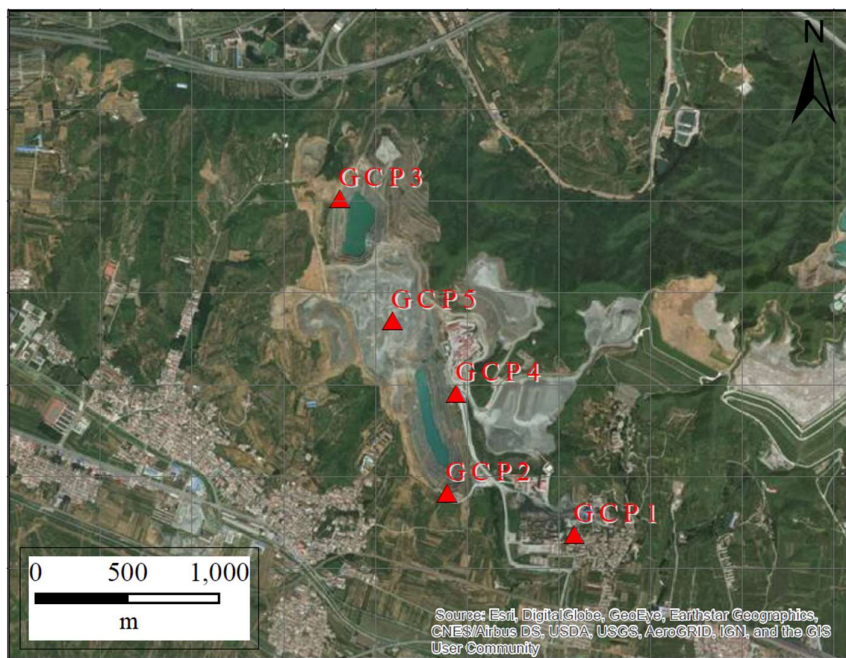


Figure 3.11. Ground Control Points used in 2014.



Figure 3.12. The location of GCPs on the ground within the study area.

The materials and methods used for this thesis will be introduced. In particular, initially a description will be made for a generic drone that can be used for a photogrammetric survey. Subsequently, the geomorphological analyses carried out will be presented.

4.1 | UAV set up and flight plan

4.1.1 | UAV general settings

An example of UAV that can be used for a high-resolution photogrammetric survey will be presented in detail here. In fact, the main characteristics of a widely-used drone for topographical surveys “MyTwinDream FVP” will be shown with the kind permission of China University of Geosciences of Beijing (CUGB).

In general, when working with drones at a professional level, is important to note that one of the most imperative parameter for UAV surveying is its battery capacity (as well as its weight) as a limiting factor for the flight duration (for example, the Skywalker X5 used for this work has a four-cell 3500mha Li-Ion polimer batteries). In accordance with this, the central body is very frequent made of extremely lightweight material (EPO foam and carbon fibre) to reduce the overall weight of the aircraft and save on energy consumption.

The following table 4.1 shows the main construction parameters of the illustrative drone.

Table 4.1. The main technical characteristics of UAV used for such work.

| Parameters | |
|--|------------------------------|
| <i>Number of engines</i> | 2 |
| <i>Type of propulsion</i> | Blades |
| <i>Left engine rotation</i> | Clockwise |
| <i>Right engine rotation</i> | Counter clockwise |
| <i>Wingspan</i> | 1.8 m |
| <i>Fuselage length</i> | 1.23 m |
| <i>Body height</i> | 0.35 m |
| <i>Maximum flight time</i> | 2 h |
| <i>Empty weight (without camera)</i> | 0.960 kg |
| <i>Maximum takeoff weight</i> | 5.8 kg |
| <i>Maximum surveying area</i> | > 10 km ² |
| <i>Takeoff type</i> | Semiautomatic |
| <i>Type of battery</i> | High Discharge Li-po Battery |
| <i>Battery voltage</i> | 22.2 V |
| <i>Electrical battery capacity</i> | 10,000 mA/h |
| <i>Battery weight</i> | 1.40 kg |
| <i>Full speed</i> | 30 m/s |
| <i>Cruise speed</i> | 2.8 m/s |
| <i>Body building material</i> | EPO foam |
| <i>Inner bar construction material</i> | Carbon fibre |

Following figures, 4.1 and 4.2, represent the UAV electrical scheme with photographs of the main components, taken with kind permission of China University of Geosciences of Beijing - CUGB.

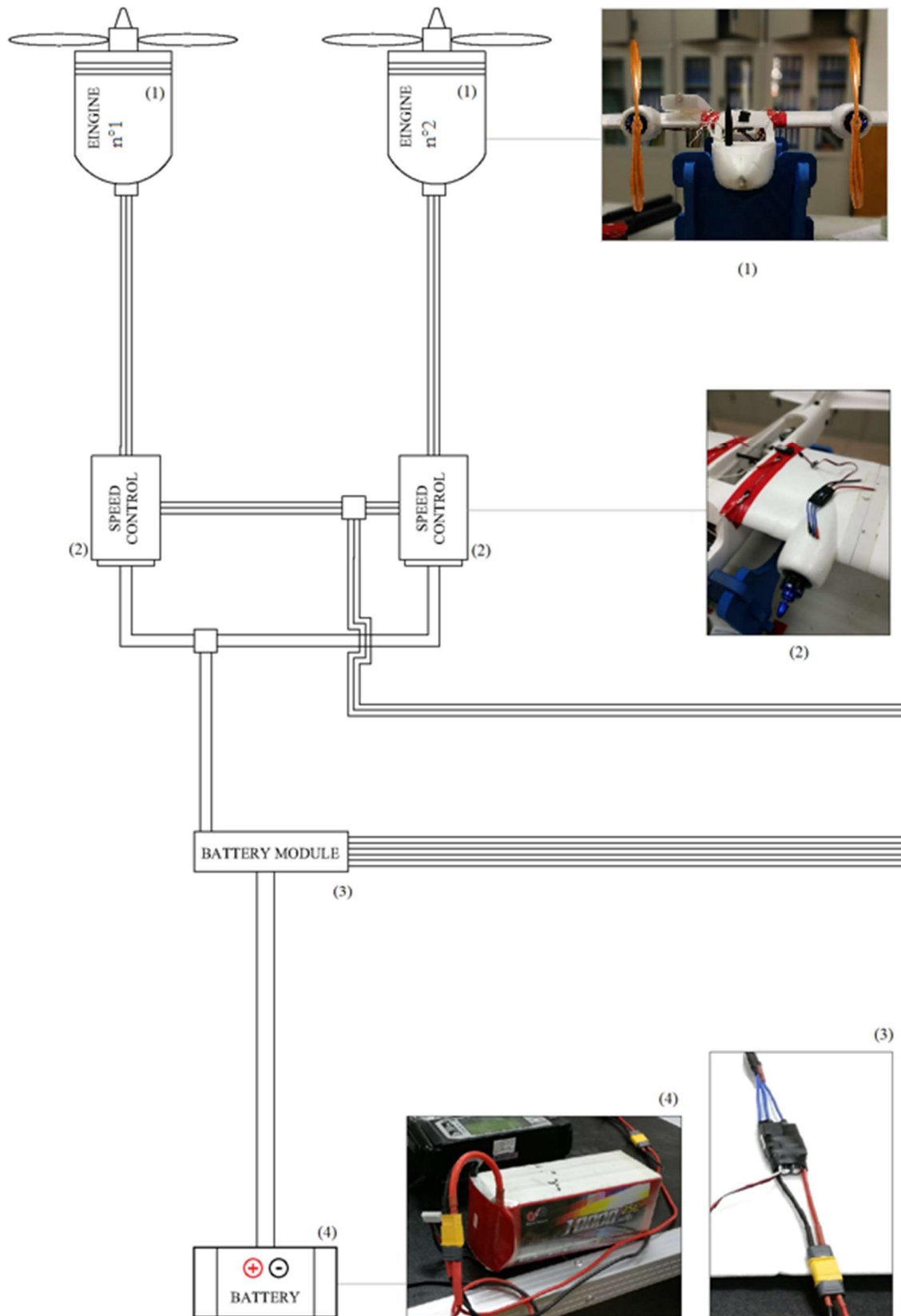


Figure 4.1. Electrical scheme: Engines (1); Speed Controls (2); Battery module (3); Battery (4). Powered by DraftSight 2017©.

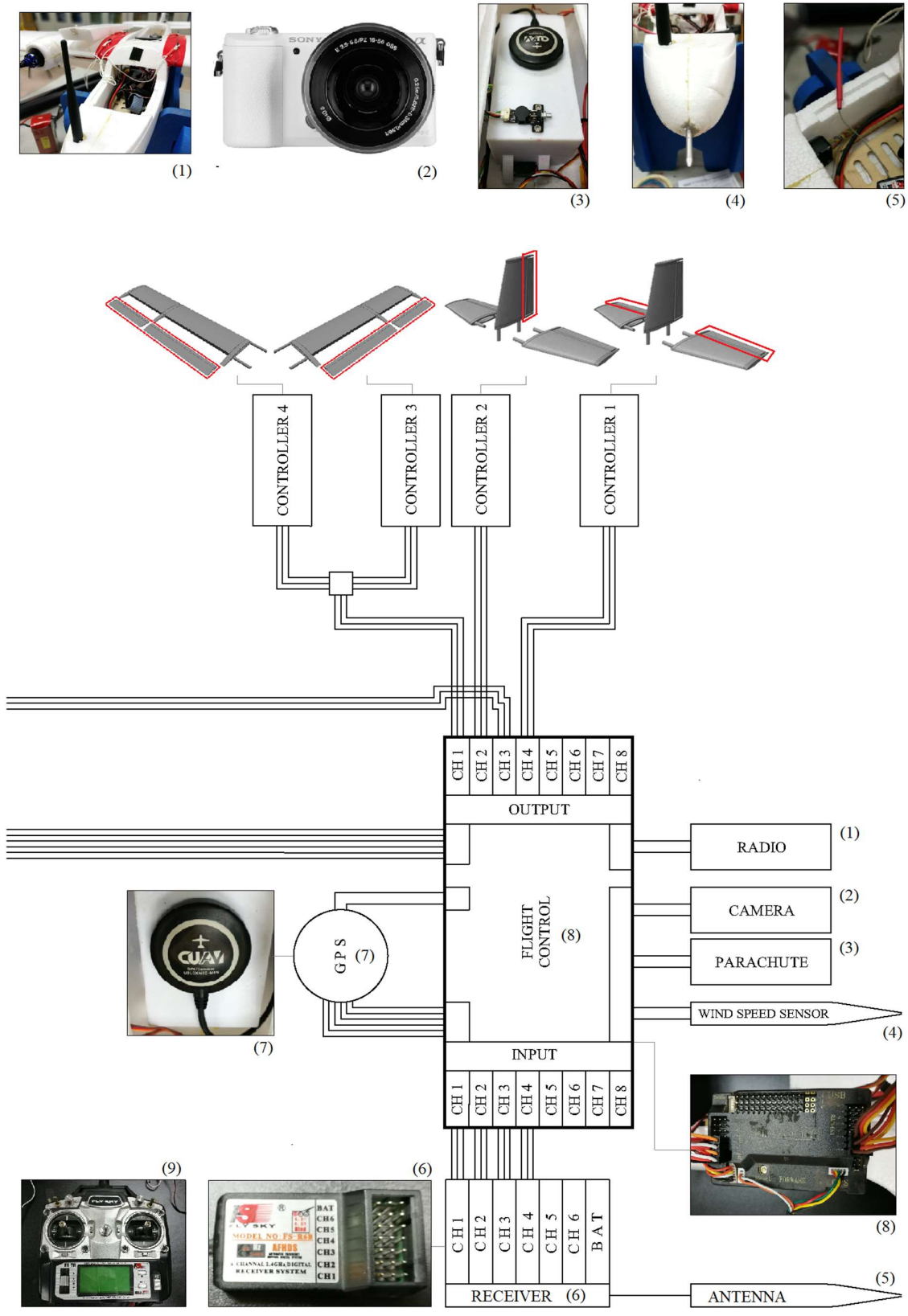


Figure 4.2. Electrical scheme: Radio (1); Camera (2); Parachute (3); Wind speed sensor (4); Antenna of receiver (5); Receiver body (6); GPS receiver (7). Powered by DraftSight 2017©.

Below, are mentioned some of the key characteristics of a generic UAV components:

- i. The *propeller engine* works with a screw principle, and is able to convert a rotating motion into a propulsion force (Glauert, 1935). It consists of a central hub rotating around a longitudinal axis where two wooden blades are attached with an angle of 180°. The two motors, placed on the two wings, rotate with opposite direction of rotation.
- ii. The *Speed Control* is a component of the electronic circuit that is designed to vary the propeller speed by increasing or decreasing engine speed. It is used for piloting the aircraft to handle speed and can be used to brake the drone aerodynamically.
- iii. The *Battery module* is a smallest energy storage consisting of one cell or an assembly of cells, electrically connected in serial or in parallel, placed in one container and mechanically associated. It is used for proper battery power management to Speed Controls and Flight Control.
- iv. The *Battery* is an electrical device consisting of different electrochemical cells with external connections and it is used for providing power to other electrical devices. Different types of batteries can be installed on the UAV: usually, and for the same technology, increasing the capacity increases both weight and durability.
- v. The *Radio* is an electronic device that allows UAV remote control via computer located on the ground. Specifically, it allows communication between the aircraft and the self-pilot software installed on the PC.
- vi. The *Camera*, located down in the fuselage (provided with a dedicated hole for the lens), is certainly one of the most important elements mounted on the UAV, as its features define a success of the survey. For example, high resolution of the camera allow a higher resolution of the 3D result (with the same altitude and operating speed).

The following table 4.2 shows the characteristics of the camera mounted on the Skywalker X5 UAV used for the two flights of this work.

Table 4.2. The main parameters of the camera mounted on the Skywalker X5 used for the two flights.

| | 2014 - 2016 |
|---------------------------------------|--------------------|
| <i>Camera producer</i> | SONY |
| <i>Camera model</i> | QX100 |
| <i>Resolution</i> | 20.9 MP |
| <i>Focal length (Carl Zeiss lens)</i> | 10.4 – 37.1 mm |
| <i>Sensor (ExmorR CMOS)</i> | 1” |

- vii. The *Parachute* is an aerodynamic decelerator that acts on a free-fall-body in the atmosphere (UAV), providing equal and opposite acceleration to the gravitational force, thus slowing down its downward movement to the ground. It consists of synthetic fabric and cord and is used to safely land the drone.
- viii. The *Wind speed sensor* is an electronic device positioned on the bow of the plane with the purpose of measuring wind speed. It is used as a remote pilot support to measure wind parameters.
- ix. The *Antenna* is the electronic device with the purpose of receiving the signal coming from the radio remote control, which is indispensable for manual driving.
- x. The *Receiver* is a basic electronic component for UAV flight, and works from connector between antenna and Flight Control.
- xi. The *Flight Control* is probably the main part of the UAV electrical system because it manages the different components of the aircraft to allow the flight. At the input channels are connected the various channels from the Receiver (which, thanks to the antenna, receives inputs from radio remote control positioned in the hands of the operator) and at the output channels the Flaps on the wings, the Rudder and the Elevators for determining the UAV movements in the atmosphere. The following figure 4.3 shows the main structural components of a hypothetical aircraft with the movements (Yaw, Pitch, and Roll) that they control. Flight Control is more connected to other aircraft components such as radio, camera, parachute, wind speed sensor, and GPS signal receiver.

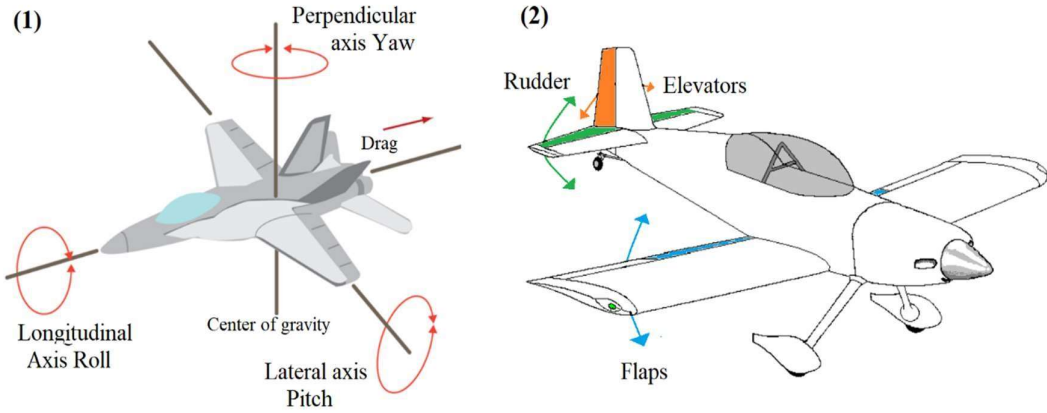


Figure 4.3. The three main movements of an airplane (1) and the components that allow them (1). Source: www.machinedesign.com and www.vincesrocket.com.

- xii. The *GPS Receiver* is an electronic device capable of receiving information about its position (via geographic coordinates) using the Global Positioning System (Rocken et al., 1993). Through a dedicated network of artificial satellites in orbit, it allows localization by transmitting a radio signal from each satellite and processing signals received by the receiver.
- xiii. The *Radio Remote Control* is a device used to remote control an equipment using radio waves as a transmission medium. The output signal from it is captured by the antenna placed on the receiver placed on the aircraft and allows the flight in manual mode. Following, in figure 4.4, there is a scheme about the main commands.

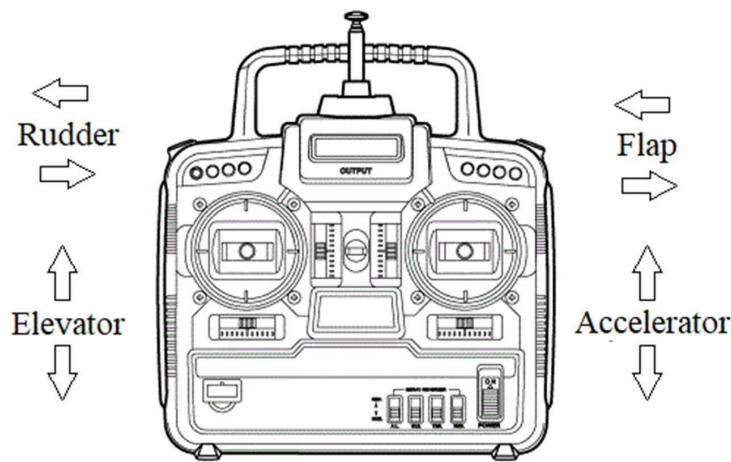


Figure 4.4. The main commands of a radio remote control. Source: ww.baronerosso.it.

4.1.2 | UAV flight planning

The two flights of this work, performed by Skywalker X5, were planned using the MissionPlanner[®] software with which is possible to identify the area of interest from a preloaded map. Specifically, by entering UAV flight parameters, the software allows to display the route during flight and determine the number of photographs to take for good performance.

The georeferencing of the photographs was done using a DGPS real-time geolocation device RTK (Real Time Kinematic), which provides to build a .csv file describing the taking position (x,y,z) of each single photo in WGS84 Coordinate System (EPSG 4326). For a better quality result, GCPs (known coordinate points) were inserted within the study area.

Below are the three settings that the software allows to manage.

1. *Simple settings*. In this windows is possible to:
 - i. Choose the Camera in a set of different models or insert a new one manually. In the first case, the advanced settings are pre-configured.
 - ii. Set the altitude and speed of the UAV during the survey. These parameters are fundamental and depend upon different factors. Firstly, by the topography of the area and by the type of result that we are looking for. In fact, high survey altitude allow a bigger survey area but, consequently, a lower resolution in the result. Usually is set from 200 m to 1000 m (in very difficult area, i.e. high hills). Software automatically calculates the UAV direction as Angle [deg].
 - iii. Other sets are for displaying the information into the map and for specifying the position of the base (takeoff and landing point).
2. *Grid option*. In this window:
 - i. Software automatically calculates the distance between lines [m] but is most important to set the percentage of overlap (almost 80%) and sidelap (almost 60%) of photos for obtaining a good quality result.
3. *Camera config*. In this window is possible to set different parameters of camera:
 - i. Focal Length [mm], Sensor Width [pixel], Image Width and Height [pixel]. Height [mm] are automatically calculated by software in function of the Focal Length (these parameters are pre-configured for cameras in the simple setting list).

Finally, the software offers a set of statistical values regarding planned flight, for example:

- i. Area [m²], Distance [m], Elevation [m] and Time [min] of the survey.
- ii. Distance [m] and Time [sec] between images and Ground resolution [cm].
- iii. Number of strips with their distance [m] and curve diameter [m].

The main flight parameters used for the two surveys of this work are summarized in the following table 4.3:

Table 4.3. UAV Flights parameters.

| <i>UAV campaign</i> | <i>Relative Flight Height [m]</i> | <i>Number of Pictues</i> | <i>Photo Interval [m]</i> | <i>Number of stripes</i> | <i>Stripes Interval [m]</i> | <i>Overlap Single Stripe [%]</i> | <i>Overlap Between Stripes [%]</i> |
|---------------------|-----------------------------------|--------------------------|---------------------------|--------------------------|-----------------------------|----------------------------------|------------------------------------|
| <i>Aug. 2014</i> | 291 | 437 | 40 | 8 | 190 | 81 | 40 |
| <i>Oct. 2016</i> | 353 | 657 | 40 | 10 | 150 | 80 | 52 |

4.2 | SfM photogrammetric survey

Each photo taken by UAV is described by georeferencing parameters (latitude, longitude and altitude) and airborne position (Yaw, Pitch and Roll) parameters. These data, directly calculated from the aircraft on-board devices, are importable as a text file in a 3D modelling software.

The images taken during this work were subsequently processed using Agisoft PhotoScan[®] software. So, once associate each image with the parameters described above, the software can build a cloud of points (x,y,z) using the overlapping of the images. Greater is the percentage value of the overlap and better will be the accuracy of the model. Software also allows inserting GCPs for better accuracy of the three-dimensional model. GPS point coordinates were imported into a specific form of the software using a text file, and then, points were manually added to the map by pointing to the targets in each photo they were visible. Next figure 4.5 shows the information about camera locations and quality of the survey in function of the overlap between pictures.

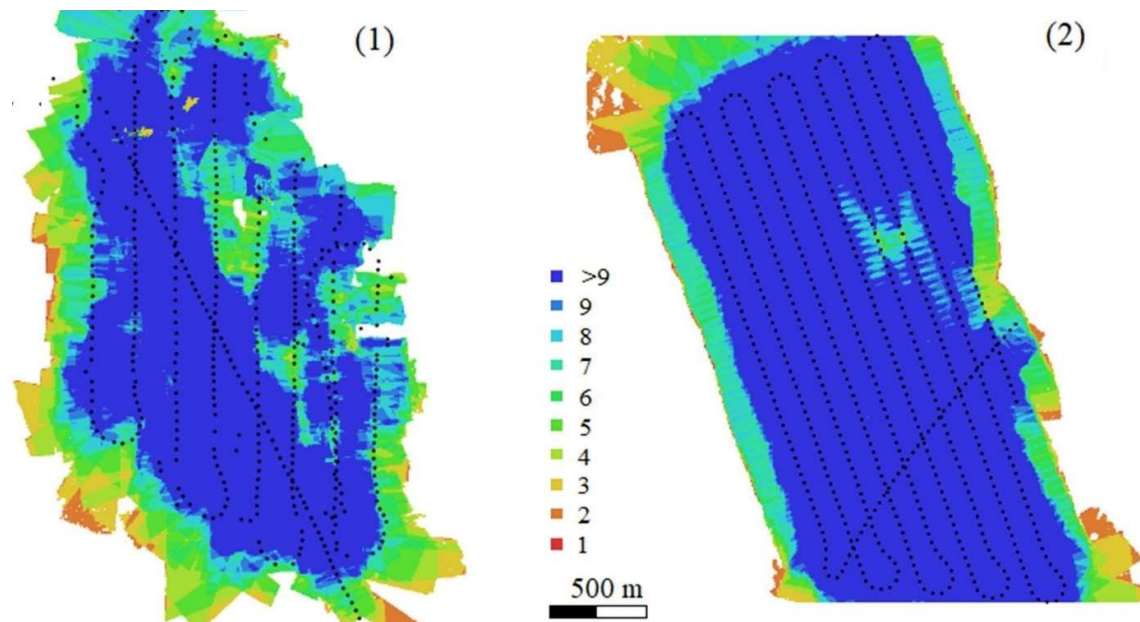


Figure 4.5. Camera location and overlap of 2014 (1) and 2016 (2). Source: Agisoft PhotoScan[®] Report.

Below, in figure 4.6, is possible to appreciate a Photoscan[®] screenshot taken during photographs processing that show the list of photos and the GCP parameters. On the left there are the information about pictures (GPS position of the UAV and inertial position of the camera with calculated errors) and GCPs (their GPS position on the ground).

For reasons of privacy, it was not possible to indicate the coordinates of the mine. Otherwise, on the right, there are the 3D sparse point cloud model (with the positions of GCPs) and some pictures preview.

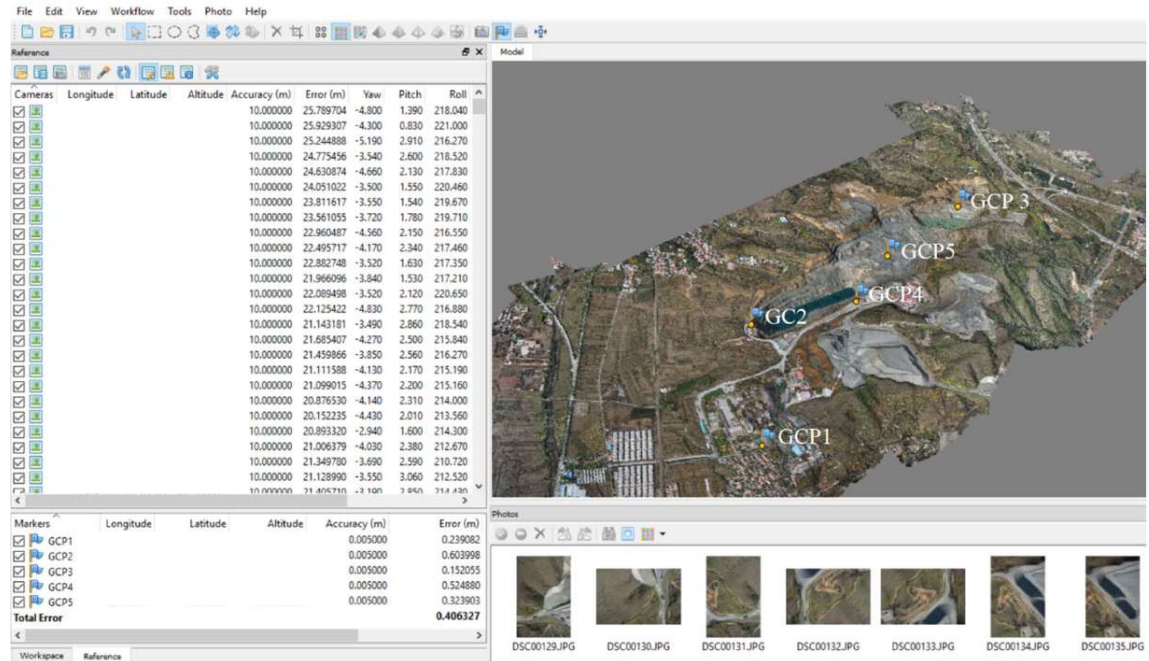


Figure 4.6. Example of software screenshot during 2016 data process.

The accuracy of the model obtained by the software is estimated through error calculation. In particular, PhotoScan[®]'s report provides automatic calculation of the error related to survey data, camera position and relative to the Ground Control Points. The error types are described below (as well as reported in PhotoScan[®] User Manual), while relative values are shown in the results chapter.

1. Survey Data:

- i. Reprojection error = root mean square reprojection error averaged over all tie points on all images.

2. Camera Locations

- i. X error (m) = root mean square error for X coordinate for all the cameras.
- ii. Y error (m) = root mean square error for Y coordinate for all the cameras.
- iii. XY error (m) = root mean square error for X and Y coordinates for all the cameras.
- iv. Z error (m) = root mean square error for Z coordinate for all the cameras.

- v. Total error (m) = root mean square error for X, Y, Z coordinates for all the cameras (please refer to next equation. Total error is calculate as ‘root-mean-square deviation’) (RMSD), or the measure of the differences between values predicted by the software and the input coordinate values. The RMSD represents the ‘sample standard deviation of the differences’ between predicted values and input values, as in equation (1) (Agisoft PhotoScan® official guide).

$$Total\ Error = sqrt\left(\frac{\sum_{i=1}^n [(X_{i,est} - X_{i,in})^2 + (Y_{i,est} - Y_{i,in})^2 + (Z_{i,est} - Z_{i,in})^2]}{n}\right) \quad (1)$$

$X_{i,in}$ = input value for X coordinate for i camera position;

$X_{i,est}$ = estimated value for X coordinate for i camera position;

$Y_{i,in}$ = input value for Y coordinate for i camera position;

$Y_{i,est}$ = estimated value for Y coordinate for i camera position;

$Z_{i,in}$ = input value for Z coordinate for i camera position;

$Z_{i,est}$ = estimated value for Z coordinate for i camera position;

3. Ground Control Points

- i. XY error (m) = root mean square error for X and Y coordinates for a GCP location / check point.
- ii. Z error (m) = error for Z coordinate for a GCP location / check point.
- iii. Error (m) = root mean square error for X, Y, Z coordinates for a GCP location / check point.
- iv. Projections = number of projections for a GCP location / check point over all the images.
- v. Error (pix) = root mean square error for X, Y coordinates on an image for a GCP location / check point averaged over all the images.
- vi. Total = implies averaging over all the GCP locations / check points.

The PhotoScan® software, after an initial operation of photographs aligning, offers a first cloud of point, called ‘sparse cloud point’. Subsequently, through the ‘build dense point tool’ it is possible to increase the number of points of the cloud in order to obtain a much higher resolution result. This cloud is called ‘dense cloud point’. In addition, the software allows the construction and subsequent export of the Digital Elevation Model (DEM) and the Digital Orthomosaic Model (DOM) of the area surveyed.

This work was carried out for the 2014 and 2016 survey and the dense point clouds were then exported in .las format and imported into CloudCompare® software for the analysis, free downloadable at www.danielgm.net. Next figure 4.7 shows an operative example screenshot during data management.

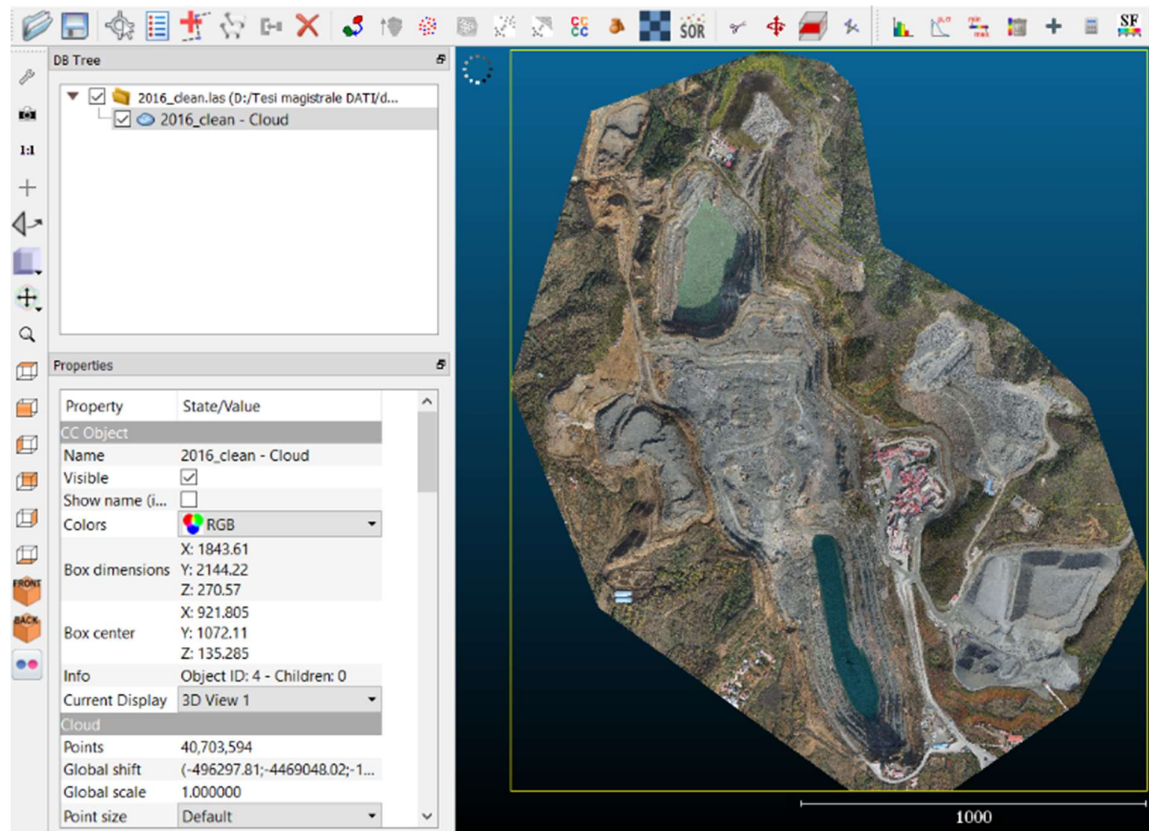


Figure 4.7. CloudCompare screenshot during 2016 cloud analysis.

Using CloudCompare®, the point clouds were initially aligned using five reference points and the ICP algorithm, so that they can be compared by becoming overlapping. The three alignment tools used for this operation were ‘match bounding-box centres’, ‘fine registration’ and ‘align’. Subsequently, the clouds were trimmed for removing any points not belonging to the mine’s surface.

The latest step was to clean the cloud by statistically eliminating points through the ‘noise filter’. Once the clouds cleaning operation was completed, they were re-exported and imported into Esri ArcGis® software for building and analysing DSMs.

4.3 | DEM analysis

In this chapter will be introduced the techniques and methodologies used for the analysis of DEMs (2014 and 2016) obtained by photogrammetric survey from drone. In particular, in this thesis work, the main focus was on the calculation and mapping of the main geomorphological analyses of the Earth's surface, i. e. Elevation, Slope, Aspect, Curvature and Roughness.

These analyses were carried out separately first on the DEM obtained from the 2014 survey and then on the DEM obtained from the 2016 survey. The results of these operations will be included in the results chapter and mapped across the entire study area. In some cases, for better viewing and to offer more interesting data to the user, a specific area within the quarry will be focused on.

The main characteristics of the geomorphological analyses carried out in this thesis work are then described.

- i. *Elevation Analysis*. This analysis involves the creation of a thematic map as a function of the elevation of the single cell of the raster, usually applying a colour scale from lower to higher values. In this way, the difference in height is clearly visible.
- ii. *Slope Analysis*. In this thesis work, this analysis was carried out on the 2014 and 2016 DEMs using the 'Slope' tool in Landserf[®] software, free downloadable from <http://www.landserf.org/>. It calculates, for each cell, the maximum rate of change in value from a cell to its neighbors and it fits a plane to the z-values of a 7x7 cells neighborhood around the processing cell. The maximum change in elevation over the distance between the cell and its eight neighbors identifies the steepest downhill descent from the cell. Next equation (2) shows how that tool works.

$$Slope_{degrees} = ATAN \left(\sqrt{\left(\frac{dz}{dx}\right)^2 + \left(\frac{dy}{dx}\right)^2} \right) \cdot \frac{180}{\pi} \quad (2)$$

- iii. *Aspect Analysis*. As is possible to observe in the Esri ArcGis[®] manual, Aspect analysis identifies the downslope direction of the maximum rate of change in value from each cell to its neighbors, very similar to the slope direction. The values of each cell in the output raster indicate the compass direction that the surface faces at that location. It is measured clockwise in degrees from 0 to 360 and indicates the cardinals points. Flat areas having no downslope direction are given a value of -1. Next figure 4.8 show an example scheme.

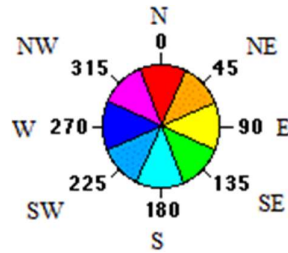


Figure 4.8. Example scheme about how to work the aspect tool. Source: modified by ArcGis Help.

- iv. *Curvature*. Another interesting analysis that can be carried out on a DTM is the curvature, useful for a better identification of the geomorphological forms present on the surface. In a mathematic way, the curvature is the second spatial derivative of the elevation of the terrain. The calculation of the curvature is of primary importance, for example, for studying the surface runoff and for identifying features related to erosion process.

In this thesis the software Landsert[®] was used, and the curvature has been calculated using the Evans method, as proposed by Tarolli et al., 2012. In particular, Evans proposed a DTM where the surface is approximated using a five-terrain-parameters bivariate function Z , with two variables (x and y), as described in the following equation (3) (Evans et al., 1979):

$$Z = ax^2 + by^2 + cxy + dx + ey + f \quad (3)$$

In the equation, x , y and Z are the local coordinates and a to f are quadratic coefficients. These coefficients could be solve within a moving-window of 3x3 cells and therefore using a combination of neighbouring cells. As authors continue, two of the most widely used methods of calculating curvature are Profile Curvature and Plan Curvature.

The Profile curvature is the curvature of the surface in the steeper downslope direction. It describes the rate of change of slope along a profile. For this reason, this tool could be used to highlight convex and concave slopes within the DTM.

On the other hands, Plan curvature is the curvature of a contour drawn through the central pixel. For this reasons, it describes the rate of change of aspect in plan across the surface and may be useful to define ridges, valleys, and slopes along the side of these features.

- v. *Roughness*. The soil surface microtopography, or roughness, was moreover calculated for this thesis work from the two DEMs input. In particular, the two main roughness indices are (Cavalli et al., 2008):

1. *Roughness index-elevation*. This index corresponds to the standard deviation of the 'residual topography', calculated as follows:
 - i. From the input DEM raster, a new grid is calculated using the Focal Statistic tool in ArcGis®, set up to calculate the mean value in a moving window of 7x7 cells. The single cell of this new grid has, as its value, the mean value of the neighbouring cells of the starting raster. It is possible to call this result “mean DEM”.
 - ii. In a second phase, using the raster calculator, the difference between the input DEM and the ‘Mean DEM’ was calculated.
 - iii. Using the Focal Statistic tool on the residual topography grid on a moving window of 7x7 cells and set up to calculate the Standard Deviation, a new raster was calculated - please refer to equation (4). Each cell of it has a value equal to the Standard Deviation calculated in relation to the neighbouring cells. This new raster can be assumed as surface roughness.

$$\sigma = \sqrt{\frac{\sum_{i=1}^{25} (x_i - x_m)^2}{N}} \quad (4)$$

Where N is the number of neighbouring cells, x_i is the value of the specific cell and x_m is the mean value of the N cells.

2. *Roughness index-slope*. This index analyses the topographic variability starting from the maximum slope grid, and calculating its Standard Deviation as follows:
 - i. Based on the slope raster, a new grid is calculated using the Focal Statistic tool set up to calculate the Standard Deviation of a 7x7 cells window. This new raster can be defined as the roughness of the surface.

4.4 | DoD for volume quantification

In recent decades, thanks to the development of technologies capable of producing high-resolution digital terrain models (DEMs), it has been possible to plan campaigns for surveying the Earth's surface in order to understand its evolution (Lane et al., 2010). In particular, the SfM technique directly from drone can offer an excellent starting point for the collection of spatial data, which will then be analysed for the construction of the DEMs.

The programming of flights above the study-area (at scheduled intervals) makes possible to construct several digital models of the surface (raster files) that are then compared using the DEMs of Difference (DoD) method. In particular, they are produced by analysing the differences in elevation between an earlier and a later DEM. Once the difference value has been calculated and the surface of the raster cell is known, this methodology allows:

- i. A qualitative volume analysis, i. e. the precise location of sub-areas subject to erosion or sedimentation inside the study-area.
- ii. A quantitative volume analysis, i. e. the quantification of the eroded and sedimented volume in the study-area;

As example, the following figure 4.9 shows the result of applying DoD obtained by comparing two DEMs before (z_1) and after (z_2) a forcing event within a watercourse (Williams, 2012).

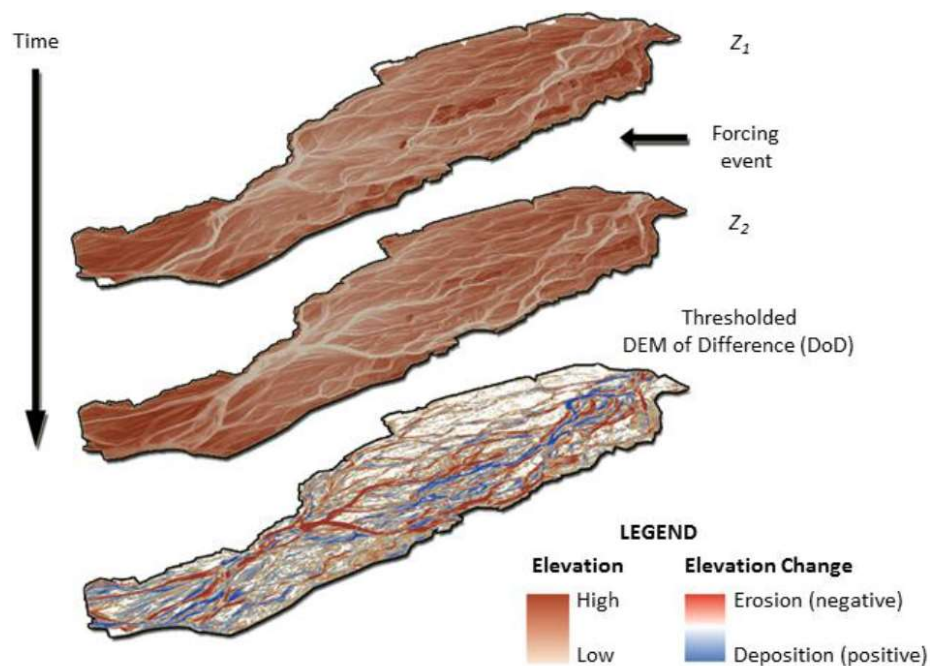


Figure 4.9. An operating scheme of DoD. Modified by Williams, 2012.

The simplest way to obtain a DoD describing the elevation variation between two multitemporal DEMs is to carry out simple subtraction, as well as by equation (5):

$$DoD_{21} = DEM_{t2} - DEM_{t1} \quad (5)$$

Where DEM_{t2} refers to a model obtained from a subsequent survey of DEM_{t1} . The result of this operation leads to a DoD that describes the simple elevation variation but without considering possible errors (due, for example, to the survey operations or the precision of the instruments used) (Wheaton et al., 2010).

The quality of the starting rasters is therefore a fundamental element of the whole analysis, also because the result is doubly conditioned by the error of the inputs.

A first method to consider the quality of DEMs in the analysis of geomorphological changes and thus improve the accuracy of the result is the definition of a threshold called ‘minimum Level of Detention’ ($_{\min}LoD$) which is propagated uniformly on the DoD (Brasington et al., 2003). The $_{\min}LoD$ threshold is chosen in such a way that the errors of the starting DEMs be propagated in the DoD error ($\delta_u DoD$) according to the following equation (6):

$$\delta u_{DoD} = \sqrt{(\delta z_{new})^2 + (\delta z_{old})^2} \quad (6)$$

Where δz_{new} and δz_{old} are the errors calculated respectively for the recent and for the oldest DEMs.

An alternative method for the estimation of $_{\min}LoD$ for DoD correction is based on statistical error theory (Taylor, 2012), in which a probabilistic threshold is chosen (U_{crit}) calculated from the user's accuracy necessities. The threshold proposed by Brasington et al is calculated as:

$$U_{crit} = t \left(\sqrt{(SDE_{new})^2 + (SDE_{old})^2} \right) \quad (7)$$

Where δz is regarded as an approximation of the standard deviation error (SDE) of each starting raster and t is the t-statistic value for the chosen confidence interval:

$$t = \frac{|z_{DEM_{new}} - z_{DEM_{old}}|}{\delta u_{DoD}} \quad (8)$$

Where $|z_{DEM_{new}} - z_{DEM_{old}}|$ is the DoD absolute value of each cell. The DoD can thus be calculated by excluding all quota changes with a lower probability than the set threshold.

Another method for the spatialization of vertical uncertainty proposed by Wheaton et al. (2010) is the use of a fuzzy logic-based methodology for the spatialization of uncertainty on the

individual cells of the DoD. In this way, by defining a system of rules, an uncertainty threshold δz cell by cell is detected.

In this thesis paper, the software used for DoD analysis (from DEM 2014 and 2016 of the areas inside the mine) was the Geomorphic Change Detection (GCD – version 6.1.14), briefly described in the following figure 4.10, and used as a tool by Esri ArcGis® 10.2.1.



Figure 4.10. Screen of GCD Software. Source: joewheaton.org.

5 | RESULTS AND DISCUSSION

In this chapter, the results obtained from the two surveys of the quarry under study will be presented and discussed. In particular, will be shown:

- i. the preliminary result of the surveys, i. e. the calculation of the x,y,z densified point clouds, obtained by processing the photographs taken by drone, the inertial positions of the aircraft and the coordinates of the ground control points;
- ii. The creation, analysis and the subsequent comparison of the two DSMs calculated after a preliminary cleaning and alignment of point clouds.

For reasons of privacy, it was not possible to indicate the coordinates of the mine.

5.1 | Results of the SfM applications

Figure 5.1 show a first result of the photogrammetric survey, in which it is possible to observe the two clouds of points orthogonal to the ground.

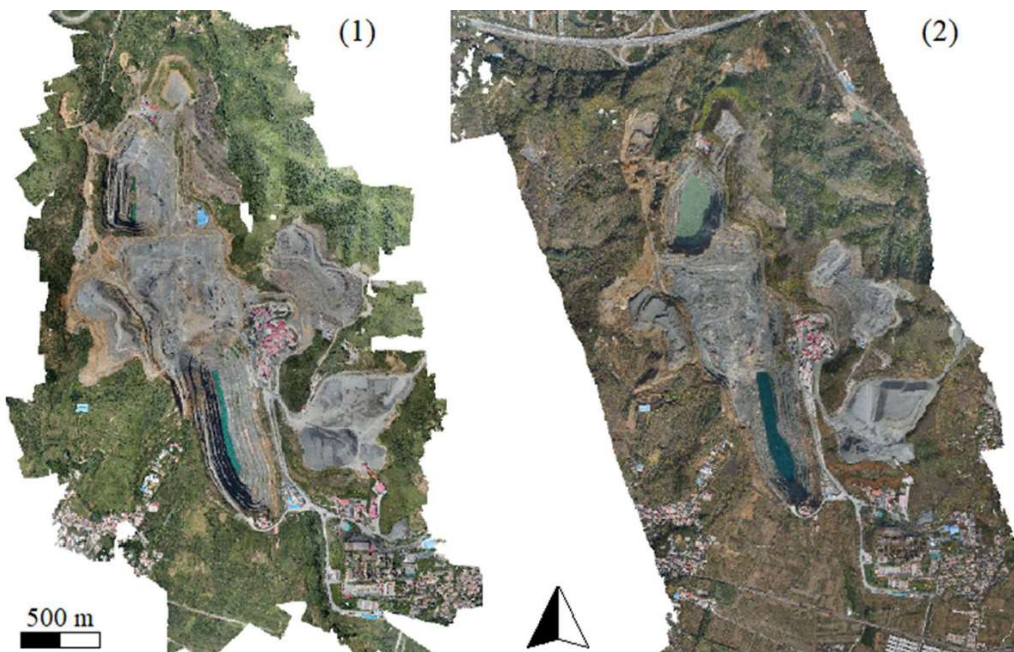


Figure 5.1. The first result of the 2014 survey (1) and 2016 (1). The detailed cartography will be shown later.

In addition, next tables shows a comparison between the data of survey 2014 and 2016 realized using the PhotoScan® report. In particular, table 5.1 shows a comparison between the main survey data and the table 9 shows the calculated error of camera location for building the clouds (please refer to chapter 4.2 for more information about errors).

Table 5.1. Comparison between main survey data.

| <i>Survey data</i> | <i>2014</i> | <i>2016</i> |
|-------------------------------|---------------------|---------------------|
| <i>Number of images</i> | 437 | 657 |
| <i>Flying altitude</i> | 291 m | 353 m |
| <i>Ground resolution</i> | 6.4 cm/pix | 8.09 cm/px |
| <i>Coverae area</i> | 4 sq km | 6.34 sq km |
| <i>Projections</i> | 1,437,784 | 2,210,535 |
| <i>Number of GCPs</i> | 5 | 5 |
| <i>Coordinate System</i> | WGS 84 (EPSG: 4326) | WGS 84 (EPSG: 4326) |
| <i>Number of spare points</i> | 393,826 | 392,304 |
| <i>Number of dense points</i> | 84,011,141 | 104,669,858 |
| <i>XY error</i> | 0.39 m | 0.38 m |
| <i>Z Error</i> | 1.13 m | 0.40 m |
| <i>Co-Registraion</i> | 0.52 m | |

As can be seen from the table, in 2016 it was chosen to fly at a higher altitude (353 m vs. 291 m). This leads on the one hand to an increase in the measured surface area (also due to a higher number of photographs), but on the other hand to a reduction in the ground resolution (8.08cm/px vs. 6.4cm/px). The process of densification of the sparse point cloud has been extremely laborious in both cases, but giving as a result tens of millions of points detected, an excellent starting point for subsequent analysis. The insertion of known coordinate points to the ground (GCP) has also greatly improved the accuracy of the point cloud, which is initialized by simply aligning the images. The theoretical explanation of the error calculation is reported in chapter 4.2.

It is very important to note that the error of point clouds can be drastically reduced by increasing the number of GCPs (for example > 15 rather than 5) and maximizing the performance of the PhotoScan® software. The latter, in fact, allows to set the quality of the images alignment and also to manually insert the quality of the cloud reconstruction, based on a scale from Very-Low to Ultra-High. For reasons strictly due to hardware limitations, it was decided to set the pictures alignment in High class (but not Ultra) and the reconstruction parameter in Medium class, and therefore not to the maximum of the software potential (and thus of precision of the result).

5.2 | DEMs calculation and analysis

5.2.1 Introductory analysis

Starting from the two clouds elaborated using PhotoScan[®], digital models of the quarry under study were subsequently built for 2014 and 2016. They, in raster format, were the starting point for the elaborations reported in this chapter.

In addition to surface models, the digital orthometric models (DOMs) were exported for a better understanding any increase in the area of the quarry. In fact, first proposed result is the analysis of the spatial variation of the perimeter of the quarry and the correlated estimate of the surface occupied by it (next figure 5.2, WGS84 - UTM Zone 50N).

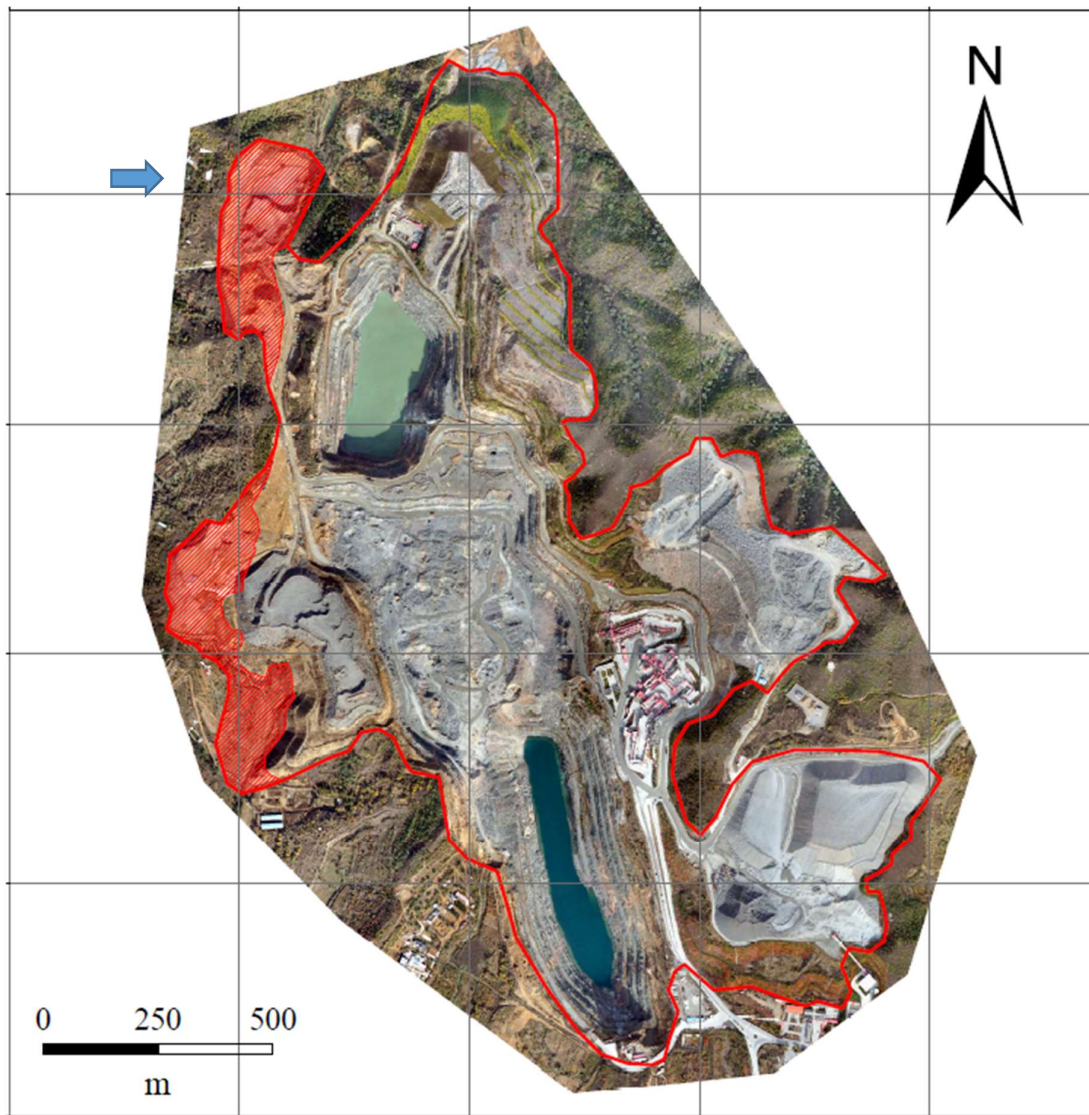


Figure 5.2. The red boundary line is the perimeter of the area occupied by the quarry in 2016, while the red-coloured part refers to the increase in the area of the excavation zone. The blue arrow shows the zone that will be zoomed in figure 5.3.

This introductory analysis aims to focus on the only variation in terms of the surface of the quarry, and not in terms of volume. As is possible to see in the figure 5.2, in the years the quarry has undergone an enlargement, especially in the western part. This result was obtained by comparing the two DOMs by incorporating the visibly mine zone into a polygon using Esri ArcGis®.

The following figure 5.3 shows a comparison between the orthophotos of 2014 and 2016. As is possible to see, the area belonging to the quarry has increased in terms of surface.

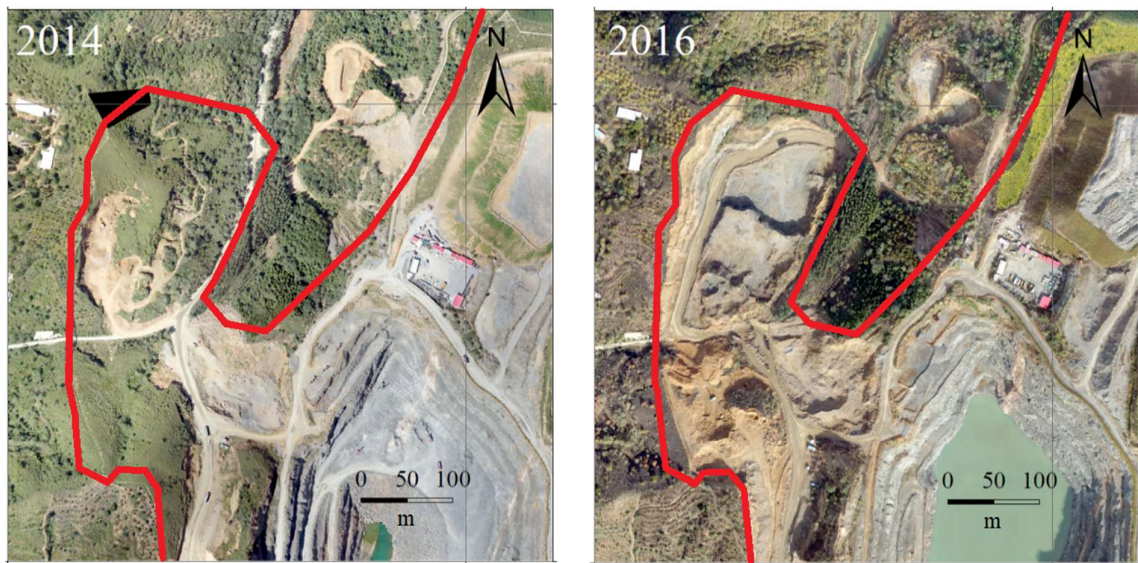


Figure 5.3. Particular example of increased surface area occupied by the quarry in the north-west.

Subsequently, the polygon was vectorized and its area calculated. In this way, it was possible to approximate the area in 2014 and 2016 and thus estimate the increase in the extraction zone. The quantitative results of this operation are shown in the following table 5.2.

Table 5.2. Estimation of the extracted surface in the quarry.

| <i>Survey</i> | <i>Estimated area (m²)</i> | <i>Estimated area (ha)</i> |
|------------------|---------------------------------------|----------------------------|
| 2014 | 1611885 | 161.2 |
| 2016 | 1748677 | 174.9 |
| <i>Variation</i> | 136792 | 13.7 |

The following analysis of the quarry under study was then carried out directly on the DEMs, elaborated from the two point clouds.

5.2.2 | Elevation analysis

Firstly, please note that the inner area of the two large holes was removed from the DEM analysis because at the time of the measurements there was a significant difference in the water level. In fact, in 2016, up to 27 m more water level is measured than in 2014.

In particular, the two digital models of the surface obtained are shown in the following figure 5.4. The resolution of the survey in 2014 is better than that of 2016: 0.2558 m and 0.3255 m. This was because the average flight altitude of the UAV during the survey was lower for the first (290 m) and higher for the second (352 m).

On the left is possible to observe the result of the 2014 survey and, on the right, of 2016. For a clearer visualization and interpretation of the rasters, they were themed using a color-scale based on a hillshade (figure 5.4).

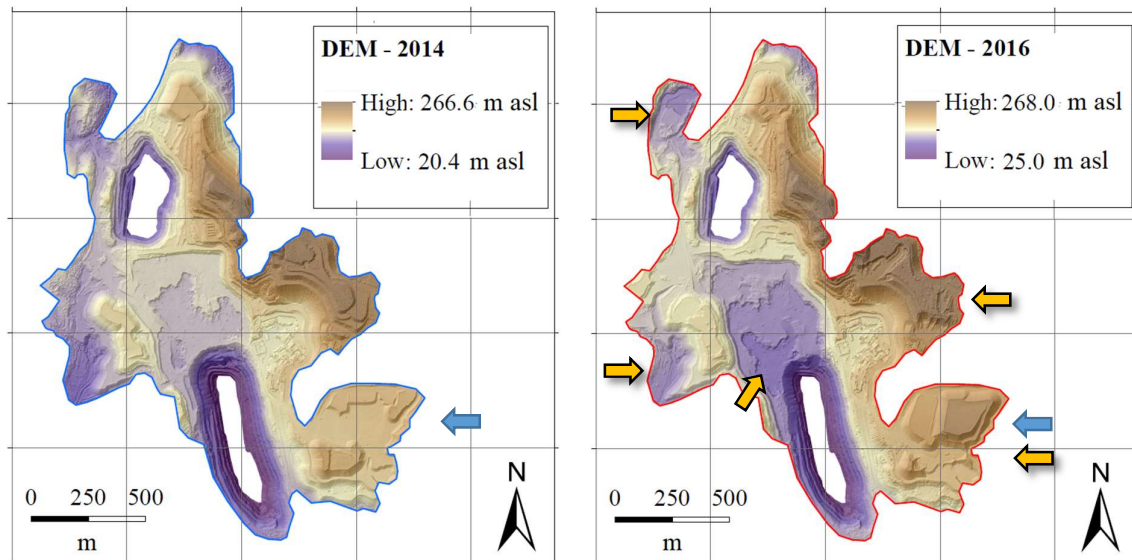


Figure 5.4. Comparison between 2014 (left) and 2016 (right) DEMs. The blue arrow indicates one of the most important deposit of the quarry. The yellow arrows indicate the areas of greatest variation.

As can be seen by the figure 5.4, the two elevation models are not identical but there are significant variations due to excavation and deposit activity inside the quarry. For example, a significant difference can be observed at the level of one of the main deposits of the mine, located in the south-east of the quarry and indicated by the blue arrow (for this reason, a detailed analysis of this area will be shown in next chapter).

5.2.3 | Slope analysis

An interesting geomorphological analysis starting from DEM is the calculation of the slope, in order to obtain a themed map that showing the areas with different value. The results obtained by applying the algorithm to the DEMs under study (using a 7x7 cells kernel) are shown in the following figure 5.5. For this work the slope has been calculated in degrees and varies in a range between 0 and about 90 degrees.

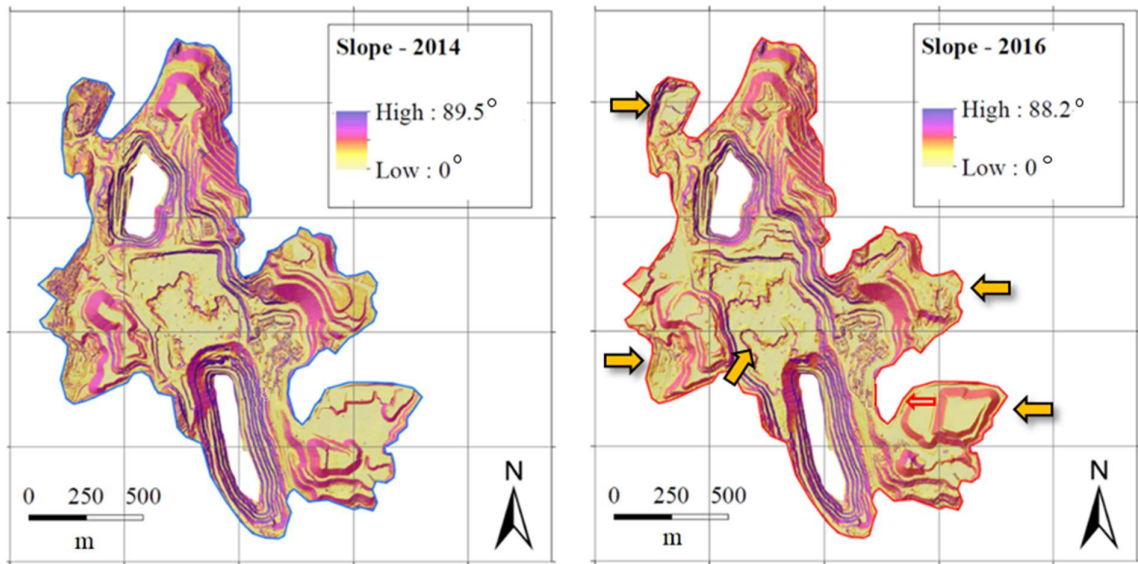


Figure 5.5. Comparison between 2014 (left) and 2016 (right) slope (deg) rasters. The red box highlights a terraced area. The yellow arrows indicate the areas of greatest variation.

An interesting key for interpreting this map is the observation of sudden variations in the slope value, easily observable through the themed raster. In particular, this operation clearly shows the terraces excavated inside the large holes of the open pit mine as a method of extraction of the material.

In addition, when the slope is calculated from two DEMs processed by surveys at different times, it can be used interestingly to identify morphological changes in the surface. This is because if the surface has undergone large variations in slope, which is very common in mining areas, the slope rasters clearly show the differences. By way of example, the following figure 5.6 shows how the slope has been strongly modified within mine area in two years.

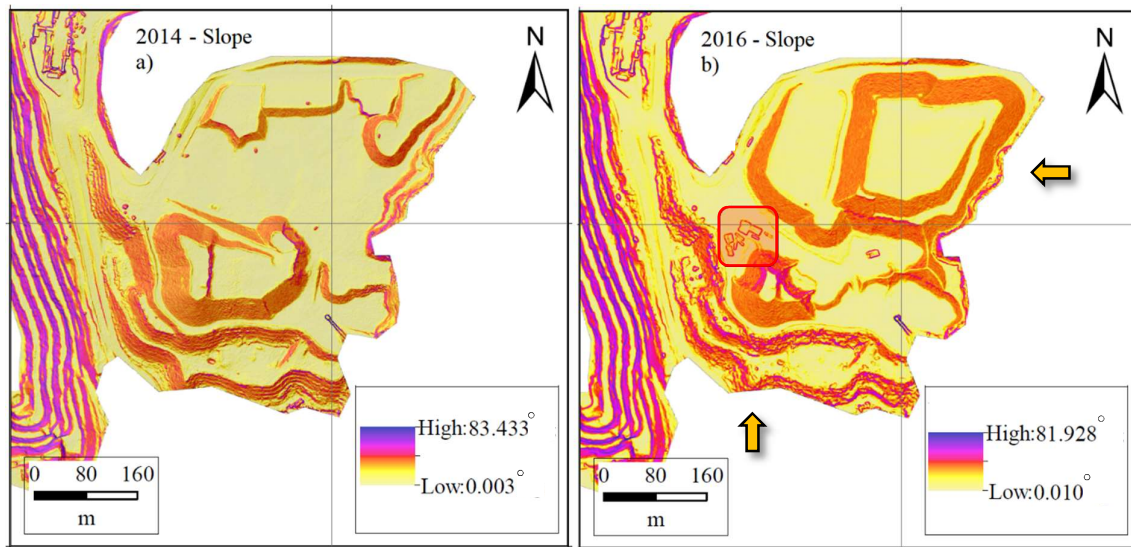


Figure 5.6. Enlargement of the two rasters of the slope in the area of the large deposit to the south-east. The map allows to clearly appreciate the changes in the surface after two years from the first survey. The red box identifies a group of new buildings. The yellow arrows indicate the areas of greatest variation.

5.2.4 | Aspect analysis

This chapter is dedicated to the analysis of the exposure of the surface of the quarry with respect to the four cardinal points. The Aspect raster is made up of cells whose value varies from 0 to 360 degrees, where values 315 to 0 and from 0 to 45 mean exposure to the north, 45 to 135 degrees to the east, 135 to 225 degrees to the south and 225 to 315 degrees to the west. The following figure 5.7 shows the result of the application of this algorithm.

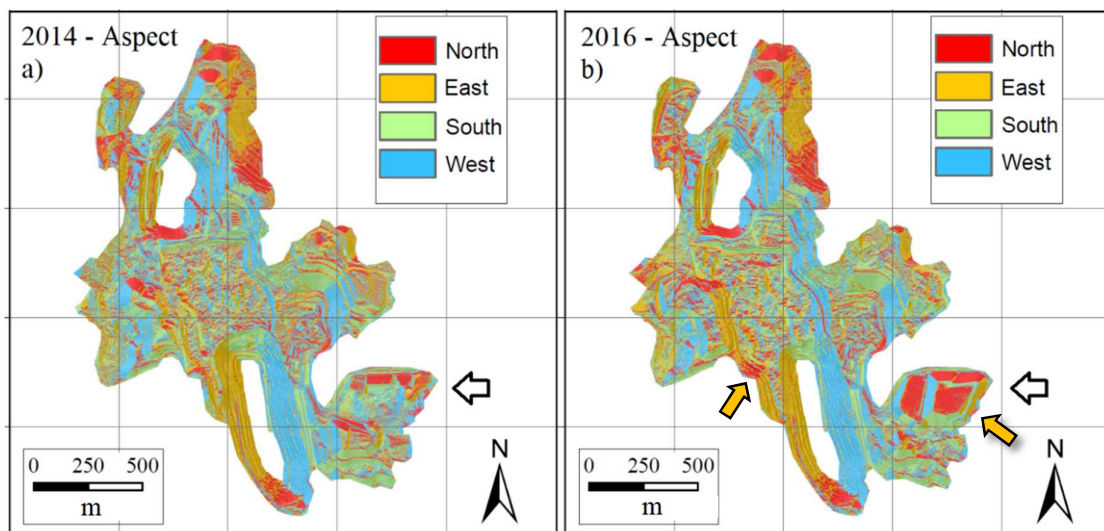


Figure 5.7. Comparison between 2014 (a- right) and 2016 (b-left) aspect. Black arrow indicates the main deposit. The yellow arrows indicate the areas of greatest variation.

A significant change in the surface is appreciable from the raster of exposure especially in the southeast of the quarry, at the level of the main deposit, as in figure 5.8 (according to N-S-E-W direction).

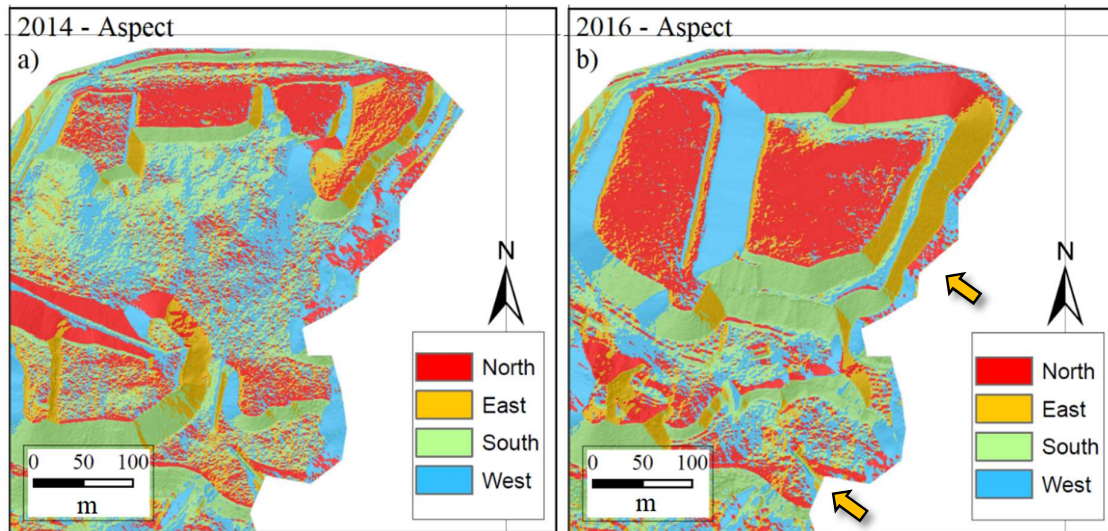


Figure 5.8. Comparison between 2014 (a- right) and 2016 (b-left) aspect in the main southeast deposit. The yellow arrows indicate the areas of greatest variation.

5.2.5 | Curvature analysis

In this chapter, the results of applying the profile curvature and the plan curvature algorithms will be shown. In particular, as already described in chapter 4.3, the first technique highlights the presence of terraces and profiles, while the second highlights any ridges or valley.

About profile curvature and given a 7x7 kernel, a negative value indicates the surface is upwardly convex at central cell and a positive one indicates the surface is upwardly concave at that cell. About plan curvature and given a 7x7 kernel, a positive value indicates the surface is laterally convex at the central cell and a negative one indicates the surface is laterally concave at that cell. The figure 5.9 shows the application of profile and plan curvature algorithms on 2014 and 2016 DEMs.

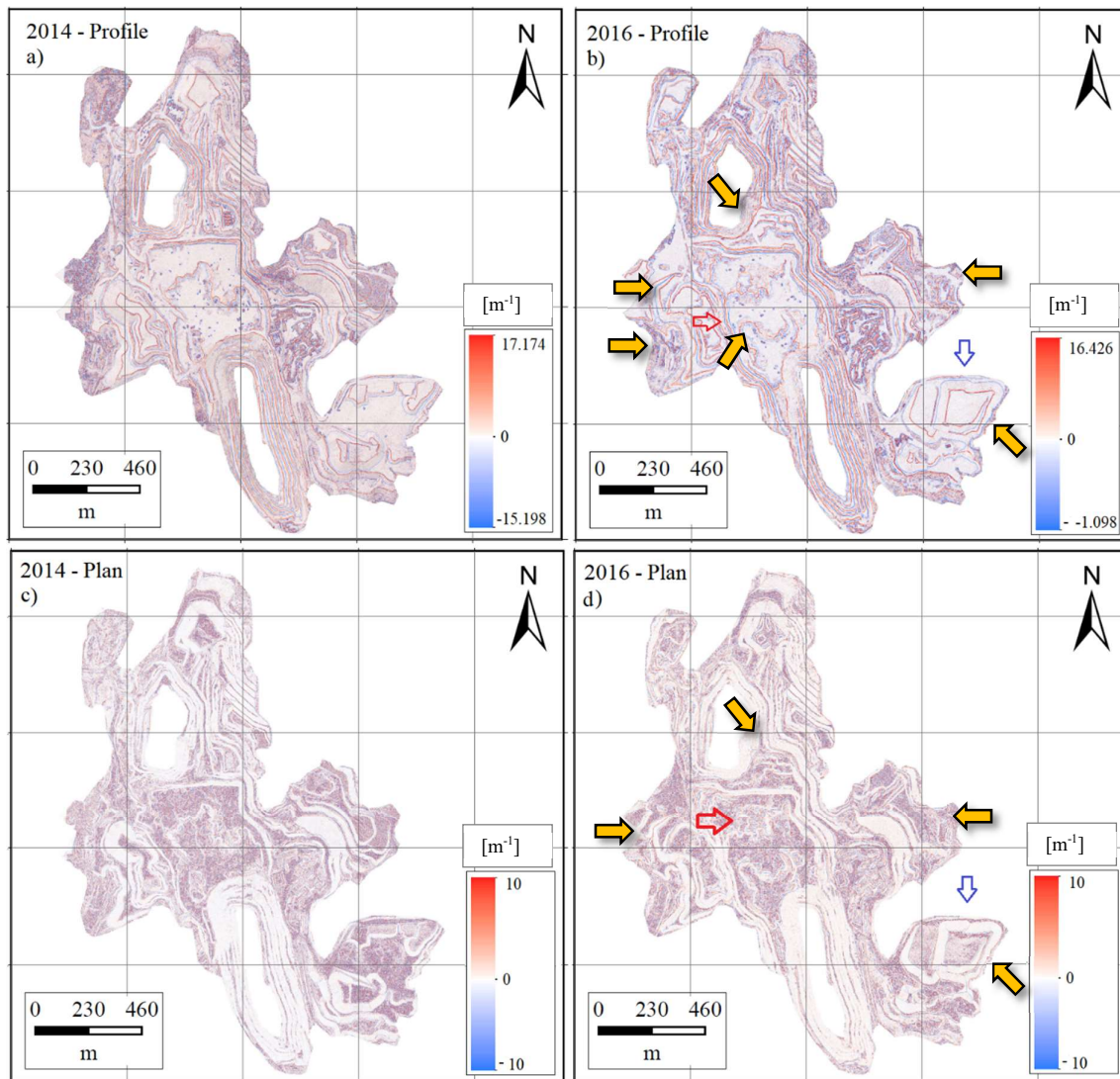


Figure 5.9. Comparison between 2014 (a) and 2016 (b) Profile and 2014 (c) and 2016 (d) Plan curvature. Blue arrow indicates the main deposit and the red one indicates the extraction area. These portions of mine will be zooming in late. The yellow arrows indicate the areas of greatest variation.

In order to better appreciate the potential of the curvature, the enlargements of the south-eastern deposit area and of the central extraction area of the mine are shown below. As can be observed from them, proposed in the following two figures 5.10 and 5.11, the rasters of curvature underline the areas subject to high curvature, outlining and perimetering the various features of the surface. In particular, the profile curvature algorithm describes in a very functional way the sudden curvature variations and is therefore useful, for example, in identifying with excellent precision the extension of the deposits, the vertical walls of the excavations in the mine and the terraces in the main hole. On the other hand, the plan curvature algorithm is more functional in identifying and describing micro topography on the ground, especially for understanding the convergence and divergence of flow across a surface.

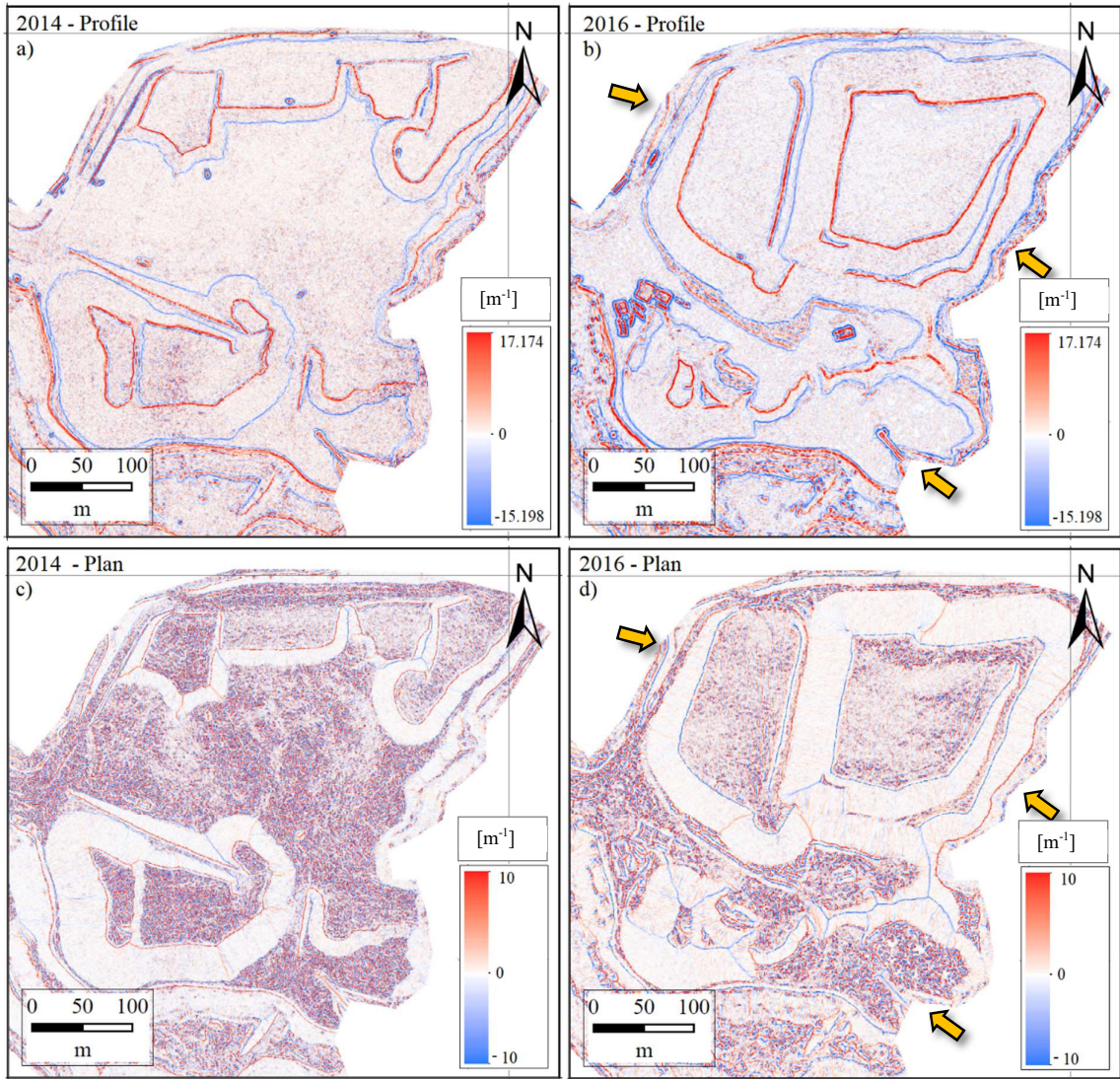


Figure 5.10. Comparison between 2014 (a) and 2016 (b) Profile and 2014 (c) and 2016 (d) Plan curvature in the main deposit. The yellow arrows indicate the areas of greatest variation.

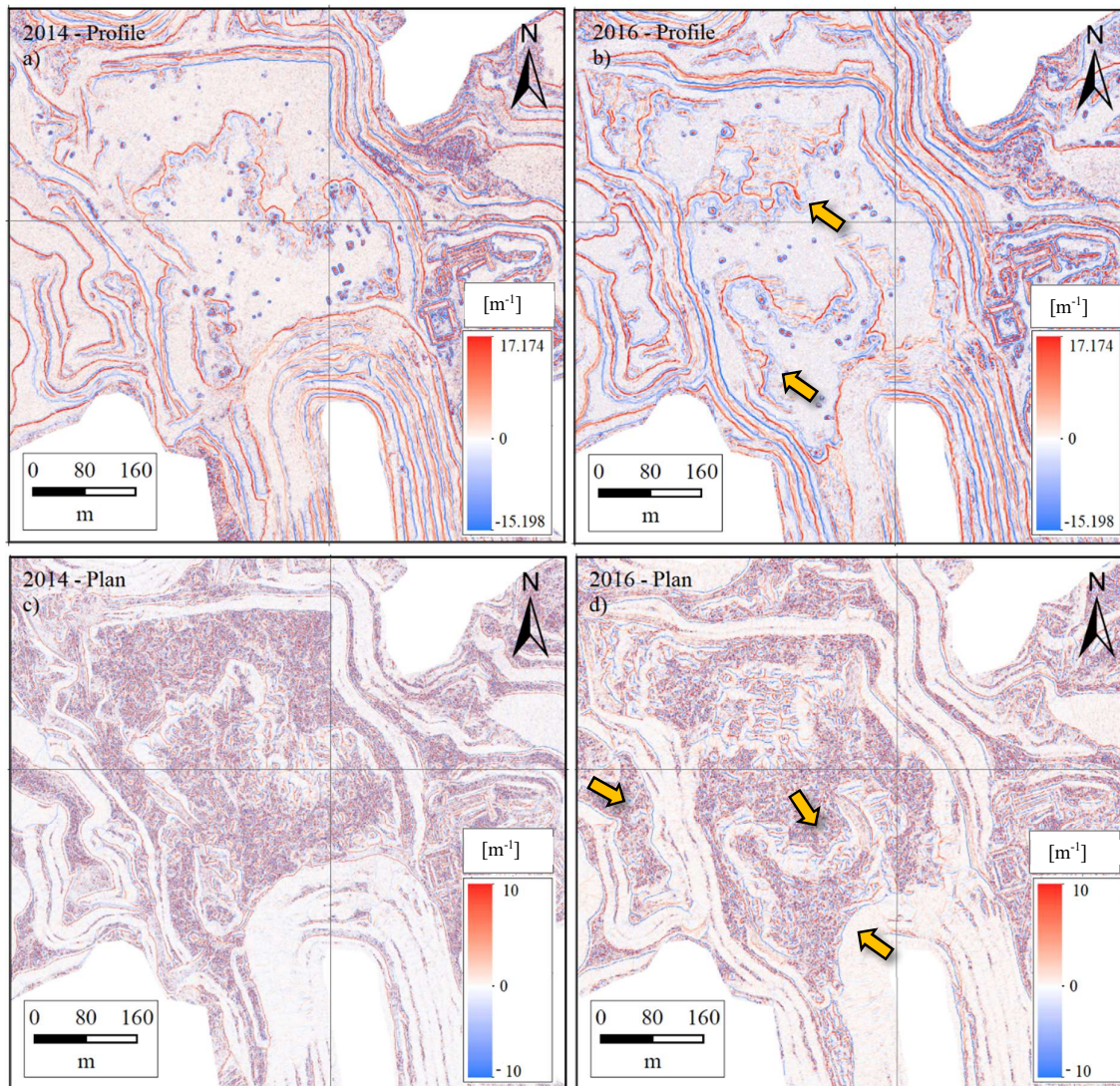


Figure 5.11. Comparison between 2014 (a) and 2016 (b) Profile and 2014 (c) and 2016 (d) Plan curvature in the main excavation. The yellow arrows indicate the areas of greatest variation.

Even in the case of the analysis of the curvature, two measurements made on the same area at different times allow to identify in an exhaustive way all the possible changes (just look at the maps in the previous figures to realize it). For this reason, this analysis is very important inside a mine, where erosion processes are continuous and extremely impactful.

5.2.6 | Roughness indexes analysis

The results of the application of the Roughness-elevation-index and the Roughness-slope-index algorithms are proposed below. In particular, in figure 5.12, the application of Roughness-elevation-index at the level of entire mine in 2014 and 2016 is reported. Red area indicates the higher roughness in the surface.

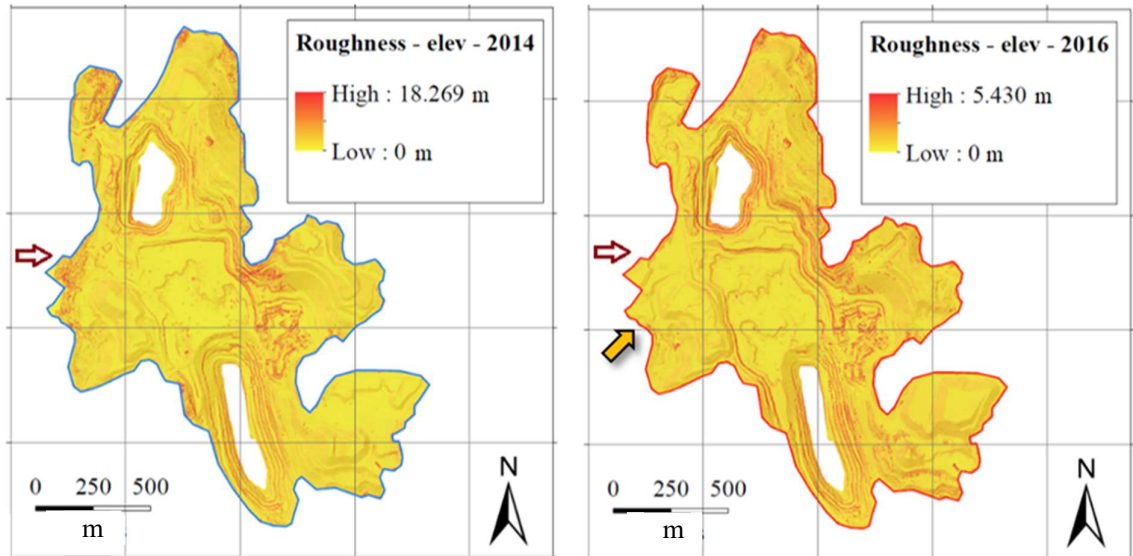


Figure 5.12. Comparison between 2014 (left) and 2016 (right) Roughness-elev rasters. The red box highlights the terraced area, the dark red indicates the expansion area of the mine zooming below and the yellow indicate the greatest variation.

In particular, the calculation of the roughness may show possible variations in the micro topography of the surface. The following figure 5.13, for example, shows the calculated roughness in a mine area that had not yet been massively excavated in 2014, and then compares it with the roughness calculated in 2016, where excavation operations were started. The map shows a greater roughness in 2014 and a lesser one in 2016, proof of the simplification suffered by the ground as a consequence of excavation operations.

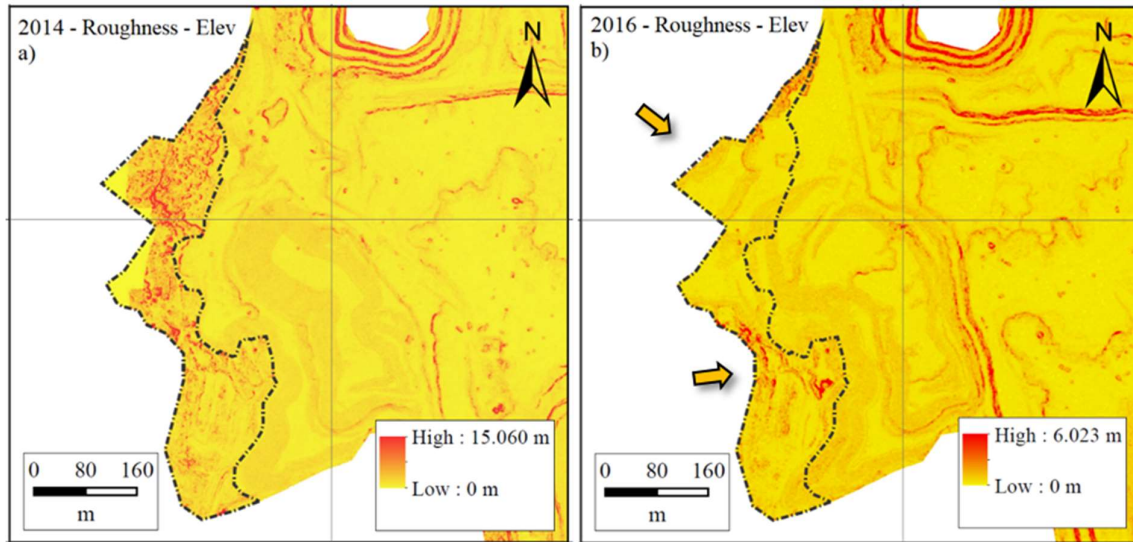


Figure 5.13. Comparison between 2014 (a) and 2016 (b) Roughness-elev rasters. The excavation operations have simplified the topography with a drastic reduction in roughness. The yellow arrows indicate the areas of greatest variation.

Moreover, the results of the application of the Roughness-slope-index, calculated using the focal statistic tool in a 7x7 kernel are shown in the figure 5.14 below.

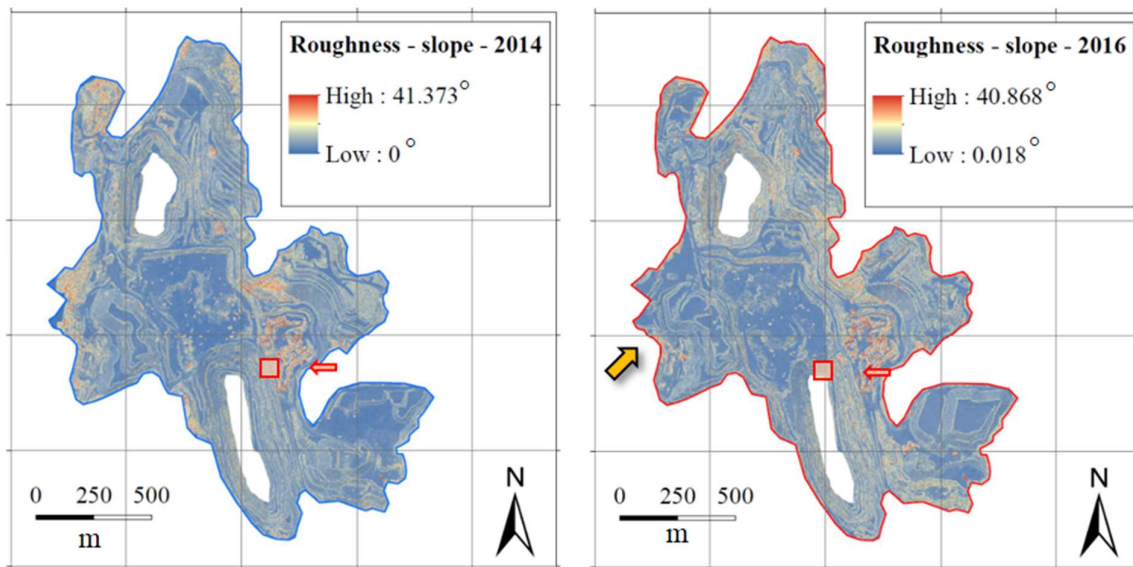


Figure 5.14. Comparison between 2014 (left) and 2016 (right) Roughness-elev rasters. The red box highlights a terraced area. The yellow arrow indicate the areas of greatest variation.

The enlargement at the level of the terraced area, where some variation has occurred (yellow arrows) is proposed in the following figure 5.15. Red area is where the roughness is higher.

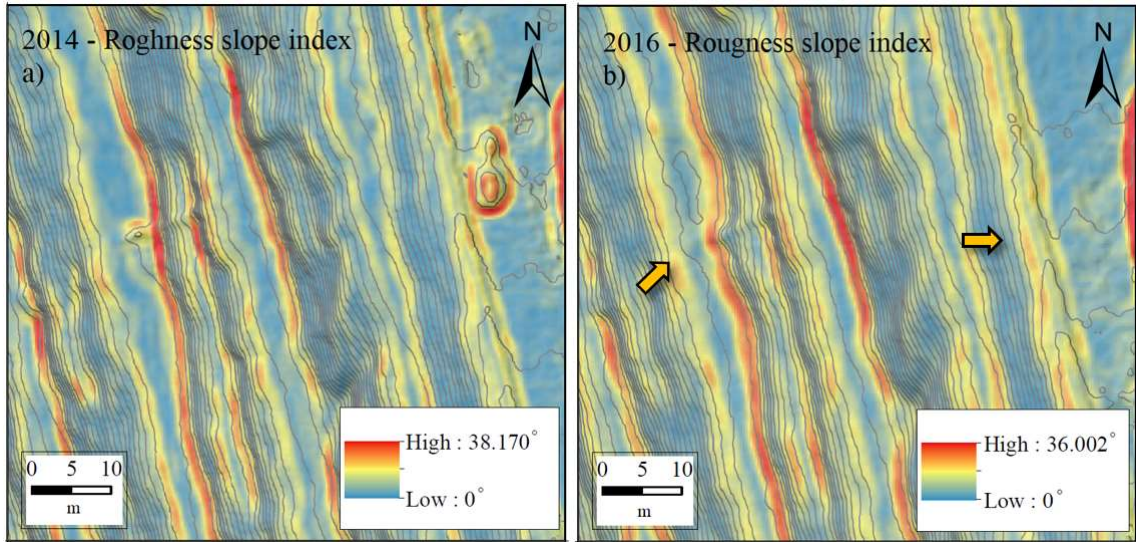


Figure 5.15. Enlargement of the roughness index-slope map inside the southern hole, characterized by a morphology of terracing. a) is about 2014 and b) 2016.

In addition, also in this case, if the two reliefs in the new area belonging to the mine are compared, it is possible to observe a simplification of the topography due to the excavation operations clearly observable by the roughness rasters in figure 5.16.

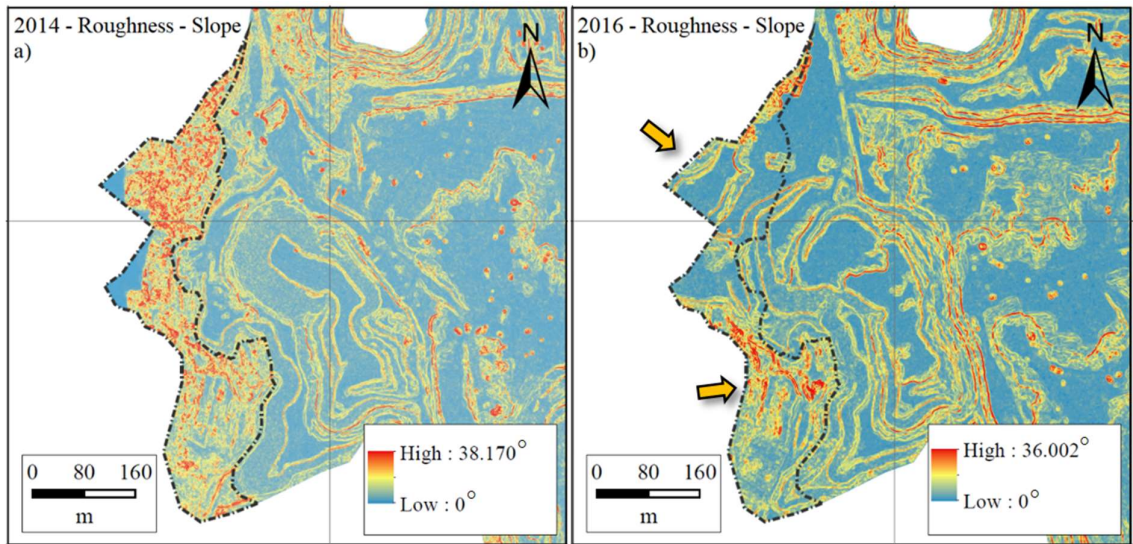


Figure 5.16. Comparison between 2014 (a) and 2016 (b) Roughness-slope rasters. The excavation operations have clearly simplified the topography of the ground, with a drastic reduction in roughness. The yellow arrows indicate the areas of greatest variation.

5.2.7 | Main Statistical information of geomorphological analysis

In this section are reported some of the fundamental statistical parameters described in numerical form, that at the reading allow observing some changes between the two DEMs. The reason why it was decided to pursue this analysis can be seen in the following chart 5.1, showing the distribution of the elevations of the same mine of study, but at two different times.

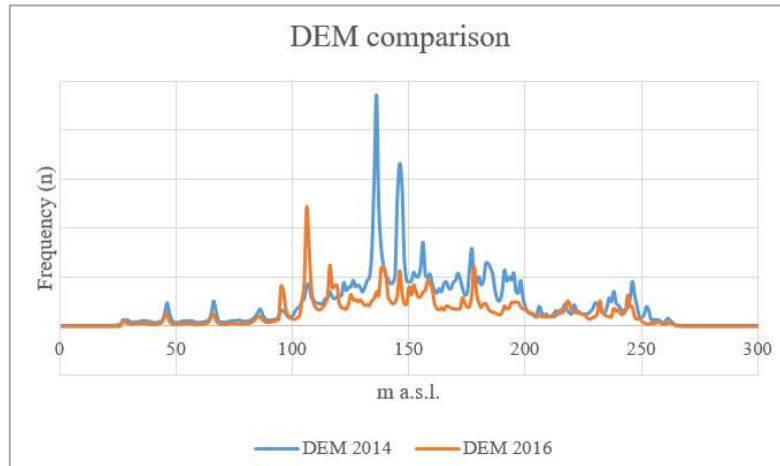


Chart 5.1. Comparison of the elevation distribution in the two DEMs.

As can be seen, the two curves, which in case of non-erosion should match, are different because of the excavation operations. As proof of this and of the strong modification of the topography, the observation of the minimum, mean and maximum values of the elaborated geomorphological analyses reported in the following table 5.6 also show a clear divergence.

Table 5.3. Main statistical parameters of 2014 and 2016 geomorphological analysis.

| 2014 | Min | Mean | Max | σ |
|--------------------------|------------|-------------|------------|----------------------------|
| <i>Elevation [m]</i> | 20.430 | 156.552 | 266.622 | 45.052 |
| <i>Slope [deg]</i> | 0.001 | 22.580 | 87.044 | 18.754 |
| <i>Aspect [deg]</i> | 0.000 | 184.402 | 360.000 | 98.600 |
| <i>Profile Curvature</i> | -15.199 | -0.009 | 17.174 | 0.323 |
| <i>Plan Curvature</i> | -10.000 | -0.004 | 10.000 | 1.899 |
| <i>Roughness [m]</i> | 0.000 | 0.060 | 15.060 | 0.109 |
| 2016 | Min | Mean | Max | σ |
| <i>Elevation [m]</i> | 25.038 | 153.107 | 268.051 | 48.326 |
| <i>Slope [deg]</i> | 0.001 | 22.807 | 85.926 | 18.700 |
| <i>Aspect [deg]</i> | 0.000 | 182.681 | 360.000 | 99.771 |
| <i>Profile Curvature</i> | -6.581 | -0.009 | 16.427 | 0.307 |
| <i>Plan Curvature</i> | -10.000 | -0.006 | 10.000 | 1.712 |
| <i>Roughness [m]</i> | 0.000 | 0.068 | 6.024 | 0.102 |

5.3 | Volume quantification

This chapter will explore and investigate the changes in the mine surface from 2014 to 2016, due to mining operations. In particular, three distinct spatial and volumetric analyses will be made: 1) one of the entire quarry, 2) one in the central part of the mine and 3) another one in the large south-eastern deposit.

The volume estimate was carried out using the Geomorphic-Change-Detection[®] software, developed by Utah State University, and using the two DEMs of 2014 and 2016 as a starting point. DEMs are compared by calculating the DEM of Different (DoD), described in more detail in chapter 4.4.

Firstly, a new GCD project was created. Subsequently, the two DEMs to be compared were entered in the input folder. In this phase, the software also allows the calculation of any associated surfaces such as, for example, slope, roughness and associated error surface according to a spatially uniform Lod.

The comparison between the two surface models and, in particular, the calculation of the DoD, was finally carried out using a probabilistic approach with a confidence value t of 95%.

The results obtained are shown below both in terms of graphics, tables and on a dedicated thematic map. They are indicated in two ways: raw, i.e. not considering the threshold value that separates an effective topographical variation with noise, and thresholded, i.e. considering the threshold value for calculating the volume.

5.3.1 | DoD analysis of entire open-pit mine

Table 5.4. Results of DoD of entire quarry.

| <i>Areal:</i> | <i>Row</i> | <i>Thresholded</i> | <i>± Error</i> | <i>% Error</i> |
|---|---------------|--------------------|----------------|----------------|
| Total Area of Erosion (m ²) | 696,903.00 | 599,277.00 | | |
| Total Area of Deposition (m ²) | 955,367.00 | 836,338.00 | | |
| Total Area of detectable change (m ²) | | 1,435,615.00 | | |
| Total Area of Interest (m ²) | | 1,652,270.00 | | |
| Percent of Area of Interest with Detectable Change | 86.89% | | | |
| <i>Volumetric:</i> | <i>Row</i> | <i>Thresholded</i> | <i>± Error</i> | <i>% Error</i> |
| Total Volume of Erosion (m ³) | 9,268,572.93 | 9,252,442.56 | ± 101,700.68 | 1.1 |
| Total Volume of Deposition (m ³) | 3,536,880.82 | 3,516,350.63 | ± 141,931.27 | 4.04 |
| Total Volume of Difference (m ³) | 12,805,453.75 | 12,768,793.19 | ± 243,631.95 | 1.91 |
| Total Net Volume Difference (m ³) | -5,731,692.11 | -5,736,091.93 | ± 174,606.74 | -3.04 |
| <i>Vertical averages:</i> | <i>Row</i> | <i>Thresholded</i> | <i>± Error</i> | <i>% Error</i> |
| Average Depth of Erosion (m) | 13.3 | 15.44 | ± 0.17 | 1.1 |
| Average Depth of Deposition (m) | 3.7 | 4.2 | ± 0.17 | 4.04 |
| Average Total Thickness of Difference (m) for Area of Interest | 7.75 | 7.73 | ± 0.15 | 1.91 |
| Average Net Thickness of Difference (m) for Area of Interest | -3.47 | -3.47 | ± 0.11 | -3.04 |
| Average Total Thickness of Difference (m) for Area with Detectable Change | | 8.89 | ± 0.17 | 1.91 |
| Average Net Thickness of Difference (m) for Area with Detectable Change | | -4 | ± 0.12 | -3.04 |

As can be seen from table 5.4, it is interesting to note that in the two years under study the volume eroded, or the volume of material extracted from the quarry, was considerable: over 9 million cubic meters. In addition, about 3 million cubic metres of material were deposited in the two large deposits inside the quarry and the elevation variation range is between ≈ -45 and $+49$ m. As can be seen from the following figure 5.17, most of the material was extracted in the central area of the quarry, while the main deposit is located in the southern part of it.

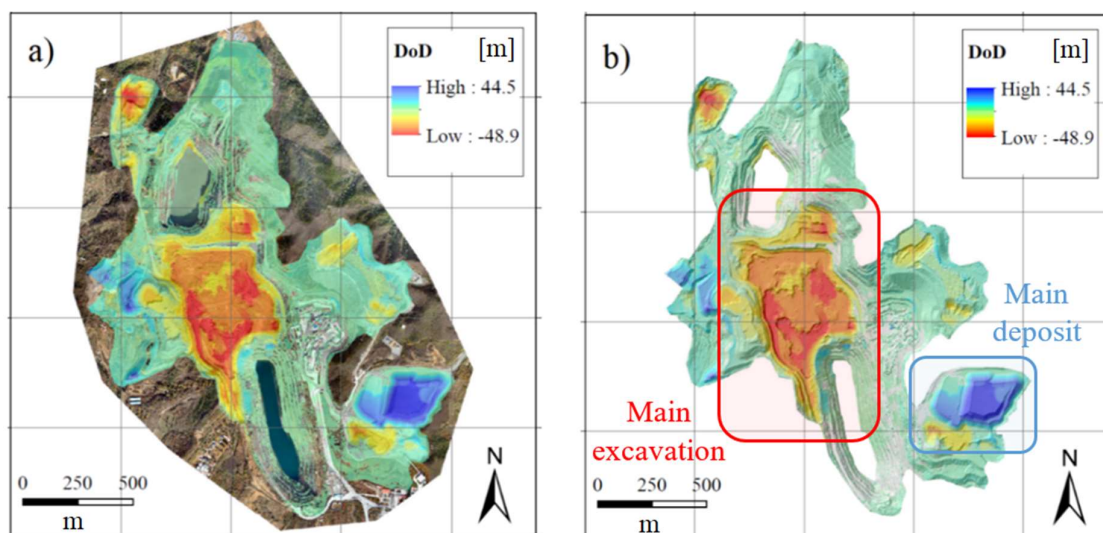


Figure 5.17. Maps of DoD based on a) 2016 orthophoto and b) 2016 hillshade.

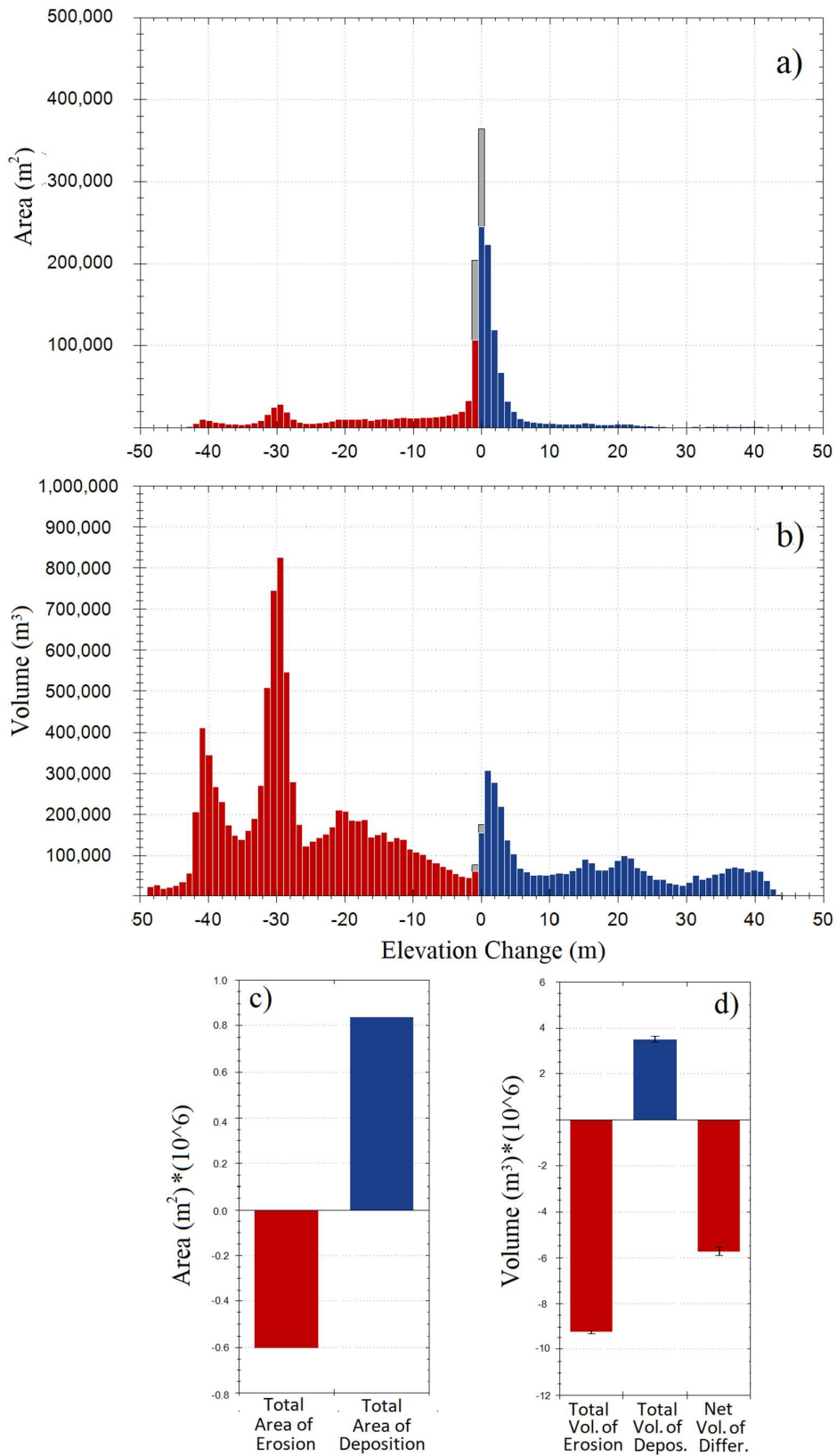


Figure 5.18. Entire mine DoD results observable as a histogram. a) and c) refer to the change in erosion/deposit area; b) and d) refer to the changes in volume.

5.3.2 | DoD analysis of South-East deposit

Table 5.5. Results of DoD of SE deposit.

| Areal: | Row | Thresholded | ± Error | % Error |
|---|--------------|--------------------|----------------|----------------|
| Total Area of Erosion (m ²) | 31,560.00 | 29,812.00 | | |
| Total Area of Deposition (m ²) | 118,568.00 | 112,131.00 | | |
| Total Area of detectable change (m ²) | | 141,943.00 | | |
| Total Area of Interest (m ²) | 150128 | | | |
| Percent of Area of Interest with Detectable Change | | 0.9455 | | |
| Volumetric: | Row | Thresholded | ± Error | % Error |
| Total Volume of Erosion (m ³) | 345,865.09 | 345,608.08 | ± 5,059.26 | 1.46 |
| Total Volume of Deposition (m ³) | 1,795,863.31 | 1,794,586.03 | ± 19,029.26 | 1.06 |
| Total Volume of Difference (m ³) | 2,141,728.39 | 2,140,194.11 | ± 24,088.53 | 1.13 |
| Total Net Volume Difference (m ³) | 1,449,998.22 | 1,448,977.95 | ± 19,690.33 | 1.36 |
| Vertical averages: | Row | Thresholded | ± Error | % Error |
| Average Depth of Erosion (m) | 10.96 | 11.59 | ± 0.17 | 1.46 |
| Average Depth of Deposition (m) | 15.15 | 16 | ± 0.17 | 1.06 |
| Average Total Thickness of Difference (m) for Area of Interest | 14.27 | 14.26 | ± 0.16 | 1.13 |
| Average Net Thickness of Difference (m) for Area of Interest | 9.66 | 9.65 | ± 0.13 | 1.36 |
| Average Total Thickness of Difference (m) for Area with Detectable Change | | 15.08 | ± 0.17 | 1.13 |
| Average Net Thickness of Difference (m) for Area with Detectable Change | | 10.21 | ± 0.14 | 1.36 |

As from the following map 5.19, the south-eastern area is occupied by a large deposit of material of about 15 ha. In two years, a part of this area was excavated through a massive vertical removal up to 30 m; another part of the area was instead destined to the deposit of the extracted material, with vertical variation up to 45 m high. In quantitative terms, the excavated part is about 350 thousand cubic metres, while the material deposited exceeds 1.5 million m³.

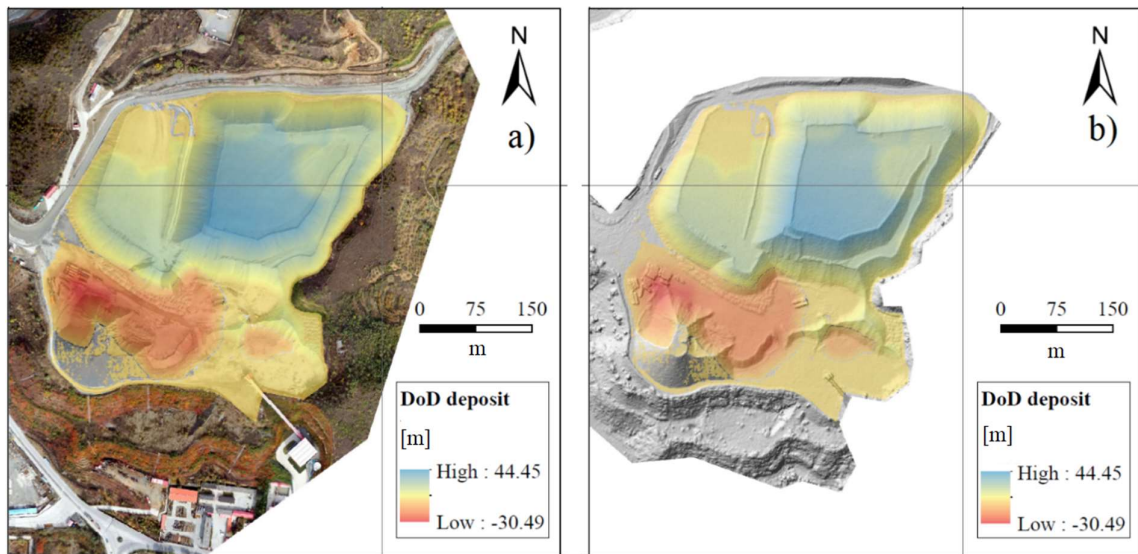


Figure 5.19. Maps of DoD based on a) 2016 orthophoto and b) 2016 hillshade of the SE deposit.

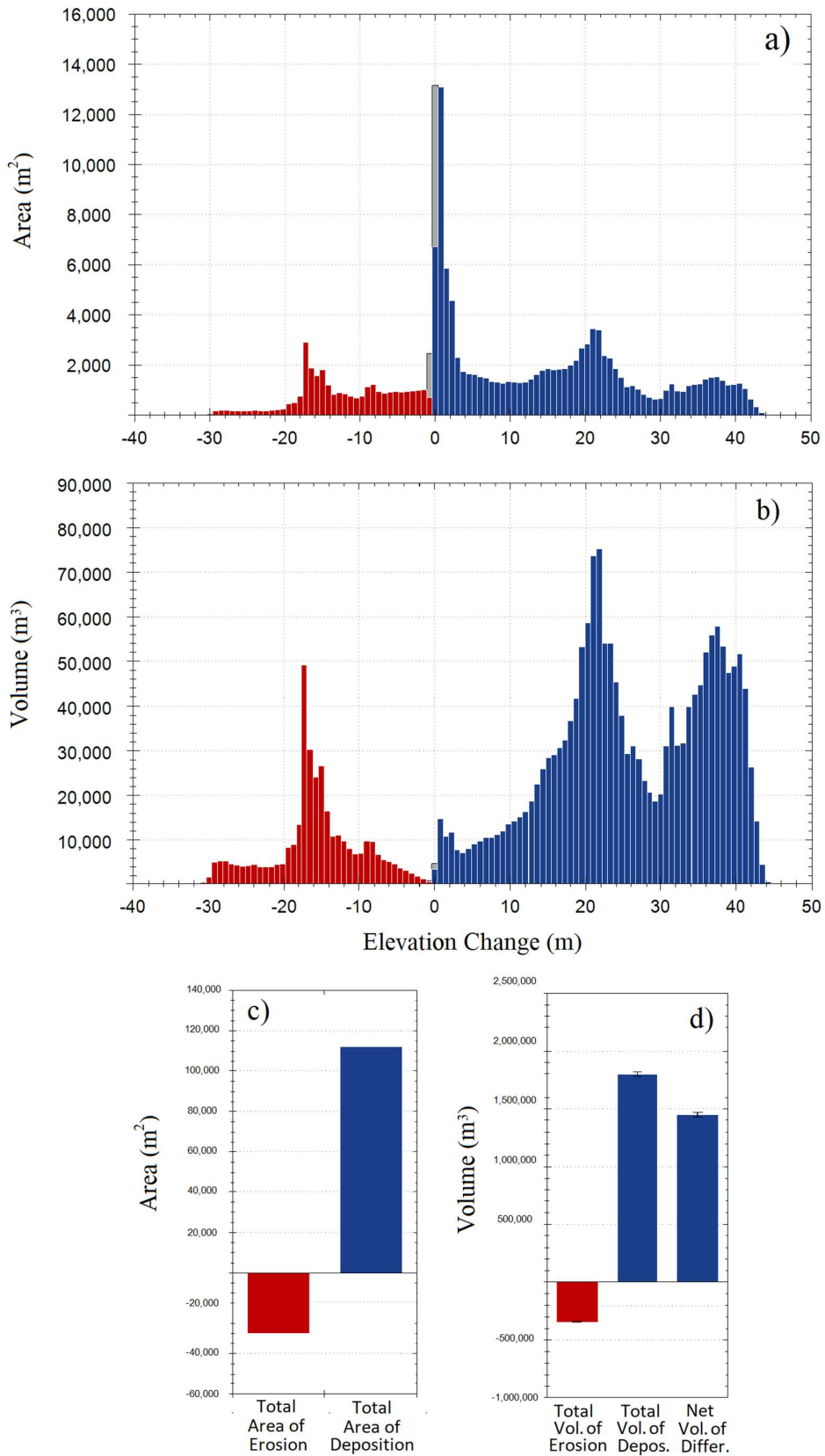


Figure 5.20. Deposit DoD results observable as a histogram. a) and c) refer to the change in erosion/deposit area; b) and d) refer to the changes in volume.

5.3.3 | DoD analysis of central excavation area

Table 5.6. Results of DoD of central excavation.

| Areal: | Row | Thresholded | ± Error | % Error |
|---|---------------|--------------------|----------------|----------------|
| Total Area of Erosion (m ²) | 322,400.00 | 320,467.00 | | |
| Total Area of Deposition (m ²) | 3,781.00 | 2,040.00 | | |
| Total Area of detectable change (m ²) | | 322,507.00 | | |
| Total Area of Interest (m ²) | 326181 | | | |
| Percent of Area of Interest with Detectable Change | | 0.9887 | | |
| Volumetric: | Row | Thresholded | ± Error | % Error |
| Total Volume of Erosion (m ³) | 7,633,433.70 | 7,633,139.27 | ± 54,385.05 | 0.71 |
| Total Volume of Deposition (m ³) | 2,049.86 | 1,799.05 | ± 346.20 | 19.24 |
| Total Volume of Difference (m ³) | 7,635,483.56 | 7,634,938.33 | ± 54,731.25 | 0.72 |
| Total Net Volume Difference (m ³) | -7,631,383.84 | -7,631,340.22 | ± 54,386.16 | -0.71 |
| Vertical averages: | Row | Thresholded | ± Error | % Error |
| Average Depth of Erosion (m) | 23.68 | 23.82 | ± 0.17 | 0.71 |
| Average Depth of Deposition (m) | 0.54 | 0.88 | ± 0.17 | 19.24 |
| Average Total Thickness of Difference (m) for Area of Interest | 23.41 | 23.41 | ± 0.17 | 0.72 |
| Average Net Thickness of Difference (m) for Area of Interest | -23.4 | -23.4 | ± 0.17 | -0.71 |
| Average Total Thickness of Difference (m) for Area with Detectable Change | | 23.67 | ± 0.17 | 0.72 |
| Average Net Thickness of Difference (m) for Area with Detectable Change | | -23.66 | ± 0.17 | -0.71 |

As can be seen from the following figure 5.21, the central area of the mine has been subjected to a strong excavation during the two years of study. The material extracted from this single area is more than 7.5 million cubic metres, with a variation in height of up to about 49 m.

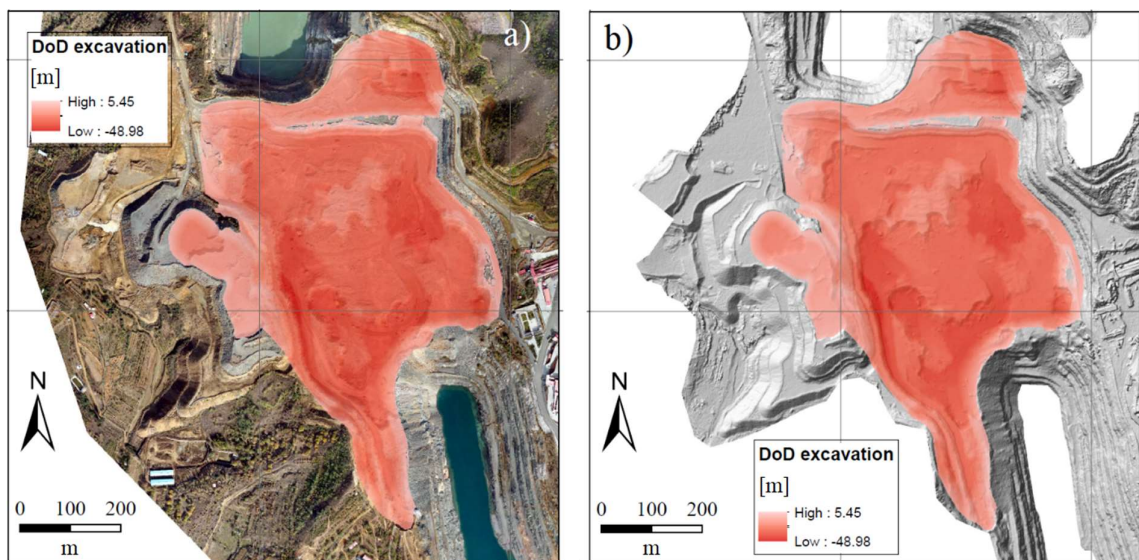


Figure 5.21. Maps of DoD based on a) 2016 orthophoto and b) 2016 hillshade of the central excavation.

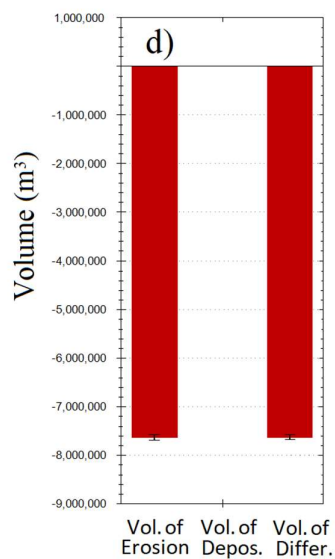
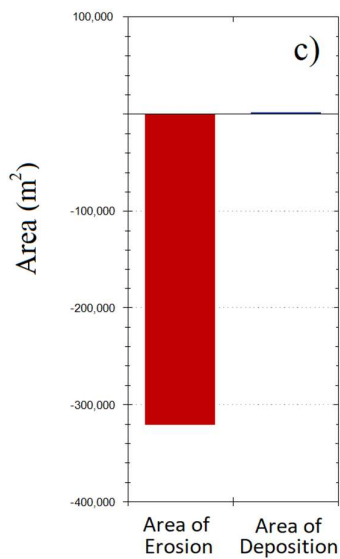
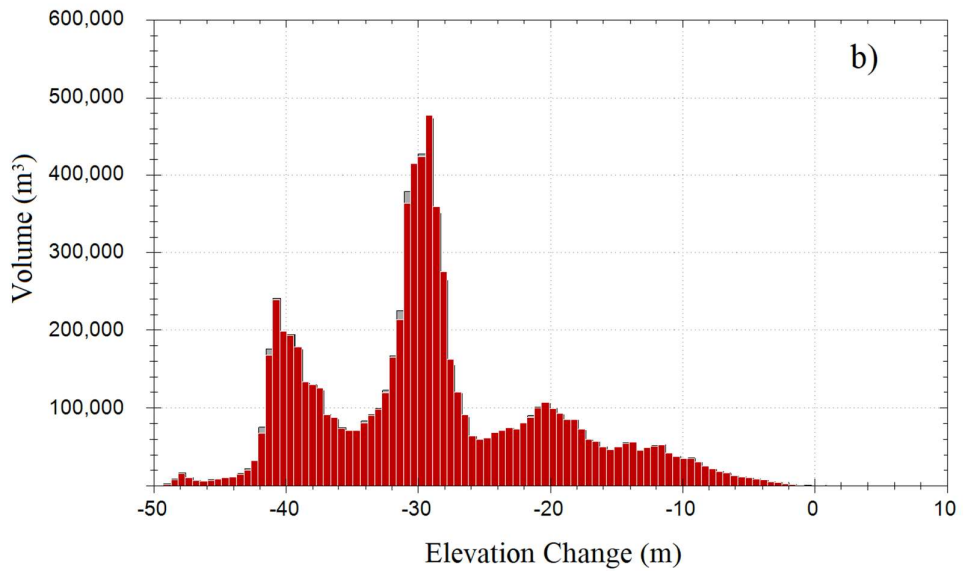
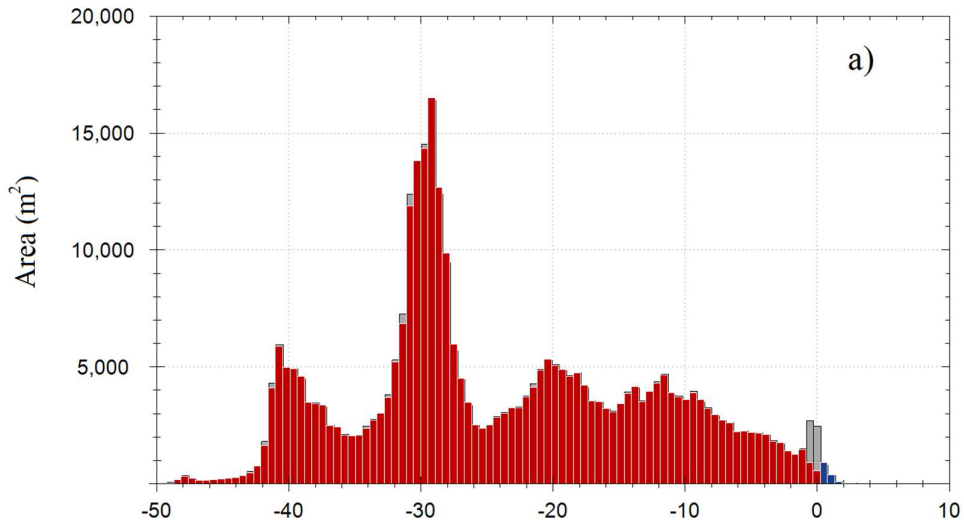


Figure 5.22. Excavation DoD results observable as a histogram. a) and c) refer to the change in erosion/deposit area; b) and d) refer to the changes in volume.

5.3.4 | Tonnage estimation

As can be seen from Table 5.11, the total excavated volume inside the quarry is much higher than the deposited volume. This value is in line with the continuous mining activity during the two-year study. From the extracted volume it is possible to estimate the mass of the material handled in the two years of activity (Xiang et al., 2018). For do this, as reported in Xiang et al. (2018), the volume value has been multiplied by the average of ore-bearing rate (about 20%), the average ore-grade (about 30%) and the average density of iron ore (about 4 t/m³) or of tailings (about 2.5 t/m³).

The results of this application is reported in the next table 5.10.

Table 5.7. Tonnage estimation.

| | <i>Entire mine</i> | <i>South-East Area</i> | <i>Central excavation</i> |
|--|--------------------|------------------------|---------------------------|
| <i>Excavated volume (m³)</i> | 9,252,443 | 345,608 | 7,633,139 |
| <i>Error (m³)</i> | ± 101,701 | ± 5,059 | ± 54,385 |
| <i>Average of ore-bearing rate</i> | 30% | 30% | 30% |
| <i>Average ore-grade</i> | 20% | 20% | 20% |
| <i>Average density of iron ore (t/m³)</i> | 4 | 4 | 4 |
| <i>The mined ore tonnage (t)</i> | 2,220,586 | 82,946 | 1,831,953 |
| <i>Error (t)</i> | ± 24,408 | ± 1,214 | ± 13,052 |

5.4 | Subsidence estimation

5.4.1 | Subsistence estimation for the road's surfaces

In this chapter, the two point clouds of 2014 and 2016 have been used to evaluate a possible subsidence of the surface of three different roads inside the open pit mine. The first stretch chosen for the study extends for 232 m around the main deposit site in the south-east of the mine; the second is 464 m long and is located in east part of the mine around the houses; the third road is 602 m long and is located in the north side of the mine. In particular, such analysis may be useful in valuing the collapse of some parts of the road following the transit of vehicles operating in the mine. The software used for this analysis was CloudCompare®.

In the first phase, the two clouds were cleaned of points that did not appear on the road using the "segment" function. Once cleaned, they were aligned using the ICP cloud registration algorithm, using the 2014 survey as a reference and allowing translation and rotation in the three XYZ axes. The algorithm also allows to estimate the co-registration error between the two clouds, defined as 'RMS error'. Once aligned, the 'Compute Distance' tool was used in Cloud Compare® to calculate the distance between the two point clouds. The result of this operation is the creation of a map, appropriately themed, in which are highlighted the areas where the distance between clouds is different from zero and, therefore, where the surface has actually been subject to subsidence or, in general, to changes in elevation.

Anyway, in the three stretches of road, the topographical changes were negative, i.e. they suffered, in some places, a decrease in height certainly due to the continuous transit of heavy vehicles inside the mine.

The next three pages are dedicated to the location of the roads under study, the definition of the areas subject to subsidence and a statistical description of it. In addition, the main statistical parameters of the subsidence results are summarized in table 5.8. The minus sign of the data in the table means that, compared to the survey of 2014, in the two years between the two surveys the road surface has been lowered in some areas highlighted in the map.

Table 5.8. For each section of road, the minimum, mean and maximum subsidence values (lowering of the surface) are indicated. The mean column refers to an average subsidence value of the three road sections.

| | Road I | Road II | Road III | Mean |
|-----------------------|---------------|----------------|-----------------|-------------|
| <i>Min [m]</i> | -0.002 | 0.000 | -0.005 | -0.003 |
| <i>I Quant. [m]</i> | -0.094 | -0.162 | -0.191 | -0.149 |
| <i>Median [m]</i> | -0.186 | -0.325 | -0.383 | -0.298 |
| <i>III Quant. [m]</i> | -0.279 | -0.487 | -0.575 | -0.447 |
| <i>Max [m]</i> | -0.371 | -0.649 | -0.761 | -0.593 |

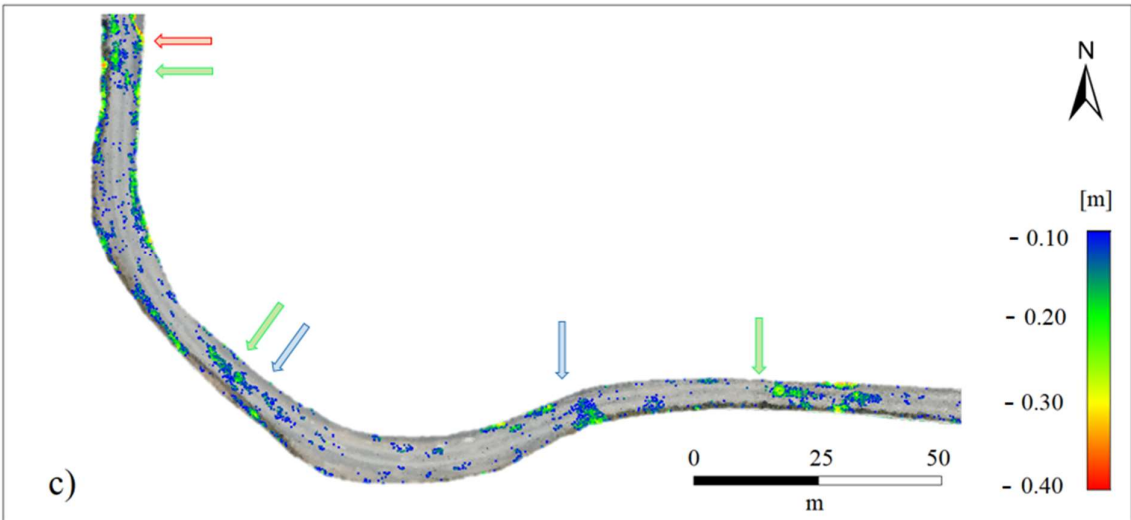
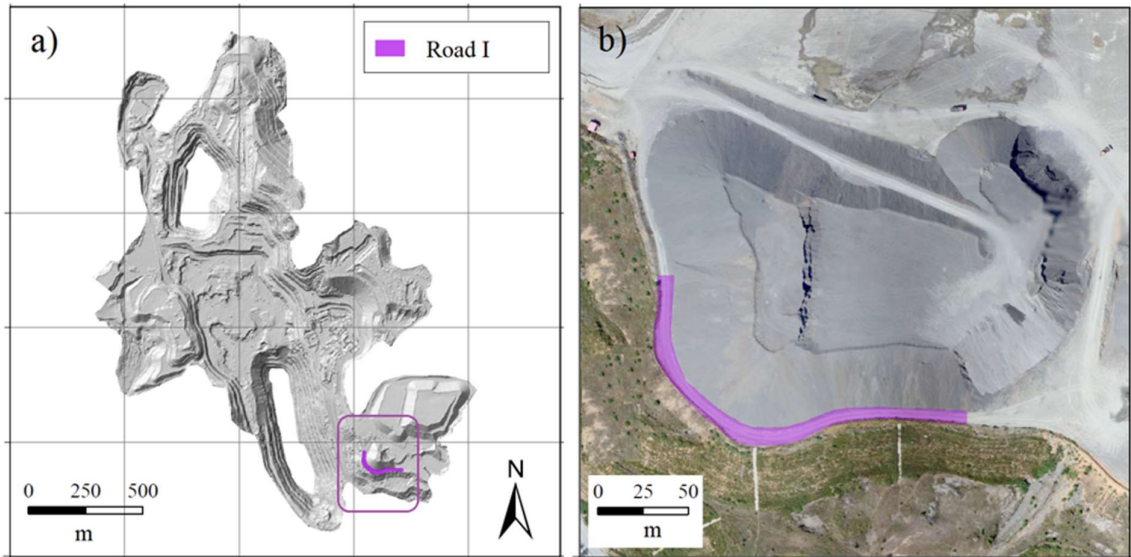


Figure 5.23. a) and b) are the locations of the Road I; c) is the result of the distance calculation.

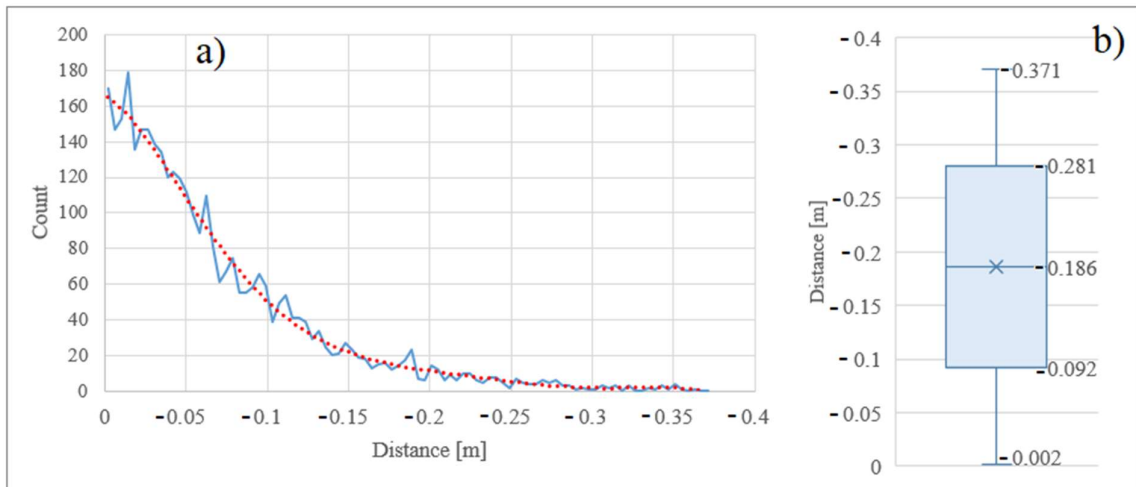


Chart 5.2. Road I. a) graphic result of distance calculation; b) distance box-plot.

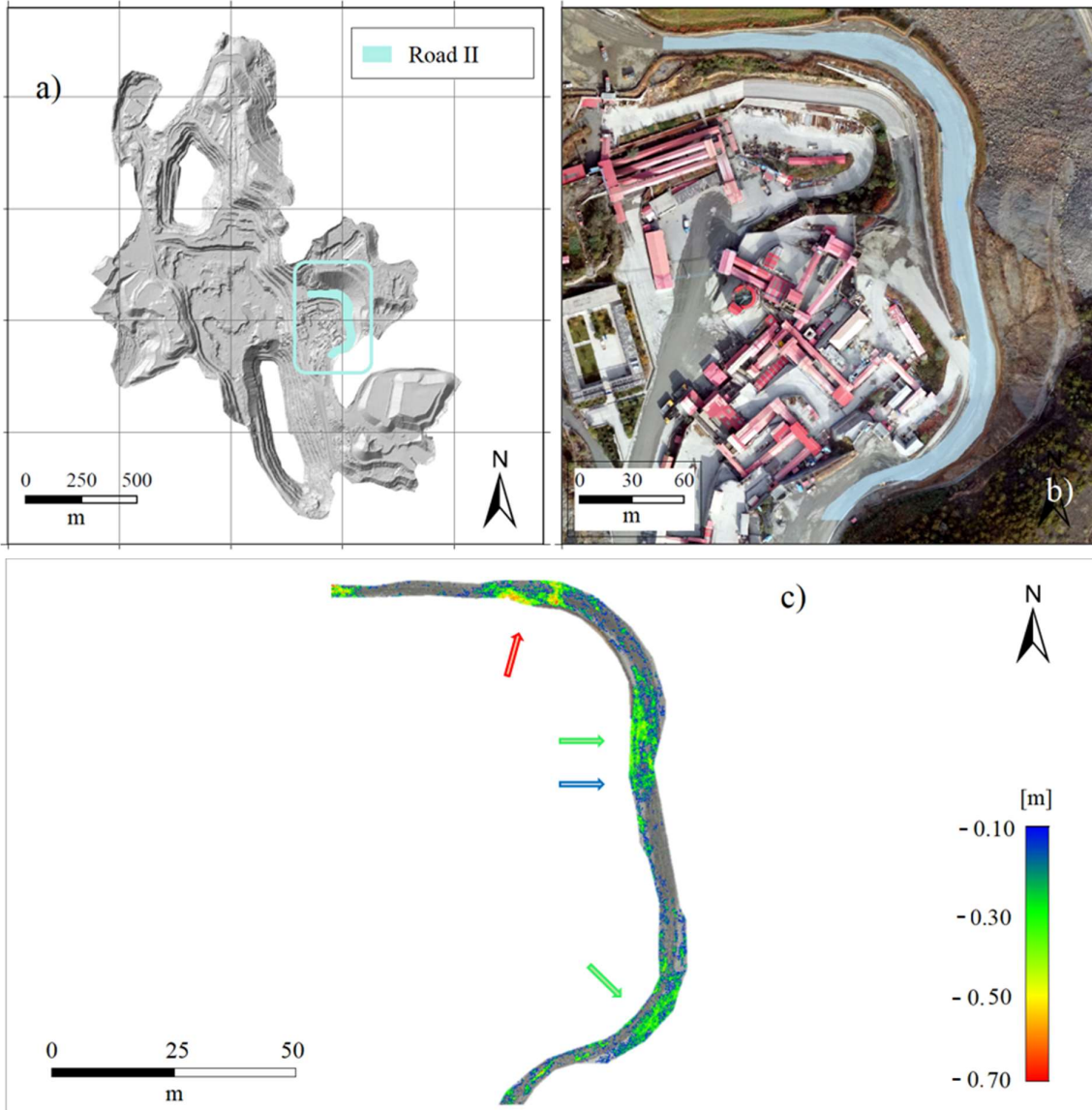


Figure 5.24. a) and b) are the locations of the Road II; c) is the result of the distance calculation.

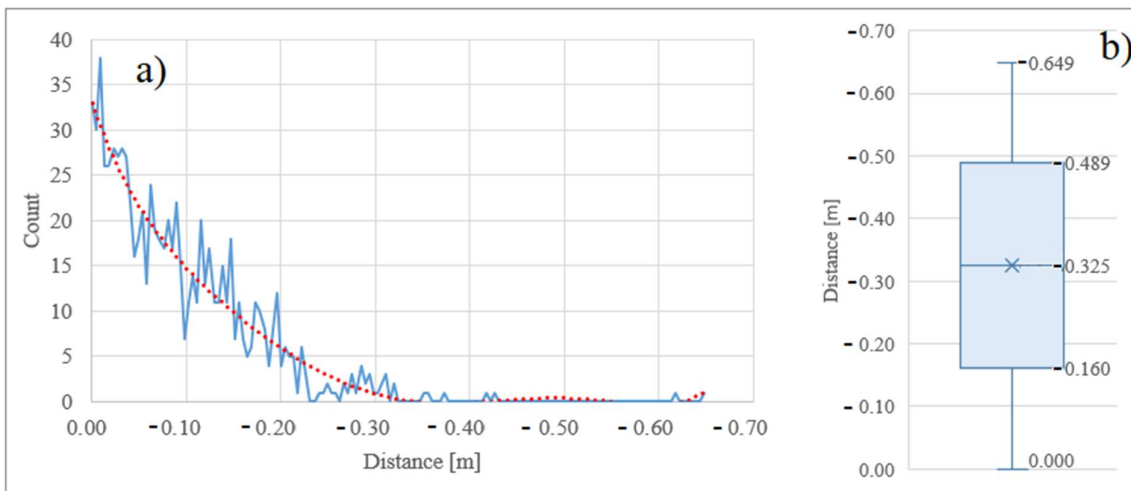


Chart 5.3. Road II. a) graphic result of distance calculation; b) distance box-plot.

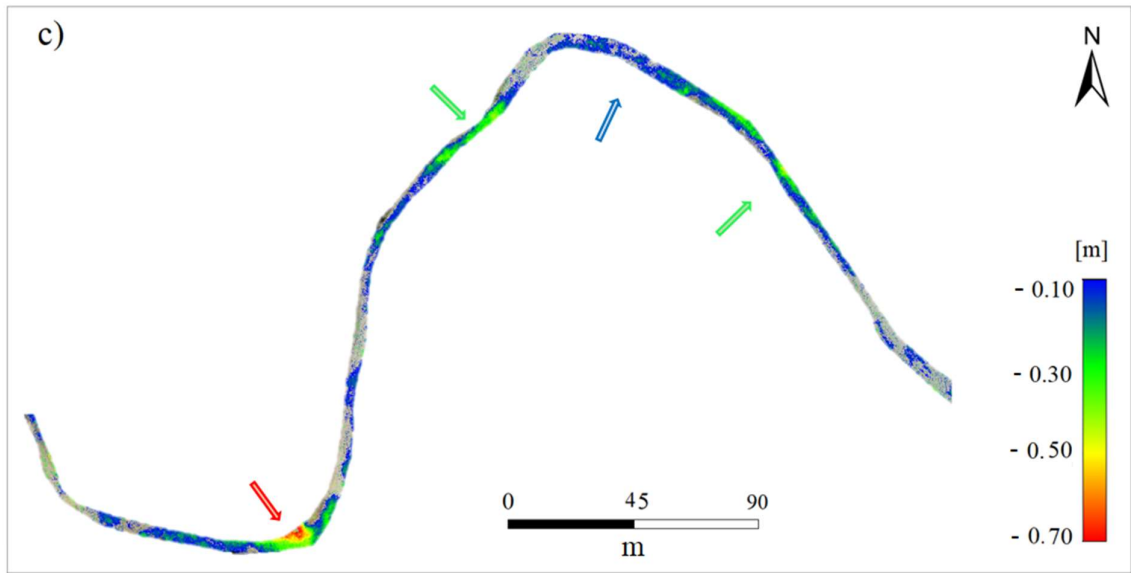
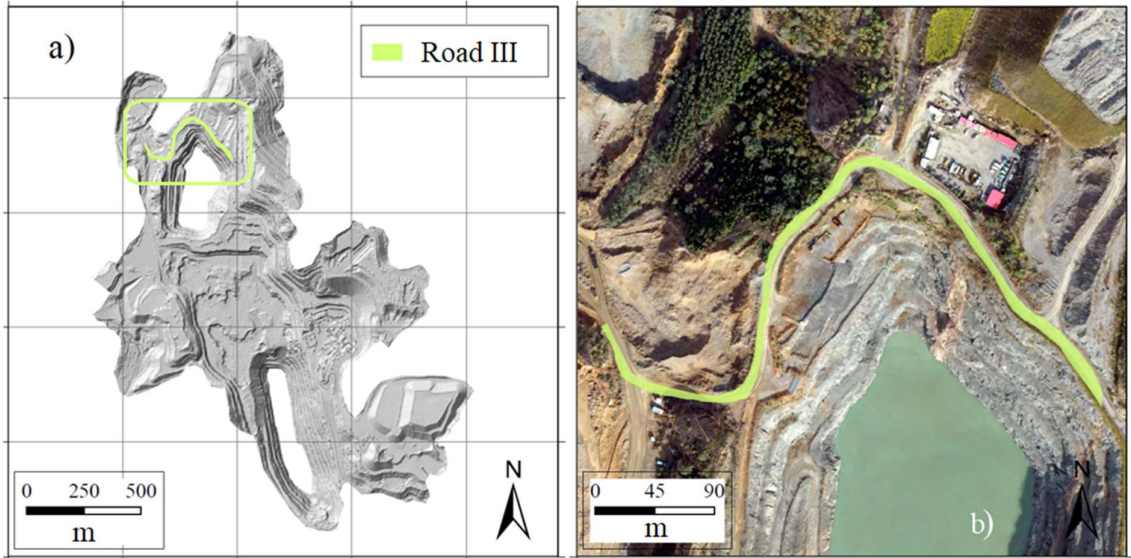


Figure 5.25. a) and b) are the locations of the Road III; c) is the result of the distance calculation

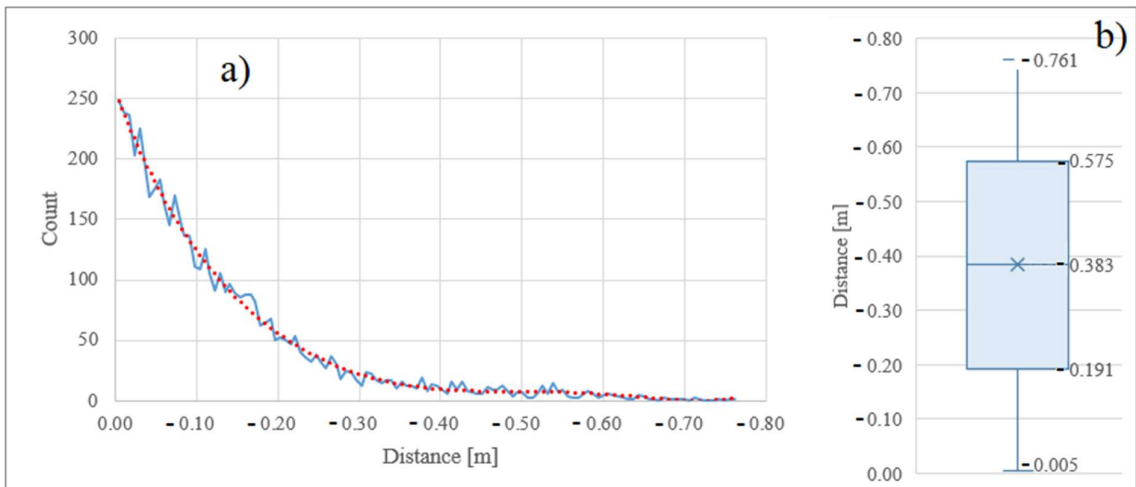


Chart 5.4. Road III. a) graphic result of distance calculation; b) distance box-plot

As can be seen from the maps above, the method offers a clear and simple visualization of the problem of subsidence by comparing two clouds of points. Especially in mining, where the soil is subject to continuous stress and compaction of the road surface (with consequent lowering), this method can provide stakeholders with an indication to understand where the problem of subsidence is and to what extent. Thanks to this, it is then possible to design protection measures to solve the problem with a maintenance plan.

5.4.2 | New challenges for the subsidence estimation using UAV

In general, geological subsidence is slow to evolve and does not cause excessive difficulties in short periods. Human-induced subsidence, on the other hand, are more frequent and have a more serious effect on the environment, especially when they are induced by the overexploitation of underground resources.

A very striking example of this is the abandonment of mines at the end of concessions, because without a serious environmental restoration plan, situations of hazard can arise. A problem of this kind, for example, is present in Korea, where more than 5000 mines have been abandoned without any rehabilitation plan for the mitigation of the hazard (Suh et al., 2017) .

For this reason, to minimize the risk of subsidence, in general where there is a strong human presence, it should be important to create maps to identify and quantify the areas at risk, in order to provide an excellent starting point for the design of protection infrastructure. Of great importance could be the planning of a series of monitoring UAV flights, for example on an annual basis, able to offer a database constantly updated on hazardous areas. In this case, any sudden changes to the surface would be promptly identified to be able to respond preventively to situations of danger.

In this field, the advent of UAVs is opening the doors to countless new case studies. This is thanks to the versatility and relative economy of these aircraft which, equipped with the most advanced technology, offer increasingly precise results in geomorphology.

In this thesis, a multi-temporal methodology for mapping and analysing the subsidence of a stretch of road affected by continuous transit of heavy-vehicles is proposed. Nevertheless, the comparison between two multi-temporal drone surveys of a study area can be useful in countless situations. Through this methodology, for example, UAVs could be used not only for monitoring the Earth surface, but also in engineering and architecture fields to monitor any

subsidence situations of structures. This could be apply to roads, bridges, buildings and also to hydrogeological protection works such as dams and riverbanks.

In particular, a similar case to mining roads are forest roads. In fact, they are periodically subject to use and consequently maintenance is essential to keep them functional. The use of UAVs, especially in stretches where it is possible to fly at a sufficiently high altitude to ensure the quality of the images but avoiding the canopy of the plants ($> 3-4$ m), can offer a very quickly and economically way for estimating subsidence, so as to identify areas that require maintenance.

However, a great advantage of the world of UAVs is therefore their multidisciplinary, and so the ability to offer solutions to problems of different nature, of an environmental or anthropogenic character, through modern and advanced techniques.

6 | CONCLUSION

The aim of this thesis was to use multi-temporal surveying to analyse geomorphological changes, quantify the volume of soil removed/deposited during two years inside an open-pit mine and, finally, analyse subsidence of three roads. To do this, two UAV surveys were carried out within the study area, a mine 80 km northeast of Beijing (PR China), which, using the SfM technique, have allowed the creation of two geo-referenced point clouds and, subsequently, two comparable high-resolution DEMs.

In particular, the two surveys were carried out in August 2014 and October 2016 inside an open-pit mine using a UAV called *SkyWalker X5 Plane*. In both cases, five GCPs were used, with coordinates appropriately measured via RTK-DGPS.

In general, the analysis suggested that the area of the mine under study has increased in size by 13.7 ha, from about 161.2 ha in 2014 to about 174.9 ha in 2016. Moreover, in the two years, mining activities inside the quarry have been considerable, causing a significant modification of the Earth's surface. More in specific, the morphological changes on the surface have been analysed comparing the main geomorphic attributes (elevation, slope, curvature, aspect) and the roughness index of elevations.

In particular, the analysis of the elevation immediately revealed a considerable variation in the topography of the mine, mainly highlighting a lowering of the soil in the central area, affected by excavation, with a consequent increase in the size of southeast main deposit. Starting from this reason, it has been decided to deepen the analysis of the surface variation through the comparison of the two multi-temporal surveys also for the other indicators mentioned above.

The comparison of slope maps was useful especially to analyse the terraced area inside the large holes offering a delimitation of flat areas and walls. The aspect study, on the other hand, clearly showed the massive variation that had taken place in the large southeaster deposit. In fact, the deposition was so massive as to modify the aspect over the entire area. The analysis of the curvature, especially through the profile algorithm, was instead fundamental to highlight the terraces, the shape of the deposits and of the excavations, because, thanks to the identification of the areas with maximum curvature (distinguishing concave and convex), is able to offer maps of simple reading but very effective. On the other hand, the roughness indicator was useful in identifying all those portions of surface that have been affected by extraction over time. The

advent of excavation, in fact, has caused a sort of simplification of the ground, eliminating most of the geomorphological forms that made up the original micro topography of the area, thus causing a drastic reduction in roughness.

The volume excavated and/or deposited in the two years has been also estimated using the DoD (DEM of Difference methodology). The depth of excavation has reached almost 50 m, and in a storage area, located to the south-east, material has deposited up to about 45 m high.

With regard to the estimate of the volume mobilized, $9,252,442.56 \text{ m}^3 \pm 1.1\%$ were excavated in the entire quarry, of which $3,516,350.63 \text{ m}^3 \pm 4.4\%$ were deposited within the perimeter. This means that $5.736.091.93 \text{ m}^3 \pm 3.04\%$ of material was transported to other locations. In particular, the 82.5% of the entire excavated material was taken from the central area, while the remaining 17.5% was taken from the new area belonging to the quarry to the north-west and from the main deposit located to the southeast.

Finally, a comparison between 2014 and 2016 point clouds has been carried out in order to estimate the subsidence of roads surfaces, by calculating the distance between the two appropriately processed clouds. This analysis led to the perimeter of some areas subject to subsidence due to the transit of trucks. The results obtained have an average subsidence (and therefore a lowering of the ground) equal to 0.18 m, a maximum of 0.37 m and a statistical standard deviation of 0.10 m. This analysis is certainly useful for the mine operator because it accurately identifies the degraded areas, thus allowing a quicker and more effective maintenance intervention. Of primary importance is also the issue of monitoring the mines for safety purposes (both for operators of the quarry and for those who frequent the surrounding areas), just think of the significant disasters related to mining activity.

In a world where human expansion is continuous and exponential, it is crucial to offer a multi-disciplinary methodology capable of identifying subsidence in a precise, rapid and economic way (for example, it can be also used in the engineering and architectural field for monitoring infrastructure).

In addition, geomorphological analyses linked to the variations to which the Earth's surface is subject due to human activities has been gaining increasing interest among researchers. A very delicate concept connected with the continuous exploitation of natural resources is certainly the so-called "point of no-return", a tangible and real limit, beyond which the collateral effects of

soil degradation can turn into a real environmental disaster, with very serious consequences for the safety and health of societies.

The intention of this thesis is to describe how modern technologies as UAVs can be used to create a solid, relatively economic and scientifically proven starting point, which aims at quantifying the eroded soil and identifying precisely and accurately the areas subject to variations. The analysis conducted in this thesis can be transferred in any situation of superficial degradation, which offers a topographic survey at high resolution and determines a volumetric quantification of erosion.

On one hand, in mining field, the high definition soil mapping (with a mono and/or multi-temporal approach) may offer an interesting benefit for stakeholders. Just think, for example, at the volumetric estimation of the material, the measurement of the mine and its parts, the identification of deposits, etc., or at all the operation that before the advent of photogrammetry were entirely manual, slow and expensive.

But on the other hand, if it is applied not only in mining but in every situation where surface erosion could be a serious problem, the same methodology allow knowing where the main erosive phenomena are and how the soil could evolve in the future, also identifying areas and offering a useful information for a better environmental management.

-
- Amato, L. (2017). Tecniche innovative per il rilievo e la modellazione del territorio. Retrieved from <http://www.tecnoin.it/?p=482>
- Ambrožič, T., & Turk, G. (2003). Prediction of subsidence due to underground mining by artificial neural networks. *Computers and Geosciences*, 27, 627–637. [https://doi.org/10.1016/S0098-3004\(03\)00044-X](https://doi.org/10.1016/S0098-3004(03)00044-X)
- Anton, A., Klebercz, O., Magyar, A., Burke, I., Jarvis, A., Gruiz, K., & Meyes, W. (2014). Geochemical recovery of the Torna–Marcal river system after the Ajka red mud spill, Hungary. *Environmental Science: Processes & Impacts*, 16, 2677–2685. <https://doi.org/10.1039/C4EM00452C>
- Azapagic, A. (2004). Developing a framework for sustainable development indicators for the mining and minerals industry. *Journal of Cleaner Production*, 12, 639–662. [https://doi.org/10.1016/S0959-6526\(03\)00075-1](https://doi.org/10.1016/S0959-6526(03)00075-1)
- Baek, J., Kim, S.-W., Park, H.-J., Jung, H.-S., Kim, K.-D., & Kim, J. W. (2008). Analysis of ground subsidence in coal mining area using SAR interferometry. *Geosciences Journal*, 27, 277–284. <https://doi.org/10.1007/s12303-008-0028-3>
- Bassani, C., Cavalli, R. M., Cavalcante, F., Cuomo, V., Palombo, A., Pascucci, S., & Pignatti, S. (2007). Deterioration status of asbestos-cement roofing sheets assessed by analyzing hyperspectral data. *Remote Sensing of Environment*, 109, 361–378. <https://doi.org/10.1016/j.rse.2007.01.014>
- bp. (2017). *BP Statistical Review of World Energy June 2017*. Retrieved from bp.com/statisticalreview/
- Brasington, J., Langham, J., & Rumsby, B. (2003). Methodological sensitivity of morphometric estimates of coarse fluvial sediment transport. *Geomorphology*, 53(3–4), 299–316. [https://doi.org/10.1016/S0169-555X\(02\)00320-3](https://doi.org/10.1016/S0169-555X(02)00320-3)
- Business Insider Intelligence. (2015). *The drones report: Market forecasts for commercial applications, regulatory process and leading players*.
- Carrington, D. (2016). The Anthropocene epoch: scientists declare dawn of human-influenced age. *The Guardian*, 4. Retrieved from

- <https://www.theguardian.com/environment/2016/aug/29/declare-anthropocene-epoch-experts-urge-geological-congress-human-impact-earth>
- Cavalli, M., Tarolli, P., Marchi, L., & Dalla Fontana, G. (2008). The effectiveness of airborne LiDAR data in the recognition of channel-bed morphology, *73*, 249–260.
<https://doi.org/10.1016/j.catena.2007.11.001>
- Chen, J., Li, K., Chang, K. J., Sofia, G., & Tarolli, P. (2015). Open-pit mining geomorphic feature characterisation. *International Journal of Applied Earth Observation and Geoinformation*, *42*, 76–86. <https://doi.org/10.1016/j.jag.2015.05.001>
- Chen, Q. (2007). Airborne Lidar Data Processing and Information Extraction. *Photogrammetric Engineering & Remote Sensing*, *73*, 109–112.
- Clever Drone Maps. (n.d.). Vantaggi degli uav ad ala fissa rispetto a quelli ad ala rotante. Retrieved from <http://www.cleverdronemaps.com/>
- CNR. (2018). Interferometria Differenziale Radar ad Apertura Sintetica. *Istituto per Il Rilevamento Elettromagnetico Dell'ambiente*, 1–2.
- Crutzen, P. J. (2002). Geology of mankind. *Nature*, *415*, 23–23.
<https://doi.org/10.1038/415023a>
- Dassot, M., Constant, T., & Fournier, M. (2011). The use of terrestrial LiDAR technology in forest science: Application fields, benefits and challenges. *Annals of Forest Science*, *68*(5), 959–974. <https://doi.org/10.1007/s13595-011-0102-2>
- Datcu, M., Daschiel, H., Pelizzari, A., Quartulli, M., Galoppo, A., Colapicchioni, A., ... Elia, S. D. (2003). Information Mining in Remote Sensing Image Archives: System Concepts. *IEEE Transactions of Geoscience and Remote Sensing*, *41*, 2923–2936.
- Drone Nodes. (2015). 13 Commercial drone applications and UAV progress insight. Retrieved from <http://dronenodes.com/commercial-drone-applications/#tab-con-12>
- Ely, J. C., Graham, C., Barr, I. D., Rea, B. R., Spagnolo, M., & Evans, J. (2017). Using UAV acquired photography and structure from motion techniques for studying glacier landforms: application to the glacial flutes at Isfallsglaciären. *Earth Surface Processes and Landforms*, *42*, 877–888. <https://doi.org/10.1002/esp.4044>
- Erlandson, J. M., & Braje, T. J. (2014). Archeology and the Anthropocene. *Biochemical Pharmacology*, *4*, 1–7. <https://doi.org/10.1016/j.ancene.2014.05.003>
- Evans, I. S., & Chorley, R. (1979). Spatial analysis in geomorphology. *General*

Geomorphometry, Derivatives of Altitude, and Descriptive Statistics: Harper & Row, New York, 17–90.

Evans, K., Martin, P., Moliere, D., Saynor, M., Prendergast, J., & Erskine, W. (2004). Erosion Risk Assessment of the Jabiluka Min Site, Northern Territory, Australia. *Journal of Hydrologic Engineering*, 512–522. [https://doi.org/10.1061-\(ASCE\)1084-0699\(2004\)9:6\(512\)](https://doi.org/10.1061-(ASCE)1084-0699(2004)9:6(512))

Fernandes, G., Goulart, F. F., Ranieri, B. D., Coelho, M. S., Dales, K., Boesche, N., ... Soares-filho, B. (2016). Deep into the mud: ecological and socio-economic impacts of the dam breach in Mariana, Brazil. *Natureza & Conservação*, 14, 35–45. <https://doi.org/10.1016/j.ncon.2016.10.003>

Flood, M. (2001). Laser Altimetry: from science to commercial Lidar Mapping. *Photogrammetric Engineering and Remote Sensing*, 67(11).

Fonstad, M. A., Dietrich, J. T., Courville, B. C., Jensen, J. L., & Carbonneau, P. E. (2013). Topographic structure from motion: A new development in photogrammetric measurement. *Earth Surface Processes and Landforms*, 38(4), 421–430. <https://doi.org/10.1002/esp.3366>

Galloway, J. N., Townsend, A. R., Erisman, J. W., Bekunda, M., Cai, Z., Freney, J. R., ... Sutton, M. A. (2008). Transformation of the Nitrogen Cycle: *Science*, 320, 889–892. <https://doi.org/10.1126/science.1136674>

Ge, L., Li, X., & Ng, A. H.-M. (2016). UAV for mining applications: A case study at an open-cut mine and a longwall mine in New South Wales, Australia. *International Geoscience and Remote Sensing Symposium (IGARSS), 2016–Novem(1)*, 5422–5425. <https://doi.org/10.1109/IGARSS.2016.7730412>

Ge, L., Rizos, C., Han, S., & Zebker, H. (2001). Mining subsidence monitoring using the combined InSAR and GPS approach. *Proceedings of the 10th International Symposium on Deformation Measurements*, 1–10. <https://doi.org/10.1.1.15.5114>

Gelencsér, A., Kováts, N., Turóczy, B., Rostási, Á., Hoffer, A., Imre, K., ... Pósfai, M. (2011). The red mud accident in Ajka (Hungary): Characterization and potential health effects of fugitive dust. *Environmental Science and Technology*, 45(4), 1608–1615. <https://doi.org/10.1021/es104005r>

Georgieva, S. S., Todd, J. T., Peeters, R., & Orban, G. A. (2008). The extraction of 3D shape from texture and shading in the human brain. *Cerebral Cortex*, 18, 2416–2438.

<https://doi.org/10.1093/cercor/bhn002>

Giordan, D., Hayakawa, Y., Nex, F., Remondino, F., & Tarolli, P. (2018). Review article: The use of remotely piloted aircraft systems (RPASs) for natural hazards monitoring and management. *Natural Hazards and Earth System Sciences*, 1079–1096.

<https://doi.org/10.5194/nhess-18-1079-2018>

Glauert, H. (1935). Airplane propellers. In *Aerodynamic theory* (pp. 169–360). Springer.

GreatMining. (2017). Shrinkage Stope Mining. Retrieved from <http://www.greatmining.com/>

Green, S., Bevan, A., & Shapland, M. (2014). A comparative assessment of structure from motion methods for archaeological research. *Journal of Archaeological Science*, 46, 173–181. <https://doi.org/10.1016/j.jas.2014.02.030>

Gutman, G., Janetos, A. C., Justice, C. O., Moran, E. F., Mustard, J. F., Rindfuss, R. R., ... Cochrane, M. A. (2004). *Land change science: Observing, monitoring and understanding trajectories of change on the earth's surface* (Vol. 6). Springer Science & Business Media.

Hardin, P., & Hardin, A. (2013). Hyperspectral Remote Sensing of Urban Areas. *Geography Compass*, 1, 7–21. <https://doi.org/10.1111/gec3.12017>

Hartman, Howard L.; Mutmansky, J. M. . (2002). Introduction to mining. In *Introductory Mining Engineering* (pp. 1–24). Retrieved from <http://media.wiley.com/>

Hodgson, M. E., Jensen, J., Raber, G., Tullis, J., Davis, B. a, Thompson, G., & Schuckman, K. (2005). An Evaluation of Lidar-derived Elevation and Terrain Slope in Leaf-off Conditions. *Photogrammetric Engineering & Remote Sensing*, 71, 817–823. <https://doi.org/10.14358/PERS.71.7.817>

ICS. (2004). *Chronostratigraphic Chart*. Retrieved from <http://www.stratigraphy.org/ICSchart/ChronostratChart2018-07.pdf>

INPE - Instituto Nacional de Pesquisas Espaciais. (2015). Satélites mostram trajetória de sedimentos no Rio Doce. Retrieved from <http://www.inpe.br/>

International Energy Agency. (2017). *Coal information 2017 - International Energy Agency*. Retrieved from <https://www.iea.org/>

Jasmine, C. (2016). Rio Tinto's Kennecott wins clean air lawsuit in the US. Retrieved from <http://www.mining.com/>

Jha, A. (2010). Hungary toxic sludge spill an “ecological catastrophe” says government. *The*

- Guardian*, pp. 1–2.
- Joshi, D. (2017). Exploring the latest drone technology for commercial, industrial and military drone uses. *Business Insider*, pp. 1–4. Retrieved from <http://www.businessinsider.com/drone-technology-uses-2017-7>
- Kaufman, Y. J., Tanré, D., Remer, L. A., Vermote, E. F., Chu, A., & Holben, B. N. (1997). Operational remote sensing of tropospheric aerosol over land from EOS moderate resolution imaging spectroradiometer. *Journal of Geophysical Research: Atmospheres*, *102*, 17051–17067. <https://doi.org/10.1029/96JD03988>
- Kelly, M., & Di Tommaso, S. (2015). Mapping forests with Lidar provides flexible, accurate data with many uses. *California Agriculture*, *69*, 14–20. <https://doi.org/10.3733/ca.v069n01p14>
- Lal, R. (1998). Soil Erosion Impact on Agronomic Productivity and Environment Quality. *Critical Reviews in Plant Sciences*, *17*(4), 319–464. <https://doi.org/10.1080/07352689891304249>
- Lane, S. N., Widdison, P. E., Thomas, R. E., Ashworth, P. J., Best, J. L., Lunt, I. A., ... Simpson, C. J. (2010). Quantification of braided river channel change using archival digital image analysis. *Earth Surface Processes and Landforms*, *35*(8), 971–985. <https://doi.org/10.1002/esp.2015>
- Lee, S., & Choi, Y. (2015). Topographic survey at small-scale open-pit mines using a popular rotary-wing unmanned aerial vehicle (drone). *Tunnel and Underground Space*, *25*, 462–469. <https://doi.org/10.7474/TUS.2015.25.5.462>
- Lemmens, M. (2007). Airborne lidar sensors. *GIM International*, *21*, 24–27.
- Lewis, S. L., & Maslin, M. A. (2015). Defining the Anthropocene. *Nature*, *519*, 171–180. <https://doi.org/10.1038/nature14258>
- Lillesand, Thomas, Kiefer, & Chipman. (2014). *Remote sensing and image interpretation*. (John Wiley & Sons, Ed.).
- Liu, X., Zhang, Z., Peterson, J., & Chandra, S. (2007). LiDAR-derived high quality ground control information and DEM for image orthorectification. *GeoInformatica*, *11*, 37–53. <https://doi.org/10.1007/s10707-006-0005-9>
- Lopes, L. M. N. (2016). O rompimento da barragem de Mariana e seus impactos socioambientais. *Sinapse Múltipla*, *5*, 1–14. Retrieved from <http://periodicos.pucminas.br/index.php/sinapsemultipla>

- Mancini, F., Dubbini, M., Gattelli, M., Stecchi, F., Fabbri, S., & Gabbianelli, G. (2013). Using unmanned aerial vehicles (UAV) for high-resolution reconstruction of topography: The structure from motion approach on coastal environments. *Remote Sensing*, 5(12), 6880–6898. <https://doi.org/10.3390/rs5126880>
- Marcoe, K. (2007). LIDAR an Introduction and Overview. Retrieved from http://web.pdx.edu/~jduh/courses/Archive/geog481w07/Students/Marcoe_LiDAR.pdf
- Marinha do Brasil. (2015). *Levantamento ambiental expedito em regência/es*.
- Maslin, M., & Lewis, S. (2018). Anthropocene vs Meghalayan: why geologists are fighting over whether humans are a force of nature.
- Mayes, W. M., Burke, I. T., Gomes, H. I., Anton, Á. D., Molnár, M., Feigl, V., & Ujaczki, É. (2016). Advances in Understanding Environmental Risks of Red Mud After the Ajka Spill, Hungary. *Journal of Sustainable Metallurgy*, 2, 332–343. <https://doi.org/10.1007/s40831-016-0050-z>
- Miao, Z., & Marrs, R. (2000). Ecological restoration and land reclamation in open-cast mines in Shanxi Province, China. *Journal of Environmental Management*, 59, 205–215. <https://doi.org/10.1006/jema.2000.0353>
- Mielke, C., Rogass, C., Boesche, N., Segl, K., & Altenberger, U. (2015). New geometric hull continuum removal algorithm for automatic absorption band detection from spectroscopic data. *Taylor & Francis*, 6, 97–105. <https://doi.org/10.1080/2150704X.2015.1007246>
- NASA. Vegetation Canopy Lidar (VCL): Case Story & Lessons Learned, Academy of Program and Project Leadership and the Systems Management Office 1–25 (2003). Retrieved from https://www.nasa.gov/pdf/384157main_VCL_case_study.pdf
- Nelson, S. A. (2015). Geologic time. Retrieved from <http://www.tulane.edu/~sanelson/eens1110/geotime.htm>
- O'Hagan, G. (1997). Highwall Mining: The Way Ahead The Addcar Highwall Mining System. *Australian Coal Review*, 12–24.
- Obanawa, H., & Hayakawa, Y. S. (2015). High-resolutional topographic survey using small UAV and SfM-MVS technologies in hardly accessible area. *The International Symposium on Cartography in Internet and Ubiquitous Environment 2015*, 1–9.
- Othmani, A., Piboule, A., Krebs, M., & Stolz, C. (2011). Towards automated and operational forest inventories with T-Lidar. *SilviLaser*, 1, 1–9.

- Pandey, A., Chowdary, V. M., & Mal, B. C. (2007). Identification of critical erosion prone areas in the small agricultural watershed using USLE , GIS and remote sensing. *Water Resour Manage*, *21*, 729–746. <https://doi.org/10.1007/s11269-006-9061-z>
- Pankow, K. L., Moore, J. R., Mark Hale, J., Koper, K. D., Kubacki, T., Whidden, K. M., & McCarter, M. K. (2014). Massive landslide at Utah copper mine generates wealth of geophysical data. *GSA Today*, *24*, 4–9. <https://doi.org/10.1130/GSATG191A.1>
- Pettorelli, N., Vik, J. O., Mysterud, A., Gaillard, J. M., Tucker, C. J., & Stenseth, N. C. (2005). Using the satellite-derived NDVI to assess ecological responses to environmental change. *Trends in Ecology and Evolution*, *20*(9), 503–510. <https://doi.org/10.1016/j.tree.2005.05.011>
- Polyakov, V., & Lal, R. (2004). Modeling soil organic matter dynamics as affected by soil water erosion. *Environment International*, *30*, 547–556. <https://doi.org/10.1016/j.envint.2003.10.011>
- Prosdocimi, M., Calligaro, S., Sofia, G., Dalla Fontana, G., & Tarolli, P. (2015). Bank erosion in agricultural drainage networks: New challenges from structure-from-motion photogrammetry for post-event analysis. *Earth Surface Processes and Landforms*, *40*(14), 1891–1906. <https://doi.org/10.1002/esp.3767>
- Puigdefabregas, J., Sole, A., Gutierrez, L., Del Barrio, G., & Boer, M. (1999). Scales and processes of water and sediment redistribution in drylands: Results from the Rambla Honda field site in Southeast Spain. *Earth Science Reviews*, *48*, 39–70. [https://doi.org/10.1016/S0012-8252\(99\)00046-X](https://doi.org/10.1016/S0012-8252(99)00046-X)
- Raymond, R. W. (1881). Glossary of Mining and Metallurgical Terms. *American Institute of Mining Engineers*, 3.
- Recker, S., Shashkov, M., Hess-Flores, M., Baltrusch, R., Butkiewicz, M., & Joy, K. (2014). Structure-From-Motion Systems for Scene Measurement. *Quality Digest*, *1*, 1–18.
- Reichl, C., Schatz, M., & Zsak, G. (2017). *World mining data* (Vol. 32). Retrieved from <http://www.wmc.org.pl/>
- Rio Tinto Corporate. (2017). Kennecott Official Webpage. Retrieved from <http://www.kennecott.com/>
- RitchieWiki. (2017). Highwall Mining. Retrieved from <http://www.ritchiewiki.com/>
- Rocken, C., Ware, R., Vanhove, T., Solheim, F., Alber, C., & Johnson, J. (1993). Sensing atmospheric water-vapor with the Global Positioning System. *Geophysical Research*

- Letters*, 20, 2631–2634. <https://doi.org/10.1029/93gl02935>
- Ruddiman, W. F. (2003). The anthropogenic greenhouse era began thousands of years ago. *Climatic Change*, 61, 261–293. <https://doi.org/10.1007/s10584-005-7278-0>
- Sabins, F. F. (1999). Remote sensing for mineral exploration. *Ore Geology Reviews*, 157–183.
- Salomons, W. (1995). Environmental impact of metals derived from mining activities: Processes, predictions, prevention. *Journal of Geochemical Exploration*, 52, 5–23.
- Sofia, G., Masin, R., & Tarolli, P. (2017). Prospects for crowdsourced information on the geomorphic “engineering” by the invasive Coypu (*Myocastor coypus*). *Earth Surface Processes and Landforms*, 42, 365–377. <https://doi.org/10.1002/esp.4081>
- Sousa, J. J., & Bastos, L. (2013). Multi-temporal SAR interferometry reveals acceleration of bridge sinking before collapse. *Natural Hazards and Earth System Science*, 13, 659–667. <https://doi.org/10.5194/nhess-13-659-2013>
- Steffen, W., Broadgate, W., Deutsch, L., Gaffney, O., & Ludwig, C. (2015). The trajectory of the anthropocene: The great acceleration. *Anthropocene Review*, 2(1), 81–98. <https://doi.org/10.1177/2053019614564785>
- Steffen, W., Grinevald, J., Crutzen, P., & McNeill, J. (2011). The Anthropocene: conceptual and historical perspectives. *Philosophical Transactions of the Royal Society A: Mathematical, Physical and Engineering Sciences*, 369, 842–867. <https://doi.org/10.1098/rsta.2010.0327>
- Steffen, W., Sanderson, R. A., Tyson, P. D., Jäger, J., Matson, P. A., Moore III, B., ... others. (2004). *Global change and the earth system: a planet under pressure*. Springer Science & Business Media.
- Suh, J., & Choi, Y. (2017). Mapping hazardous mining-induced sinkhole subsidence using unmanned aerial vehicle (drone) photogrammetry. *Environmental Earth Sciences*, 1–12. <https://doi.org/10.1007/s12665-017-6458-3>
- Tang, Q., Gao, H., Lu, H., & Lettenmaier, D. P. (2009). Remote sensing: hydrology. *Progress in Physical Geography*, 33, 490–509. <https://doi.org/10.1177/0309133309346650>
- Tarolli, P., Arrowsmith, J. R., & Vivoni, E. R. (2009). Understanding earth surface processes from remotely sensed digital terrain models. *Geomorphology*, 113, 1–3. <https://doi.org/10.1016/j.geomorph.2009.07.005>

- Tarolli, P., & Sofia, G. (2016). Human topographic signatures and derived geomorphic processes across landscapes. *Geomorphology*, 255, 140–161.
<https://doi.org/10.1016/j.geomorph.2015.12.007>
- Tarolli, P., Sofia, G., & Dalla Fontana, G. (2012). Geomorphic features extraction from high-resolution topography: Landslide crowns and bank erosion. *Natural Hazards*, 65–83.
<https://doi.org/10.1007/s11069-010-9695-2>
- Thornton, E., Sallenge, A., Sesto, J. Co., Egley, L., McGee, T., & Parson, R. (2006). Sand mining impacts on long-term dune erosion in southern Monterey Bay. *International Journal of Marine Geology, Geochemistry and Geophysics*, 45–58.
<https://doi.org/10.1038/NMAT2404>
- Thrush, P. (1996). A dictionary of mining, mineral and related terms. *American Geological Institute*, 1275. <https://doi.org/10.1180/minmag.1970.037.289.21>
- Tiwary, R., Dhar, B., & Jamal, A. (1997). Acid mine drainage occurrences and its control in Indian coal mines. In *Proceedings of the 27th International Conference of Safety in Mines Research Institute* (pp. 1253–1259). New Delhi, India.
- Tiwary, R. K. (2001). Environmental impact of coal mining on water regime and its management. *Water, Air, and Soil Pollution*, 132, 185–199.
- Tiwary, R. K., & Dhar, B. B. (1994). Environmental pollution from coal mining activities in damodar river basin, India. *Mine Water and the Environment*, 13, 1–10.
- Tomlinson, C. J., Chapman, L., Thornes, J. E., & Baker, C. (2011). Remote sensing land surface temperature for meteorology and climatology: A review. *Meteorological Applications*, 18, 296–306. <https://doi.org/10.1002/met.287>
- Tong, X., Liu, X., Chen, P., Liu, S., Luan, K., Li, L., ... Hong, Z. (2015). Integration of UAV-Based Photogrammetry and Terrestrial Laser Scanning for the Three-Dimensional Mapping and Monitoring of Open-Pit Mine Areas. *Remote Sensing*, 7, 6635–6662.
<https://doi.org/10.3390/rs70606635>
- Tooth, S., & Viles, H. (1991). Ten reasons why Geomorphology is important. *British Society for Geomorphology*, 1, 1–17. Retrieved from
<http://serc.carleton.edu/vignettes/index.html>
- Torres-Sanchez, J., Peña, J. M., de Castro, A. I., & López-Granados, F. (2014). Multi-temporal mapping of the vegetation fraction in early-season wheat fields using images from UAV. *Computers and Electronics in Agriculture*, 103, 104–113.

- <https://doi.org/10.1016/j.compag.2014.02.009>
- U.S. Army Training and Doctrine Command - TRADOC. (2010). *Us army unmanned aircraft systems roadmap 2010-2035*. Federation Of American Scientists.
- Unipi. (2016). Il radar ad apertura sintetica. Retrieved from http://www2.ing.unipi.it/~a005993/Materiale_Didattico/MTT/LEZIONI/SAR.pdf
- United States Environmental Protection Agency. (2016). Mountaintop Mining Research. Retrieved from <https://www.epa.gov/>
- Ustin, S. L., & Gamon, J. A. (2010). Remote sensing of plant functional types. *New Phytologist*, 186, 795–816. <https://doi.org/10.1111/j.1469-8137.2010.03284.x>
- UVS International. (2012). Remotely piloted aircraft systems. In *RPAS Glossary 130815* (pp. 5–6).
- Watts, A. C., Ambrosia, V. G., & Hinkley, E. A. (2012). Unmanned aircraft systems in remote sensing and scientific research: Classification and considerations of use. *Remote Sensing*, 4(6), 1671–1692. <https://doi.org/10.3390/rs4061671>
- Weedman, S. (2001). Energy Resources Program of the U . S . Geological Survey. *USGS Science for a Changing World*. Retrieved from <https://pubs.usgs.gov/>
- Wegmuller, U., Strozzi, T., Werner, C., Wiesmann, A., Norbert, B., & Volker, S. (2000). Monitoring of mining-induced surface deformation in the Ruhrgebiet (Germany) with SAR interferometry. *IEEE Transactions on Geoscience and Remote Sensing*, 2771–2773.
- Wehr, A., & Lohr, U. (1999). Airborne laser scanning—an introduction and overview. *ISPRS Journal of Photogrammetry & Remote Sensing*, 54, 68–82. [https://doi.org/10.1016/s0924-2716\(99\)00011-8](https://doi.org/10.1016/s0924-2716(99)00011-8)
- Westoby, M. J., Brasington, J., Glasser, N. F., Hambrey, M. J., & Reynolds, J. M. (2012). “Structure-from-Motion” photogrammetry: A low-cost, effective tool for geoscience applications. *Geomorphology*, 179, 300–314. <https://doi.org/10.1016/j.geomorph.2012.08.021>
- Wężyk, P., Szostak, M., Krzaklewski, W., Pająk, M., Pierzchalski, M., Szwed, P., ... Ratajczak, M. (2015). Landscape monitoring of post-industrial areas using LiDAR and GIS technology. *Geodesy and Cartography*, 125–137. <https://doi.org/10.1515/geocart-2015-0010>

- Wheaton, J. M., Brasington, J., Darby, S. E., & Sear, D. A. (2010). Accounting for uncertainty in DEMs from repeat topographic surveys: Improved sediment budgets. *Earth Surface Processes and Landforms*, 35, 136–156. <https://doi.org/10.1002/esp.1886>
- Williams, R. D. (2012). DEMs of Difference. *Geomorphological Techniques*, 2, 1–17. <https://doi.org/2047-0371>
- World Bank Group. (2017). World population. Retrieved from <https://data.worldbank.org/>
- World Nuclear Association. (2017). In Situ Leach Mining of Uranium. Retrieved from <http://www.world-nuclear.org/>
- Xiang, J., Chen, J., Sofia, G., Tian, Y., & Tarolli, P. (2018). Open - pit mine geomorphic changes analysis using multi - temporal UAV survey. *Environmental Earth Sciences*, (77), 219–220. <https://doi.org/10.1007/s12665-018-7383-9>
- Xiao, J., Shen, Y., Ge, J., Tateishi, R., Tang, C., Liang, Y., & Huang, Z. (2006). Evaluating urban expansion and land use change in Shijiazhuang, China, by using GIS and remote sensing. *Landscape and Urban Planning*, 75, 69–80. <https://doi.org/10.1016/j.landurbplan.2004.12.005>
- Xiaoye Liu. (2008). Airborne LiDAR for DEM generation: some critical issues. *Progress in Physical Geography*, 32, 31–49. <https://doi.org/10.1177/0309133308089496>
- Zalasiewicz, J., Williams, M., Haywood, A., & Ellis, M. (2011). The Anthropocene: a new epoch of geological time? *Philosophical Transaction of Royal Society*, 369, 835–841. <https://doi.org/10.1098/rsta.2010.0339>
- Zhang, L., Wang, J., Bai, Z., & Lv, C. (2015). Effects of vegetation on runoff and soil erosion on reclaimed land in an opencast coal-mine dump in a loess area. *Catena*, 128, 44–53. <https://doi.org/10.1016/j.catena.2015.01.016>
- Zhao, Z., Shahrour, I., Bai, Z., Fan, W., Feng, L., & Li, H. (2013). Soils development in opencast coal mine spoils reclaimed for 1 e 13 years in the West-Northern Loess Plateau of China. *European Journal of Soil Biology*, 55, 40–46. <https://doi.org/10.1016/j.ejsobi.2012.08.006>
- Zhou, G. (2009). Near Real-Time Orthorectification and Mosaic of Small UAV Video Flow for Time-Critical Event Response. *IEEE Transactions of Geoscience and Remote Sensing*, 47(3), 739–747.

ACKNOWLEDGEMENTS

The end of a wonderful period of my life has come. The time to look back, to reap the fruits of so much work and to launch myself towards my tomorrow.

I would like to write on this piece of paper a few (but sincere) words to thank all the people who allowed me to cross the line of this fundamental goal of my life.

First of all, I would like to thank my mentor and professor, Paolo Tarolli, not because he is my professor and I feel obliged to do it, but because he was a real turning point in my life. He taught me a lot, not only didactically speaking, he also allowed me to have a unique experience that I will probably never be able to do again in my life. He taught me to open my eyes to the World and to appreciate the different, with curiosity and desire to experiment. Finally, I thank him for having affixed that flyer with the Chinese flag to the coffee machines.

I would like to thank Professor Chen and his wonderful working group. Thanks to Jeckie, Huang, PanTinTin, Enrè, Clever, Ulmair, David and Shi (I hope you can forgive me but your real names are a bit complicated for me). Thank you for the fundamental support in this thesis, of course, but thank you especially for making me feel at home 8,118 km from the real one. Thank you for letting me immerse in your splendid and millenary culture, with passion and welcome, showing me all those facets of China that only a few have the privilege of living.

I will miss you, my friends.

I also thank people who are the key of my life, those people who without them I would not be who I am.

Thanks to my parents, an example of strength, tenacity and generosity. Thanks to Tommaso and my wonderful grandmothers, for every kind of comfort, especially Christian and culinary. Thank you to all my relatives.

I feel lucky to be part of this family.

Thanks to my friends, those of a lifetime, those who are far away or near are always there with me.

Thanks to the friends I met in Padova, you have made these 5 years unique. Thanks to my roommates Chiara and Flavia, thanks to Luca, Isy and Sve. You have been very important to me, and you will always be.

Thanks to Federica, an extraordinary person of great heart, who has always been close to me on every occasion and who has always supported me in every choice. I feel lucky to have met such a beautiful and intelligent person as you. And with her, of course, I also thank your fantastic roommates!

Thanks to Cristian, a colleague but, above all, a friend. An example for me, of goodness and altruism. Then I thank him for his always impeccable advice.

Thanks to Manuela for the endless trips to Padova that became very short, filled with our interesting chats.

Thanks to Angelo and Ileana. Thanks for their support, their advice and their chocolate (faithful travel companion in China). Also thanks for boat trips: the best way to oxygenate the mind after hours on this thesis.

And finally, thanks to Tiz, because despite your distance you have always been an example to me. In addition, if I'm going to become an *arzenpoiner* too, I think it's all your fault!